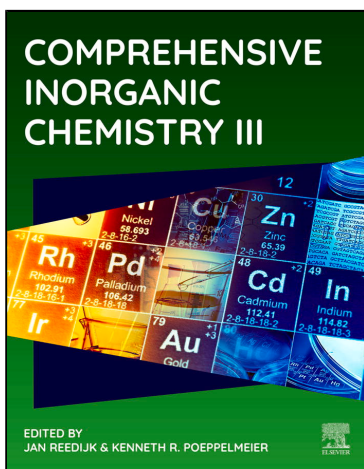


Provided for non-commercial research and educational use.
Not for reproduction, distribution or commercial use.

This article was originally published in Comprehensive Inorganic Chemistry III, published by Elsevier, and the attached copy is provided by Elsevier for the author's benefit and for the benefit of the author's institution, for non-commercial research and educational use including without limitation use in instruction at your institution, sending it to specific colleagues who you know, and providing a copy to your institution's administrator.



All other uses, reproduction and distribution, including
without limitation commercial reprints, selling or
licensing copies or access, or posting on open
internet sites, your personal or institution's website or
repository, are prohibited. For exceptions, permission
may be sought for such use through Elsevier's
permissions site at:

<https://www.elsevier.com/about/our-business/policies/copyright/permissions>

Nelson, R.; Ertural, C.; Müller, P. C.; Dronskowski, R. Chemical bonding with plane waves. In *Theory and Bonding of Inorganic Non-molecular Systems*; Fredrickson, D. C.; in Comprehensive Inorganic Chemistry III; Reedijk, J., Poeppelmeier, K. R., Eds.; Vol. 3, pp 141–201. Oxford: Elsevier. ©2023 Elsevier Ltd. ISBN 9780128231531. DOI: B978-0-12-823144-9.00120-5.
ISBN: 9780128231449
Copyright © 2023 Elsevier Ltd. All rights reserved
Elsevier

3.07 Chemical bonding with plane waves

Ryky Nelson, Christina Ertural, Peter C. Müller, and Richard Dronskowski, Institute of Inorganic Chemistry, RWTH Aachen University, Aachen, Germany

© 2023 Elsevier Ltd. All rights reserved.

3.07.1	Part I: Foundations	142
3.07.1.1	Introduction	142
3.07.1.2	Chemical bonding for the simplest molecule: H ₂	143
3.07.1.3	Schrödinger's and Fock's equation, Kohn-Sham equations: DFT	144
3.07.1.4	More complicated molecules, LCAO in general	147
3.07.1.5	Plane Waves and Bloch's theorem	148
3.07.1.6	One-dimensional systems	149
3.07.1.7	Concept of charges and bonding Indicators (COOP and COHP)	151
3.07.2	Part II: Methods	155
3.07.2.1	Basis functions	155
3.07.2.2	Pseudopotentials in general	157
3.07.2.3	Projector augmented wave method	158
3.07.2.4	Plane-wave-based quantum chemistry programs	159
3.07.2.5	Projection method	160
3.07.2.6	Atomic basis sets in LOBSTER	162
3.07.2.7	The projected DOS, COOP, COHP, fatband, and \mathbf{k} -dependent COHP and time-reversal symmetry	163
3.07.2.8	Mulliken and Löwdin population analysis	166
3.07.2.9	Crystal orbital bond index	168
3.07.2.10	Averaged bonding descriptors	171
3.07.2.10.1	Covalent bonding indicators: Averaged COHP and effective interaction number	171
3.07.2.10.2	Ionic bonding indicators: Ionicity and Madelung energy	173
3.07.3	Part III: Applications	176
3.07.3.1	Molecular systems	176
3.07.3.2	Bonding between molecules (H and X bonding), bonding on surfaces	178
3.07.3.3	Semiconductors such as GaAs and Phase-change materials	180
3.07.3.4	Spin polarization and magnetic systems	184
3.07.3.5	Rechargeable battery electrode materials	187
3.07.3.6	Thermoelectrics and Zintl phases	189
3.07.3.7	Materials mapping	191
3.07.3.8	Interplay of bonding and structure	194
3.07.4	Computational details	196
Acknowledgments		196
References		196

Abstract

Two kinds of basis functions, plane waves and local orbitals, have been dominantly used in quantum chemistry due to their specific advantages. The former excels because of its simple computational implementation, whereas the latter is often chosen because of its convenience of extracting and analyzing chemical aspects of materials. In this review, we thoroughly describe a projection method bridging these two kinds of basis functions in order to harvest the benefits of their properties. Although the projection technique can in principle be applied to any quantum-chemical method, a particular implementation has been realized in a computer program called Local Orbital Basis Suite Towards Electronic-Structure Reconstruction (LOBSTER) processing data from density-functional theory (DFT) calculations. The reconstruction, furthermore, facilitates chemical bonding analysis through various bonding indicators and extraction of chemical information. Prior to the description of the projection method, the concept of chemical bonding is introduced to emphasize its importance in understanding chemical systems. Afterward, formulations of various quantum-chemical methods helping to understand bonding problems in many-electron systems are also described. Finally, we present diverse interesting material studies, including molecular systems, semiconductors, phase-change materials, electrode materials, etc. in great detail to demonstrate the advantages of exploiting both kinds of basis functions simultaneously.

3.07.1 Part I: Foundations

3.07.1.1 Introduction

Strange, isn't it, that chemists can talk for hours about the concept of chemical bonding (let alone writing review articles about that very subject) although, strictly speaking, such phenomenon dubbed "chemical bonding" does not exist at all if we hide in the incredibly tiny box labeled "physics reductionism". As will be clarified somewhat later and as provocatively formulated by Richard Feynman quite early, all theoretical chemistry is really physics, and all theoretical chemists know it.

But seriously and for the moment being, let us predict what we are going to witness in the coming sections: to solve those quantum-mechanical equations envisioned by Schrödinger or by Kohn and Sham serving us well when dealing with atoms, molecules, and solids, the quantum-chemical (there we go!) interpretations but very often also starting assumptions make us aware, puzzlingly enough, that even a quantum-mechanical model of a system dubbed "molecule" does *not* relate to atoms and bonds (the chemist's language) but to nuclei and electrons (the physicist's language). Even worse, the more sophisticated the calculations, the more estranged we may become from chemistry such that, eventually, all the chemical understanding (and the chemical bonding, too) may vanish into thin air.

So where do we start? The good ol' triangle by van Arkel¹ and Ketelaar,² depicted in Fig. 1, will serve us because it already comprises three (out of five) flavors of chemical bonding, at least qualitatively. If we agree on the concept of electronegativity EN,³ namely the tendency of an atom to pull electron density towards itself inside a molecule (or whatever chemical entity), irrespective of whether electronegativity is defined empirically or even quantum-mechanically,⁴ the stage is set for things to come. There are "ionic" compounds to begin with, seen in the upper red corner, which result from chemical reactions between those atoms that strongly differ in their electronegativities, in other words: electronegative nonmetals and not-so-electronegative (lab jargon: "electropositive") metals. Here, the EN difference is so large that an electron eventually hops from one atom (metal which turns into a *cation*) to the other atom (nonmetal becoming an *anion*), and the amount of electron localization at the anion is so tremendous (the electron now fully belonging to the nonmetal atom) that this very electron may be nicely described by a wave function *exclusively* belonging to that atom it eventually resides on. Quantum-chemically speaking, it is a kind of "one-center" bonding because just one atom is involved to hold the electron. As a result, there will be a Coulomb force between cation and anion, and in a three-dimensional solid there results a Madelung field which lends itself to classical bonding theory typically found in textbooks dealing with ionic solids such as CsCl or MgO.

The right blue corner could not be more different. If two highly electronegative atoms (the nonmetals) lacking an EN difference come together, the outer electrons of those atoms will experience the nuclear charge of both atoms, so both atoms and their wave functions will engage in holding those electrons such that a phenomenon called "covalent" bonding must result. Although there are quantum-mechanical principles which somewhat complicate the entire story—the electrons cannot be distinguished and experience so-called electronic exchange due to their Fermionic nature—it is safe to assume that this kind of bonding involves two partners, so it is a "two-center" bonding. This is the type of bonding for which valence-bond and molecular-orbital theory were developed, eventually clarifying the meaning of Lewis' formulation of chemical bonding by drawing a stick for two "paired" electrons, say, in the H₂ molecule. We are surrounded by and composed of such molecules featuring covalent bonds between nonmetal atoms so the importance of that two-center bonding type cannot be overstated.

And yet, there is another corner on the left for which there is also no EN difference but with much smaller electronegativities, so this is all about the interaction of metal atoms, say, in metallic Cs and even in metallic Fe, that is, "metallic" bonding. In metallic systems, there are plenty of metal atoms—which being metal atoms—are always short of a sufficient number of electrons, so some

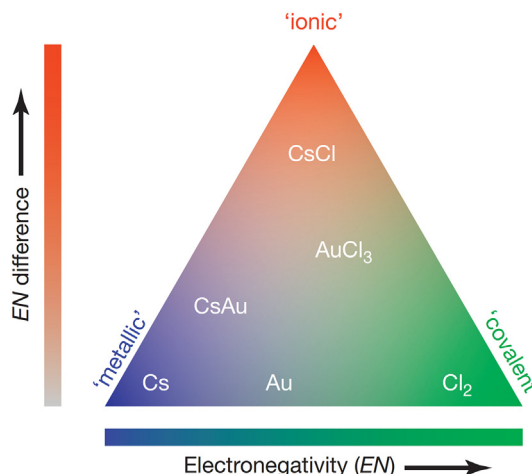


Fig. 1 The van Arkel-Ketelaar triangle of chemical bonding, grouping all chemical species by their EN differences and the EN size of their involved atoms. Reprinted from Deringer, V. L.; Dronskowski, R., Computational Methods for Solids. In: *Comprehensive Inorganic Chemistry II: From Elements to Applications*, Reedijk, J.; Poeppelmeier, K., Eds. Elsevier: Amsterdam, 2013; vol. 9, pp 59–87 with permission from Elsevier.²⁸⁷

kind of electronic socialism sets in to lower the individual burden for all atoms by making an individual electron *collectively* belonging to plenty of atoms at the same time, a kind of "many-center" bonding. Technically speaking, dealing with two or more electrons is not a big difference, and we safely regard "metallic" bonding as a special case of "covalent" bonding. Before we describe how to proceed in terms of real computations, let us also comment on two more "bonding" types which do not show up in the magic triangle.

Even if nonmetal atoms have no electrons to share, such as between light noble-gas elements like He, there is a tendency to come together and lower their energies by some weak "dispersion" forces as originally dubbed by London⁵ or much earlier, in a classical picture, by van der Waals.^{6,7} The reason is the fluctuation of the vacuum (or Heisenberg's uncertainty principle, a matter of taste) which induces momentary atomic dipoles inducing other atomic dipoles, so there results a force from, well, nothing which scales with the polarizability of the atoms but *without* electrons in-between and *without* electron transfer. It is a small effect (which may become significant for, say, molecular iodine), usually incorporated by perturbation theory or empirical corrections. And there is also the biochemist's delight, so-called hydrogen bonding, exclusively found between hydrogen atoms and neighboring atoms with a large EN such as oxygen. In fact, this bonding type is not an independent bonding type but a complicated mélange of the other ones. Because H bonding is so prominent and important (say, for storing genetic information), however, it counts as bonding type no. 5 for sheer reasons of convenience.^{8,9}

So how do we proceed, at least in terms of the first three bonding types? Let us first quantum-chemically characterize two-center covalent bonding between nonmetals because this is what quantum chemistry was made for, successfully so. As a hole-in-one, essentially the same (delocalized) equations but now for metal atoms will make us understand and quantitatively calculate many-center metallic bonding without too much trouble. As another hole-in-one, the same equations will show, once in a while, that some of the electrons are less shared than others, so some atoms will end up with slightly lower/higher electron counts than in their neutral state, thereby arriving at slightly (or even strongly) charged atoms. That is to say that by solving the puzzle of covalent (metallic) bonding given that the atoms do show a little EN difference, we will also, indirectly so, successfully model ionic one-center bonding.

3.07.1.2 Chemical bonding for the simplest molecule: H₂

One of the most iconic and also simplest example of the covalent bond type is given by the H₂ molecule. Even simpler is the hydrogen atom with a single electron, so there is no correlation such that analytical (nonrelativistic) solutions to Schrödinger's equation are exactly known. These hydrogen-like solutions are often used as approximations for other systems.^{10–12} Likewise, the hydrogen molecule is often used as the archetypical case to introduce molecular orbital (MO) theory.

In the MO framework, the hydrogen molecule allows for covalent bonding by the formation of the simplest type of molecular orbital, a σ orbital, from two 1s orbitals, the simplest type of atomic orbital. At the same time, Pauli's exclusion principle forbids that two electrons have the same quantum numbers. In Fig. 2, the formation of a bonding σ (positive overlap of orbitals because of non-orthogonality) and an antibonding σ^* (negative overlap) state for H₂ is shown. Here, the favorable bonding level is occupied and stabilizes the system, unlike the antibonding level. The molecular orbitals are linear combinations of atomic orbitals (LCAO), which, for the H₂ molecule, read

$$\Psi_j(\mathbf{r}) = c_A \psi_A(\mathbf{r}) + c_B \psi_B(\mathbf{r}), \quad (1)$$

and c_A and c_B are the LCAO expansion coefficients for the two H atoms in H₂, both having 1s wave functions ψ_A and ψ_B which are identical for both hydrogen atoms. The LCAO coefficients c_A and c_B are crucial because the symmetric combination ($c_A = c_B = +1$) yields the bonding MO σ orbital with an even (*gerade*) parity σ_g and the antisymmetric combination ($c_A = +1, c_B = -1$) leads to the antibonding σ^* orbital with odd (*ungerade*) parity σ_u .^{10–14}

A very different approach to depict the H₂ molecule is given within valence-bond theory^{3,11,12,15,16} which will only be discussed very briefly. For example, the so-called Heitler-London-Pauling-Slater wave function³

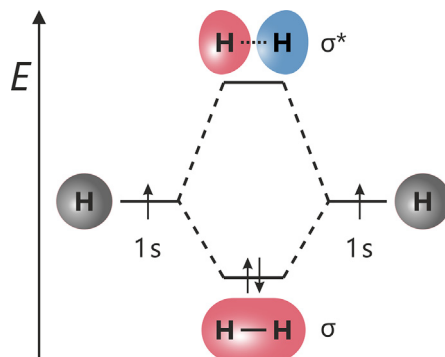


Fig. 2 MO scheme for the hydrogen molecule with its bonding σ and antibonding σ^* orbitals.

$$\Psi_{\text{VB}}(1, 2) = (1 - \eta)\Psi_{\text{cov}}(1, 2) + \eta\Psi_{\text{ion}}(1, 2) \quad (2)$$

with $\Psi_{\text{cov}}(1, 2) = \psi_A(1)\psi_B(2) + \psi_B(1)\psi_A(2)$ and $\Psi_{\text{ion}}(1, 2) = \psi_A(1)\psi_A(2) + \psi_B(1)\psi_B(2)$ for H_2 is a representation of its total wave function that includes both the covalent and ionic structures and allowing for a variational parameter η between the covalent and ionic parts. In contrast, the MO picture, an “uncorrelated” description, puts both contributions on equal footing.

3.07.1.3 Schrödinger's and Fock's equation, Kohn-Sham equations: DFT

To more comprehensively understand chemical bonding, some mathematics is needed to describe it quantitatively. For obvious reasons, quantum mechanics must be employed. Due to the wave nature of electrons (and other atomic entities), position and momentum are no longer deterministic. Instead, the fundamental property of a given quantum system is called a (quantum) state that can provide a probability distribution of a particular observable, such as position, momentum, energy, etc.

One of the formulations of quantum mechanics was proposed by Schrödinger in his 1926 paper through an equation¹⁷ named after him:

$$\left[-\frac{\hbar^2}{2m}\nabla^2 + V(\mathbf{r}) \right] \Psi(\mathbf{r}, t) = i\hbar \frac{\partial \Psi(\mathbf{r}, t)}{\partial t}. \quad (3)$$

This equation describes the evolution of the state, $\Psi(\mathbf{r}, t)$, of a quantum particle moving in a potential $V(\mathbf{r})$. Moreover, $\Psi(\mathbf{r}, t)$ is also called a wave function, and hence the formulation is called wave mechanics, in contrast to matrix mechanics, which is another formulation by Heisenberg.¹⁸ The term inside the square bracket of the left part of Eq. (3) is called the Hamiltonian, H , whereas its first term is called the kinetic energy operator:

$$T = -\frac{\hbar^2}{2m}\nabla^2, \quad (4)$$

with $\nabla^2 = \frac{\partial^2}{\partial x^2} + \frac{\partial^2}{\partial y^2} + \frac{\partial^2}{\partial z^2}$ being the Laplacian. For systems whose potential is time-independent, $\Psi(\mathbf{r}, t)$ can be constructed as a product of a function which only depends on \mathbf{r} and $e^{-iEt/\hbar}$:

$$\Psi(\mathbf{r}, t) = \Psi(\mathbf{r})e^{-iEt/\hbar}. \quad (5)$$

After inserting (5) into (3) and applying the partial derivative over time, we will get:

$$\left[-\frac{\hbar^2}{2m}\nabla^2 + V(\mathbf{r}) \right] \Psi(\mathbf{r}) = E \Psi(\mathbf{r}), \quad (6)$$

where $e^{-iEt/\hbar}$ has been taken out because it no longer affects any further calculation. Eq. (6) is called the time-independent Schrödinger equation, or often just called the Schrödinger equation. Moreover, $\Psi(\mathbf{r})$ is called an eigenfunction associated with an eigenvalue (eigen energy), E . Right after its formulation, the equation was used to study the hydrogen spectra and the results agreed with the experimental results.¹⁹ Further details, such as fine and hyperfine structure of hydrogen, however, require considering relativistic effects which are out of the scope of our discussion. Furthermore, a system with one electron, like hydrogen, is called a one-particle system and has a special place in quantum chemistry because its eigenfunctions can be used to construct the solutions for many-electron systems, as discussed later.

Eq. (6) can be extended for many-electron systems, such as molecular and solid-state materials, by including all the contributions of each electron and atom into the Hamiltonian:

$$H = -\sum_{i=1}^N \frac{\hbar^2}{2m}\nabla_i^2 - \sum_{A=1}^M \frac{\hbar^2}{2M}\nabla_A^2 - \frac{1}{4\pi\varepsilon_0} \left[\sum_{i=1}^N \sum_A \frac{Z_A e^2}{r_{iA}} - \sum_{i=1}^N \sum_{j>i} \frac{e^2}{r_{ij}} - \sum_{A=1}^M \sum_{B>A} \frac{Z_A Z_B e^2}{R_{AB}} \right]. \quad (7)$$

The first and the second terms, respectively, describe the kinetic energy of electrons and nuclei, whereas the third one is the attractive Coulomb interaction between an electron and a nucleus separated by a distance r_{iA} . The fourth and the fifth terms are, respectively, the repulsive Coulomb interaction between two electrons separated by a distance r_{ij} and a pair of nuclei separated by a distance R_{AB} .

Despite its transparent formulation, the Schrödinger equation is practically insolvable without making further approximations. The first one is called the Born-Oppenheimer approximation²⁰ whereby we assume that the electronic and the nuclear parts do not affect each other and can be solved independently. This assumption is based on the argument that the velocities of nuclei and electrons differ drastically. Furthermore, we drop the Coulomb potential between the atoms. Henceforth, we use the Hamiltonian to mean the electronic part only:

$$H = -\sum_{i=1}^N \frac{\hbar^2}{2m}\nabla_i^2 - \frac{1}{4\pi\varepsilon_0} \sum_{i=1}^N \sum_A \frac{Z_A e^2}{r_{iA}} - \frac{1}{4\pi\varepsilon_0} \sum_{i=1}^N \sum_{j>i} \frac{e^2}{r_{ij}}. \quad (8)$$

Before going further, it is important to remember that electrons are quantum particles. Hence, electrons are indistinguishable, so if two electrons are swapped in a system, the system is the same as before. Second, here is the exclusion principle named after Pauli:

two electrons or more cannot enter the same quantum state.²¹ As a consequence, the total wave function of an electronic system has to be antisymmetric.

Back to Eq. (8)! Although the nuclear parts have been taken out, the problem is still far from being solvable due to the third term correlating all electrons with each other, so that the states of all electrons need to be determined simultaneously to get the total wave function. In other words, Eq. (8) forms a set of coupled partial-differential equations of $3N$ variables, where N is the number of electrons with two previous rules as the boundary conditions. Keeping in mind that N can be as large as 10^{23} , this problem is impossible to tackle, even with any current supercomputers.

The first prominent and simplest approximation to solve the Schrödinger equation for many-electron systems is the one proposed by Hartree²² in 1928. Here one assumes that the total wave function is equal to the product of those of individual electrons, which is later called the Hartree product:

$$\Psi(\mathbf{r}) = \psi_a(\mathbf{r}_1)\psi_b(\mathbf{r}_2)\psi_c(\mathbf{r}_3)\cdots, \quad (9)$$

where $\psi_a(\mathbf{r}_1)$, $\psi_b(\mathbf{r}_2)$, $\psi_c(\mathbf{r}_3)$, ... describe one-electron orbitals. Upon inserting this approximated wave function into Schrödinger's equation and introducing a Lagrange multiplier, ε_i , to enforce orthonormalization, the minimization of the Lagrange functional with respect to the one-electron orbitals follows the variation principle, namely

$$\frac{\partial}{\partial \psi_j^*} \left[\int d\mathbf{r} \Psi^*(\mathbf{r}) H \Psi(\mathbf{r}) - \sum_i \varepsilon_i \int d\mathbf{r} |\psi_i(\mathbf{r})|^2 \right] = 0. \quad (10)$$

This leads to a set of one-electron equations

$$\left[-\frac{\hbar^2}{2m} \nabla^2 + V_{\text{eff}}(\mathbf{r}) \right] \psi_i(\mathbf{r}) = \varepsilon_i \psi_i(\mathbf{r}), \quad (11)$$

in which the original potential has been replaced by an effective one, $V_{\text{eff}}(\mathbf{r})$, which consists of the potential by the nuclei and the potential of the average interaction felt by an electron in the vicinity of other electrons:

$$V_{\text{eff}}(\mathbf{r}) = -\frac{1}{4\pi\varepsilon_0} \sum_A \frac{Z_A e^2}{r_{iA}} + \frac{e^2}{4\pi\varepsilon_0} \int d\mathbf{r}' \frac{\rho(\mathbf{r}')}{|\mathbf{r} - \mathbf{r}'|}, \quad (12)$$

where $\rho(\mathbf{r}') = \sum_{j \neq i} |\psi_j(\mathbf{r}')|^2$ is the density of $(N-1)$ electrons. The obvious advantage of the Hartree approximation is that the partial differential equations have been *decoupled* and can be solved independently. However, despite offering decisive progress in dealing with many-electron systems, it ignores the anti-symmetry principle of electronic wave functions.

To cure this problem, in 1929 Slater²³ decided to construct the wave function as a (Slater) determinant of so-called one-electron spin orbitals:

$$\Psi(\mathbf{r}) = \frac{1}{\sqrt{N!}} \begin{vmatrix} \psi_1(\mathbf{r}_1) & \psi_2(\mathbf{r}_1) & \cdots & \psi_N(\mathbf{r}_1) \\ \psi_1(\mathbf{r}_2) & \psi_2(\mathbf{r}_2) & \cdots & \psi_N(\mathbf{r}_2) \\ \vdots & \vdots & \ddots & \vdots \\ \psi_1(\mathbf{r}_N) & \psi_2(\mathbf{r}_N) & \cdots & \psi_N(\mathbf{r}_N) \end{vmatrix}. \quad (13)$$

A spin orbital, ψ_i , is a function of the space and spin coordinates. Unless described otherwise, spin orbitals will be used interchangeably with one-electron wave functions in future texts. Furthermore, later in 1930 Fock²⁴ reduced the many-electron problem into a set of linear one-electron equations:

$$F\psi_i(\mathbf{r}) = \varepsilon_i \psi_i(\mathbf{r}), \quad (14)$$

which is later known as the Hartree-Fock (HF) equations. Here, F is the Fock operator which plays a role of a one-electron energy operator. Furthermore, the Fock operator consists of three terms:

$$F = h + \sum_{j=1}^N (J_j - K_j), \quad (15)$$

where

$$h = -\frac{\hbar^2}{2m} \nabla^2 - \frac{1}{4\pi\varepsilon_0} \sum_A \frac{Z_A e^2}{r_{iA}}, \quad (16)$$

$$J_j = \frac{e^2}{4\pi\epsilon_0} \int d\mathbf{r}' \frac{\psi_j^*(\mathbf{r}')\psi_j(\mathbf{r}')}{|\mathbf{r} - \mathbf{r}'|}, \quad (17)$$

$$K_j \psi_i(\mathbf{r}) = \frac{e^2}{4\pi\epsilon_0} \int d\mathbf{r}' \frac{\psi_j^*(\mathbf{r}')\psi_i(\mathbf{r}')}{|\mathbf{r} - \mathbf{r}'|} \psi_j(\mathbf{r}). \quad (18)$$

The operator h describes an electron's kinetic energy and its potential energy due to its interactions with all M nuclei surrounding it. The second term, $\sum_{j=1}^N J_j$, is called the Coulomb term and represents the potential energy of an electron due to an average field created by all N electrons in the system. The third term, $\sum_{j=1}^N K_j$, is called the exchange term, and its existence mirrors the antisymmetry of the wave function. Note that when $j = i$, an electron will have non-physical self-interactions from the Coulomb and exchange terms, but these two terms are conversely equal and cancel each other. Furthermore, as detailed in Eq. (18), a single operator K_j acting on a spin orbital ψ_i will "swap" the electrons in ψ_i and ψ_j . The exchange term is a purely quantum mechanical effect and has no classical analogy.

To solve Eq. (14) several sophisticated algorithms have been developed but will not be described in detail here. Nevertheless, the integro-differential HF equations have to be solved self-consistently, so the solving process starts with a set of trial spin orbitals for calculating the Fock operator, and then the HF equations are solved for a new set of spin orbitals that repeat the solving process recursively until all spin orbitals converge. Furthermore, Roothaan and Hall in 1951 proposed how to solve the HF equations by employing more general, non-orthogonal basis functions to construct spin-orbitals and transforming the original HF integro-differential equations into algebraic equations,²⁵ which is computationally more practical to implement.

Due to the use of the Slater determinant, the HF method has been a prominent and reliable tool in quantum chemistry since the time it was formulated. However, since the elements of the exchange term matrix are obtained from two-electron integrals of basis functions, the HF method scales as N^4 , where N is the number of basis functions. By doubling the number of basis functions, the computational cost, i.e., time, memory, etc., will roughly increase by a factor of $2^4 = 16$. This restricts the HF method to modestly sized molecular systems.

Still, electronic correlation is missing in the HF theory. Regardless of the spin states, electrons repel each other through the Coulomb force of individual electrons, not their average density. The missing electronic correlation is more clearly seen by looking at the Hartree products that construct the Slater determinant. A Hartree product implies that the probability of simultaneously finding all electrons at their given positions is the products of probabilities of individual electrons.

Although electronic correlation, or sometimes called Coulomb correlation, is easy to comprehend, it is very hard to formulate and then to solve. The simplest mathematical definition can be written as the difference between the exact energy and the HF energy:

$$E^{\text{corr}} = E^{\text{exact}} - E^{\text{HF}}. \quad (19)$$

Due to this missing electronic correlation, the results from the HF method often deviate significantly from the experimental data. When applied to solids, the HF method may behave even worse because it wrongly predicts that simple metals, which are modeled using free electrons, are insulators.²⁶

Luckily, in most of the molecular systems made up by light atoms the effect of the electronic correlation is not that strong.²⁷ Therefore, the HF method works quite well for this kind of systems, especially organic molecular compounds.²⁶ More sophisticated methods, however, have been developed based on the HF method to include the electronic correlation, such Møller-Plesset perturbation theory,²⁸ configuration interaction,^{27,29} etc., but will not be discussed further here.

Another approach commonly used in quantum chemistry and physics is density-functional theory (DFT). Unlike the two previous approaches, DFT utilizes the electron density instead of the wave function and bases its formulation on two surprisingly simple theorems proposed by Hohenberg and Kohn.³⁰ First, the external potential, and hence the total energy, of any interacting system is a unique functional of the ground state electron density. So, by knowing the ground state density of the system of interest, the Hamiltonian is fully determined and the many-electron wave functions can be obtained. Second, the total energy functional can be defined in terms of the density and only be minimized globally by the true ground-state density. The proofs of both theorems can be found in many textbooks.^{29,31}

Despite their robustness, the two theorems do not provide any practical implementation on how to calculate the exact density and the corresponding exact energy functional. To make DFT practicable as a quantum chemistry tool, Kohn and Sham proposed a further approximation by utilizing an auxiliary system of non-interacting electrons³²:

$$H_{\text{aux}} = -\frac{\hbar^2}{2m} \nabla^2 + V(\mathbf{r}). \quad (20)$$

Up to this point we do not make any assumption on how $V(\mathbf{r})$ should look like. The associated density of this auxiliary system is given by:

$$\rho(\mathbf{r}) = \sum_{i=1}^N |\psi_i(\mathbf{r})|^2. \quad (21)$$

Here, ψ_i represent one-electron orbitals, known as Kohn-Sham (KS) orbitals, in terms of which the kinetic energy of non-interacting electrons, T_s , can be written as

$$T_s[\rho] = \int d\mathbf{r} \psi_i^*(\mathbf{r}) \left(-\frac{\hbar^2}{2m} \nabla^2 \right) \psi_i(\mathbf{r}). \quad (22)$$

Furthermore, the KS idea is to use the density of the auxiliary system to represent the density of the many-body system, so the Coulomb interaction energy between electrons, i.e., the Hartree energy (E_H), can be represented as:

$$E_H[\rho] = \frac{e^2}{8\pi\varepsilon_0} \int \int d\mathbf{r} d\mathbf{r}' \frac{\rho(\mathbf{r}) \rho(\mathbf{r}')}{|\mathbf{r} - \mathbf{r}'|}, \quad (23)$$

and total energy functional of the given interacting-electron system as:

$$E[\rho] = T_s[\rho] + \int d\mathbf{r} V_{\text{ext}}(\mathbf{r}) \rho(\mathbf{r}) + E_H[\rho] + E_{\text{XC}}[\rho], \quad (24)$$

where V_{ext} is the potential energy due to all nuclei in the system and E_{XC} is the so-called exchange-correlation energy functional. The latter is the most enigmatic term in DFT and various methods have been developed to approximate E_{XC} . Unlike the HF method, the KS approach also cleverly anticipates E_{XC} and separates it from the rest to allow its systematic improvement.

Using the variational principle and the Lagrange multiplier to enforce the orthogonality of the KS orbitals, one derives a set of linear one-electron equations, known as the Kohn-Sham (KS) equations:

$$H_{\text{KS}}\psi_i(\mathbf{r}) = \varepsilon_i\psi_i(\mathbf{r}), \quad (25)$$

where H_{KS} is the same Hamiltonian given by Eq. (20) and the potential is now given by

$$V(\mathbf{r}) = V_{\text{ext}}(\mathbf{r}) + \frac{dE_H}{d\rho(\mathbf{r})} + \frac{dE_{\text{XC}}}{d\rho(\mathbf{r})} = V_{\text{ext}}(\mathbf{r}) + V_H(\mathbf{r}) + V_{\text{XC}}(\mathbf{r}). \quad (26)$$

The simplest approximation to E_{XC} , which was also firstly introduced by Kohn and Sham,³² is called the local density approximations (LDA). Here, the exchange-correlation energy of a given system is approximated with the one of the homogenous electron gas with the same density. This means E_{XC} only depends on the (local) density at each point in the system:

$$E_{\text{XC}}^{\text{LDA}}[\rho] = \int d\mathbf{r} \rho(\mathbf{r}) \varepsilon_{\text{XC}}\left[\rho(\mathbf{r})\right] \quad (27)$$

ε_{XC} is usually separated into two terms, namely the exchange and correlation terms, i.e., $\varepsilon_{\text{XC}}(\rho) = \varepsilon_{\text{X}}(\rho) + \varepsilon_{\text{C}}(\rho)$. In this case the exchange term is represented analytically by the Dirac functional³³:

$$\varepsilon_{\text{X}}(\rho) = -\frac{3}{4} \left(\frac{3}{\pi} \right)^{\frac{1}{3}} \rho(\mathbf{r}). \quad (28)$$

$\varepsilon_{\text{C}}(\rho)$, however, does not have an analytical form but has been accurately determined by quantum Monte Carlo calculations and then parameterized.³⁴ Despite its primitive assumptions, namely slowly varying densities, LDA works surprisingly very well with many systems, even for atoms and molecules where densities do not vary slowly, the reason being some error cancellation from the exchange and correlation terms.^{35–38} A better approximation to E_{XC} than LDA is the so-called generalized gradient approximation (GGA) for which the functional also depends on the gradient of density:

$$E_{\text{XC}}^{\text{GGA}}[\rho] = \int d\mathbf{r} \rho(\mathbf{r}) \varepsilon_{\text{XC}}[\rho(\mathbf{r}), \nabla\rho(\mathbf{r})]. \quad (29)$$

More advanced approximations to E_{XC} have also been developed with their advantages and disadvantages. For more information on this topic, readers may refer to, for instance, Ref. 31.

The reader will recall that, in order to solve the electronic structure of many-body systems, all of the three methods presented above aim for downsizing many-body problems into one-electron problems, such that one-electron wave functions and their eigen energies are the products. In the next sections, we will show further, mostly within the DFT framework, how this simplification to one-electron problems has greatly advanced the exploration of the electronic structure of many materials.

It goes without saying that, in order to solve one-electron equations for their wave functions, basis functions are needed. In general, there are two kinds of basis functions, namely extended and localized functions. Plane-waves (PWs) belong to the former kind, whereas any type of atomic orbitals (AOs) to the latter. The combination of the former and the latter, through mixing or augmentation, is also possible as basis functions. These different basis sets have their own advantages and disadvantages and depending on the nature of the system, one type can be more beneficial than the other. In the coming sections, we will focus on plane-waves due to their simple application, and atomic orbitals, which are the natural basis functions for chemical bonding analysis and for extracting various kinds of chemical information.

3.07.1.4 More complicated molecules, LCAO in general

When going from a simple molecule such as H₂ to more complex ones, things naturally get more complicated. With more orbitals to optimize, more electrons and their interaction among each other, more nuclei to include into the calculation, more approximations are needed, as illustrated in this and the following sections.

The size of the system that can be examined within the quantum-mechanical framework in reasonable time is naturally limited due to computational resources. Still, the study of small molecules can give us new insights into much larger problems, for example,

the enzyme family of nitrogenases which are metalloproteins that convert nitrogen and hydrogen into ammonia,^{39–41} an essential step in the biosynthesis of amino acids and, therefore, for plants and animals. The industrial Haber-Bosch process of the ammonia synthesis requires temperatures up to 500 °C and pressures up to 350 bar for that reaction.⁴¹ In contrast, the bio-catalyzed reaction occurs at standard conditions due to the special structure of nitrogenases containing iron sulfide units acting at the active sites.⁴⁰ Let us look at the quantum-chemical study of a diatomic sub-unit of FeS to improve our general understanding of proteins like nitrogenases. We will only concentrate on the so-called MO scheme and a qualitative representation of the molecular orbitals, modeled from results of an ab initio Hartree-Fock calculation,^{42,43} for didactic purposes. As seen from Fig. 3, the MO scheme for the $^5\Delta$ experimental state⁴⁴ (it is not $^5\Sigma$ as one might assume) for FeS contains many more interactions between the valence atomic orbitals than in the simple H₂ case. Three bonding (1σ , $2 \times 1\pi$), three non-bonding ($2 \times 1\delta$, 2σ) and three antibonding molecular orbitals ($2 \times 2\pi^*$, $3\sigma^*$) can be expected and their possible shapes are depicted in Fig. 3. The orbital character of 1σ and $3\sigma^*$ is primarily dominated by S 3 p_z and Fe 3 d_{z²} (with little Fe 4s character), whereas 1π and $2\pi^*$ consist of an interaction between one of the other S 3p and other Fe 3d orbitals. The nonbonding 1δ level remains a Fe 3d level, since there is no symmetry-related orbital from S. The nonbonding 2σ shows symmetry-given interaction between Fe 4s and 3 d_{z²} orbitals.

For such complex diatomic molecules, we express the LCAO ansatz quite generally:

$$\Psi_j(\mathbf{r}) = \sum_{\mu=1}^n c_{\mu j} \psi_{\mu}(\mathbf{r}). \quad (30)$$

The AOs are solutions of the Schrödinger equation for hydrogen-like atoms. For an exact representation, an infinite number of basis function terms would be needed, but obviously this is not a practical idea in reality.

If we intend to use Hartree-Fock theory for such complex molecules, the Roothaan-Hall formalism (see above) then leads to matrix eigenvalue equations

$$\mathbf{FC} = \mathbf{SC}\epsilon, \quad (31)$$

where F, the Fock matrix, is the matrix representation of the Fock operator, C is the square matrix of the expansion coefficients, S the overlap matrix of two orbitals and ϵ is a diagonal matrix containing orbital energies.^{11–13,24,45}

Not only can the LCAO approach be employed within the MO framework. Instead, in case of periodic ("infinite") systems like crystals, the many AOs will find together to *crystal* orbitals (CO), which is also dubbed as tight binding approach in physics, as covered in the next sections.

3.07.1.5 Plane Waves and Bloch's theorem

Translationally invariant, that is, periodic systems (= crystals), at least theoretically, contain an infinite number of atoms. At first sight, these extended systems seem to be nearly impossible to solve when using local orbitals, say using the HF approach. Plane waves (PW) are a way to get out of this misery simply because of their delocalized nature to describe periodic systems.

Plane waves are solutions of the Schrödinger equation under application of a constant external potential to approximate the behavior of a wave function for the interatomic region or interstitial sites in a crystal by a single plane wave, however, this will not describe the atomic local characteristic in a satisfying way. Bloch's theorem naturally introduces plane waves as

$$\Psi_k(\mathbf{r} + T) = \Psi_k(\mathbf{r}) e^{ikT}, \quad (32)$$

so that by applying the translation T to a wave function (Bloch function) $\Psi_k(\mathbf{r})$ depending on a wave vector k , it is unchanged, except for a phase factor incorporating the periodicity of the system.

The idea behind Bloch's theorem can be better understood after having a look at Fig. 4: all knowledge about the system is contained in the unit cell (marked with blue), and the rest of the system can be replicated by exploiting the translational symmetry. Likewise, the total wave function can be expressed in terms of plane waves

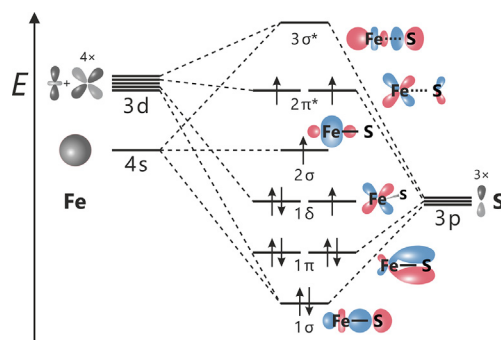


Fig. 3 MO scheme for the iron sulfide molecule with its different orbitals.

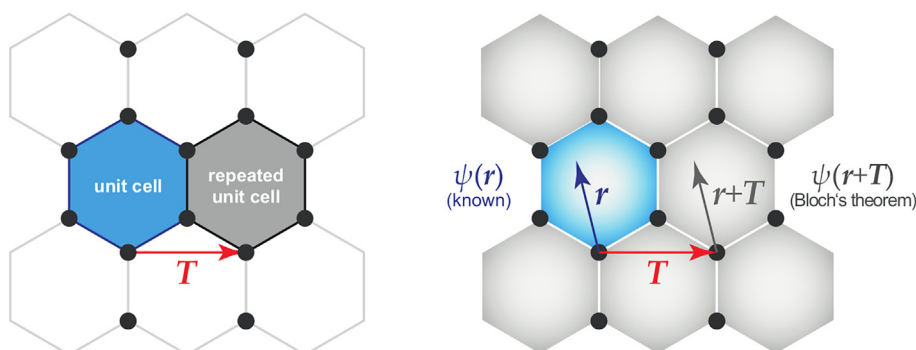


Fig. 4 Pictorial representation of Bloch's theorem. A 2D, hexagonal sheet of atoms (dark circles). Only the (blue) unit cell needs to be known, the rest of the system can be constructed from the translational symmetry, described by the translation vector \mathbf{T} . Reprinted from *Comprehensive Inorganic Chemistry II*, Vol. 9, V. L. Deringer, R. Dronskowski, Computational Methods for Solids, pp. 59–87, Copyright (2013), with permission from Elsevier.

$$\Psi_k(\mathbf{r}) = \frac{e^{i\mathbf{k}\mathbf{r}}}{\sqrt{\Omega}} \sum_{G=0}^{\infty} c_k(G) e^{iG\mathbf{r}} \quad (33)$$

and including the reciprocal lattice vector \mathbf{G} and the volume of the unit cell in real space Ω . c_k are a set of PW basis set coefficients, not to be confused with the LCAO coefficients. This linear combination of plane waves improves the description of the wave function in vicinity of the atomic nuclei. The crystal orbital can also be expanded by a linear combination of atomic orbitals (LCAO-CO), just like in the molecular case (see. Eq. 30), with the Bloch sum $\psi_{\mu k}(\mathbf{r})$

$$\Psi_k(\mathbf{r}) = \sum_{\mu=1}^n c_{\mu k} \psi_{\mu k}(\mathbf{r}), \psi_{\mu k}(\mathbf{r}) = \frac{1}{\sqrt{N}} \sum_{\mathbf{R}} e^{i\mathbf{k}\mathbf{R}} \psi(\mathbf{r} - \mathbf{R}) \quad (34)$$

where \mathbf{R} is the real-space lattice vector and N is the number of lattice sites. When comparing Eqs. (33) and (34), one realizes that any local function can be expressed as a linear combination of (ideally infinite) plane waves and vice versa.^{46–49}

3.07.1.6 One-dimensional systems

Despite the generality of Bloch's theorem and its associated plane waves of sine or cosine (i.e., essentially delocalized) character, it is straightforward to give it a very local and chemical meaning. If we assume that atoms are building up the entire crystal, we can quickly write down a Bloch sum in which the extended wave function (the crystal orbital) is expanded in those atomic orbitals we already know from molecular quantum chemistry. Our friends from the physics community are doing essentially the same thing, and then this goes under the name “tight-binding approach”.⁵⁰ Please note that this term does *not* imply that the *atoms* are tightly bound to each other; on the contrary, it means that the *electrons* are so tightly bound to its parent atoms that the original one-electron atomic wave functions (the atomic orbitals) still serve us pretty well, at least well enough to handle the system. In other words, the chemical interaction between the atoms is the perturbation, hence this approach directly targets chemical bonding.

For a one-dimensional system of hydrogen atoms, the linear-combination-of-atomic-orbitals-to-crystal-orbitals (LCAO-CO) Bloch construction then reads

$$\psi_k = \sum_{n=1}^N e^{ikna} \varphi_n, \quad (35)$$

in which we have expanded the atomic orbitals φ_n (1s atomic orbitals in this case) into a crystal orbital ψ_k which now depends on the quantum number k derived from reciprocal space. The interatomic distance is given as multiples of a (say, 1 Å), and the atomic orbitals are numbered from 1 to N (the total number of unit cells per crystal). It would be very time-consuming to calculate the course of ψ_k over the entire reciprocal space but we might want to do that only at a few, “representative” k points or, simpler still, just look at the band's energetic behavior at the center of reciprocal space called Γ ($k = 0 \times 2\pi/a = 0$) and at its outer edge X ($k = 1/2 \times 2\pi/a = \pi/a$), thereby defining the size of the so-called *Brillouin zone* (the unit cell of reciprocal space). At Γ , the exponential function equals unity, so the crystal orbital ψ_k is nothing but the sum of the individual atomic orbitals, $\varphi_1 + \varphi_2 + \varphi_3 + \dots$, clearly the bonding combination of atomic orbitals, and thus should be lowest in energy. At X , when k equals π/a , the exponential term alternates between +1 and -1, so the crystal orbital will read $-\varphi_1 + \varphi_2 - \varphi_3 + \dots$, the antibonding highest-energy combination. The qualitative plot including sketches of the crystal orbital is depicted in Fig. 5 (left), the one-dimensional analog of the molecular orbital diagram of the H₂ molecule. Exactly in the middle of the Brillouin zone, between Γ and X , we have also indicated that the crystal orbital carries nodes at every third H atom. The dispersion of the band structure, that is, the energy difference between highest and lowest energy, increases if the interatomic distance shrinks because it scales with the orbital overlap or orbital interaction, to be precise.

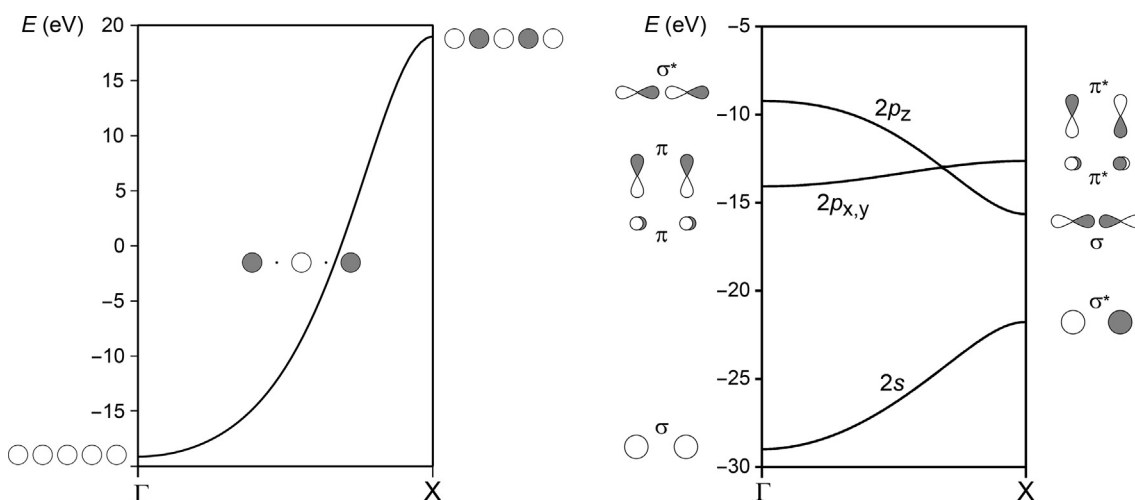


Fig. 5 One-dimensional band structure of the infinite hydrogen chain spaced at 1 Å (left) and the infinite nitrogen chain spaced at 2 Å (right). The characters of the bands have been pictorially indicated. Reprinted from Dronskowski, R. *Computational Chemistry of Solid State Materials: A Guide for Materials Scientists, Chemists, Physicists and Others*. Wiley-VCH: Weinheim (2005) with permission from John Wiley and Sons.

The band structure of a one-dimensional chain of nitrogen atoms looks a little more complicated but follows the same procedure upon computational construction. Let us include the one 2s and the three 2p valence orbitals of nitrogen and let us also assume an N–N distance of 2 Å, then Fig. 5 (right) provides the respective band structure. Similar to the 1s crystal orbital of hydrogen, the 2s crystal orbital of nitrogen moves up in energy upon going from Γ to X but the dispersion is much smaller due to the wider N–N distance and the more contracted 2s atomic orbital. Likewise, the π -like crystal orbitals arising from the 2p_x and 2p_y atomic orbitals move up in energy but their dispersion is even weaker, simply due to the less efficient π -like orbital interaction. The crystal orbital that is generated by the 2p_z orbitals of nitrogen, however, is quite different. Not only is its dispersion comparable to 2s, the trivial reason being the σ -like orbital overlap, but the electronic band runs down from Γ to X, easily understandable by the orbital icons; this very crystal band is antibonding at Γ but bonding at X. In other words: while the orbital overlap controls the band's dispersion, its topology (going up or down) is determined by the orbital symmetry.⁵¹ As regards symmetry, please also note that we have simplified things a little because a careful analysis shows that the 2s and the 2p_z bands transform according to the same irreducible representation (i.e., have identical symmetry properties), so they mix. As a consequence, the lower band dubbed 2s also carries a little 2p_z contribution whereas the upper 2p_z band also contains some 2s admixture. The closer they become in energy (that is, the more they approach the X point), the stronger the mixing.

It is rather trivial to extend this to atoms with other orbital symmetries such as 3d, and it is also trivial to allow for more than one atom per unit cell because the LCAO-CO expansion then simply includes additional terms; nothing changes, at least not fundamentally.²⁶ Likewise, we can go to higher dimensions such as two or three. For a quadratic system (say, a checkerboard of carbon atoms) the Brillouin zone of reciprocal space would also be quadratic, and we would analyze the various bands at more "special" points, not only at the very center which still reads Γ ($k_x = k_y = 0$) but also at X ($k_x = \pi/a, k_y = 0$) and Y ($k_x = 0, k_y = \pi/a$) and M ($k_x = k_y = \pi/a$), for example. For a three-dimensional (primitive) cubic crystal, the special points of reciprocal space would then be Γ ($k_x = k_y = k_z = 0$), X ($k_x = \pi/a, k_y = k_z = 0$), M ($k_x = k_y = \pi/a, k_z = 0$), and R ($k_x = k_y = k_z = \pi/a$), nothing to really worry about.

And yet, a new phenomenon pops up for the simplest system, the one-dimensional chain of hydrogen atoms. Fig. 6C shows what we have seen before in Fig. 5 (left), namely the corresponding band structure of that hydrogen chain. Here, the lattice parameter a' comprises just one H atom per unit cell. If we were to *double* this lattice parameter to a new $a (= 2 \times a')$ such that the unit cell contains two H atoms, there would also be two bands in the band structure, as shown in Fig. 6B. Mathematically, this is a trivial operation which may be graphically symbolized by "folding back" half of the crystal orbital seen on the right. Now, it is highly instructive to compare the doubly degenerate upper and lower crystal orbitals at the X point in (B), and they match the crystal orbital in the very center of the Brillouin zone of (C). The crystal-orbital icons at X indicate that both bands not only differ by a phase shift, they also have the same crystal symmetry because both are *symmetric* with respect to the hydrogen chain's horizontal mirror plane. As a fundamental consequence, both bands must *interact* for this very electron count (1 electron per crystal orbital) of the H chain and will *repel* each other.

We are witnessing what was first predicted by Peierls⁵² and goes under his name, the famous Peierls distortion, a spontaneous symmetry lowering arising for a half-filled band of a one-dimensional system. Because upper and lower bands "repel" each other (strongly so at X, but the weaker the more we immerse into the Brillouin zone), there results a distortion which leads to a shorter H–H distance (say, 0.8 Å) and a longer one (say, 1.2 Å). Alternatively expressed, the one-dimensional hydrogen chain collapses into a loose chain of H₂ molecules, and this is the reason why the lower band has the character of the bonding σ_g molecular orbital whereas the upper band stands for the σ_u^* molecular orbital, both depicted in Fig. 5A.

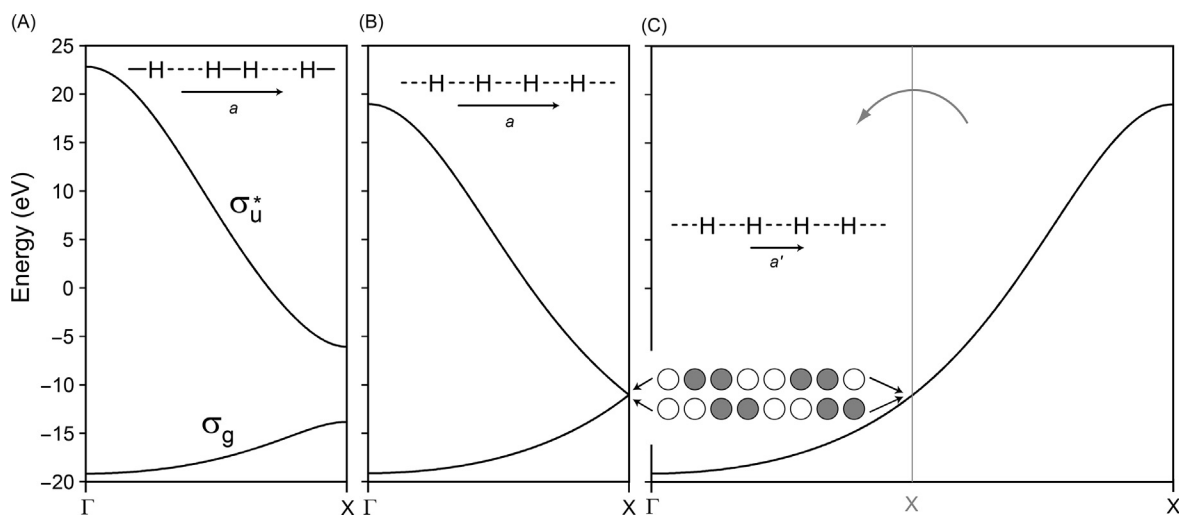


Fig. 6 As in the left part of [Fig. 5](#) but drawn differently, with two H atoms per unit cell, subfigure (B), and again with one H atom per unit cell, subfigure (C). Because of energetic degeneracy for half-filling (Peierls case) the one-dimensional system structurally distorts to yield shorter (0.8 Å) and longer (1.2 Å) H–H distances, given in subfigure (A), and lowers its total energy. Reprinted from Dronskowski, R. *Computational Chemistry of Solid State Materials: A Guide for Materials Scientists, Chemists, Physicists and Others*. Wiley-VCH: Weinheim (2005) with permission from John Wiley and Sons.

Chemists will not at all be surprised that a one-dimensional hydrogen system will turn into isolated H_2 molecules but this should not belittle the fundamentality of the Peierls scenario. It is a general phenomenon where some translational symmetry is lost and leads to a lower-energy, more stable system. It may also be regarded as the solid-state equivalent of the older and likewise famous Jahn-Teller instability⁵³ sometimes found for molecular systems; here, the resulting energetic stabilization also results from coupling the nuclear coordinates with the electronic structure but the system is lowered in point-group symmetry.

It has long been thought that the Peierls scenario is strictly valid only for one-dimensional systems but intense research has shown that Peierls distortions are found for two-dimensional as well and also for three-dimensional systems.^{54,55} Even some of the simple structures of the elemental solids may be regarded as having resulted from previous Peierls distortions without noticing the (high-symmetry) aristotypes from which they have originated. We simply “got used” to the low-symmetry structures and overlooked the high-symmetry ones. For example, the element tellurium with its helical chains of Te atoms is the result of a three-dimensional Peierls distortion away from a simple cubic (α -Po type) structure, and here the bands have been filled by 2/3 and, hence, backfolded three times in reciprocal space.⁵⁶

3.07.1.7 Concept of charges and bonding Indicators (COOP and COHP)

To more quantitatively characterize chemical bonds in terms of their covalent and ionic character, numerical bonding indicators come into play. For an ionic bond, it is pretty straightforward to use the ionic charges for quantification. The cohesive forces in an ionic compound stem from the electrostatic force (also called Coulomb force) caused by the interaction of like and unlike charged ions. As already alluded to in the introductory section, the formation of ions occurs when the difference in the electronegativity (ΔEN) of the particular atoms is so large that the valence electron(s) of one atom is transferred to the other atom, forming a cation and an anion, respectively. The electrostatic interaction between ions with unlike charges is attractive and the one between ions of like charge is repulsive. This charge concept has been around for a long time⁵⁷ and two of the most famous wave function based methods to partition electrons and assign charges to atoms are the Mulliken and Löwdin population analyses.^{58–60} It has recently become possible to extract atomic charges and orbital populations from plane waves,^{61,62} too, so we will cover the population analyses in reciprocal space. Such technique for Mulliken and Löwdin population analysis is computationally cheap and yields reasonable charges.^{61,63,62} In more general terms, if the crystal wave function $\psi(\mathbf{k})$ is constructed as a linear combination of atomic orbitals $\chi_\mu(\mathbf{k})$ in the LCAO-CO approximation,^{45,64} the so-called gross population (GP), a measure for the orbital occupation, can be calculated from the LCAO coefficients such that the Mulliken or Löwdin charge for an atom A is obtained from the difference of the number of the atom's valence electrons N (when using pseudopotentials) and the gross (orbital) population GP_μ

$$q_A = N - \sum_{\mu \in A} GP_\mu. \quad (36)$$

Clearly, charge information is useful for understanding and designing new (functional) materials, like batteries or thermoelectrics, or to find new compounds for phase-change materials. In the quantum-chemical community, both Mulliken and Löwdin charges are often understood as being highly basis-set dependent due to the changing locality of the basis functions, but this problem no longer persists with plane waves as a consequence of their nonlocality.

Simple textbook-like examples to illustrate the functionality of Mulliken (or Löwdin) charges are NaCl and CsCl, two iconic ionic cases. In both cases, depicted in Fig. 7, NaCl in its experimental, room-temperature structure with space group $Fm\bar{3}m$ and CsCl with $Pm\bar{3}m$, the cations Na and Cs show the expected charges of around +1, whereas the Cl anion exhibits a charge of around -1, depicting the typical ionic picture expected for alkaline metal halides.

We reiterate that methods like the one of Mulliken or Löwdin are wave function-based. There are also (real-space) density-based charge analysis methods, such as the one by Bader within the Atoms in Molecules (AIM) framework.^{65,66} The density-based technique shall guarantee uniqueness, but comes with the cost of losing the wave function's phase (sign) information. Instead, the topology of the electron density $\rho(r)$ is used to partition the system into a set of volume elements V , corresponding to atoms. By calculating the so-called zero-flux surfaces, contour maps of the atomic electron density are obtained, and integration of the electron density within a certain (atomic) volume element for atom A with nuclear charge Z_A , the charge arrives at

$$q_{A,\text{Bader}} = Z_A - \int_{V \in A} \rho(r) dr. \quad (37)$$

Since the Bader charge analysis does not allow for atoms to overlap, caution is advised,^{61,63} especially in covalent compounds, where orbital overlap is significant.

The impact of the electrostatic forces is captured by the Madelung energy,^{67–71} which may be used to estimate the stability of ionic compounds.^{61,72} In the case of molecular crystals or intermetallic compounds with small ionic contributions, the real charge is unclear, so Madelung energies cannot be accessed easily unless quantum-chemically derived charges are calculated.

Coming back to the covalent bond, its idea is strongly linked to the Lewis model of the electron pair bond formed between two atoms with similar electronegativities.⁷³ It gives a first quantitative measure of the bond strength in, say, organic molecules where C–C single, double, and triple bonds are possible. In the hands of a skilled chemist, this model enables the understanding and prediction of stability and reactivity of the molecule or certain functional groups. However, as electrons repel each other, a model that is based purely upon the electron density does not explain the quantum chemical situation to a satisfying extent. We also recall that the density lacks any phase information. Accordingly, distinguishing between bonding and anti-bonding interactions is not possible per se. As such, wave function-based methods are required.

In molecular systems, the orbital overlap and Hamilton integrals $S_{\mu\nu}$ and $H_{\mu\nu}$ are used to quantify the strength of a covalent bond.

$$S_{\mu\nu} = \int \phi_\mu \phi_\nu dt; \quad H_{\mu\nu} = \int \phi_\mu \hat{H} \phi_\nu dt \quad (38)$$

As solid-state materials are translationally invariant, this feature has to be respected when bonding indicators for these materials are formulated. Eq. (38) must somehow include the quantum number k that defines the position in the reciprocal space originating from Bloch's theorem (section 3.07.1.5). The resulting band structures, introduced in section 3.07.1.6, will now serve to introduce the bonding indicators for the solid state.

Before we dive into the concept of bonding, another difficulty of the band structure plots must be solved. For one-dimensional crystals such as the linear hydrogen chain, the choice of the path through the Brillouin zone seems obvious, from the Γ point to the X point. For two- and three-dimensional crystals, any path is equally valid because here, k is a vector with two or three dimensions, respectively. The solution to this issue is the integration of the band structure over the entire reciprocal space which results in the density of states (DOS). The DOS yields information on the number of states (actually, one-electron levels) in a given energy interval and its value is inversely proportional to the slope of the band structure.

$$\text{DOS}(E) \propto \left(\frac{\partial E}{\partial k} \right)^{-1} \quad (39)$$

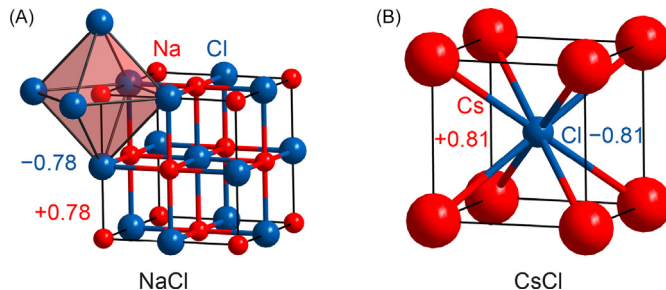


Fig. 7 Mulliken charges of NaCl and CsCl. Reproduced with permission from Ertural, C.; Steinberg, S.; Dronskowski, R., Development of a Robust Tool to Extract Mulliken and Löwdin Charges From Plane Waves and Its Application to Solid-State Materials. *RSC Adv.* **2019**, 9 (51), 29821–29830—Published by The Royal Society of Chemistry.

For chemical bonding analysis, however, the DOS is not an appropriate tool as it only shows the position of levels, and not the way they interact. The information on bonding and anti-bonding can be introduced by including an additional quantity. The first approach is the crystal-orbital overlap population (COOP) by Hughbanks and Hoffmann which premiered in 1983.⁷⁴

$$\text{COOP} = S_{\mu\nu} \sum_{j,k} w_k c_{\mu,jk}^* c_{\nu,jk} \delta(\varepsilon_j(\mathbf{k}) - E) \quad (40)$$

COOP is an overlap-weighted density of states and corresponds to the two-center case of the Mulliken population analysis in the solid. Positive values of the COOP are interpreted as bonding levels, while negative values are attributed to antibonding ones. When the COOP is integrated over the energy up to the Fermi-level, the ICOOP is achieved, to be understood as the bond population or number of electrons that occupy the covalent bond.

Fig. 8 shows the band structure of the linear hydrogen chain from **Fig. 5**, but with color coded bonding information of the 1s-orbitals. It consists of strictly bonding interactions at the Γ point that becomes fully antibonding at the X point. When the band structure is then integrated over reciprocal space, the density of states is achieved which, when multiplied with the overlap integral, results in the COOP plot on the right-hand side of **Fig. 8**. This plot can easily be explained by the orbital interactions shown in the band structure. At -8 eV, the H–H interaction has its maximum in the bonding region as all orbitals are in phase. With increasing energy, the COOP decreases until it reaches zero at the Fermi level (0 eV) despite the existence of states in the DOS at this point, a consequence of the non-bonding type of interaction. With further increasing energy, the COOP indicates an antibonding interaction that reaches its maximum at 30 eV; here, the phases of the 1s-orbitals are strictly alternating so the interaction between two neighboring orbitals is always antibonding. In sum, the interaction in the linear hydrogen chain is bonding as all bonding levels below the Fermi-level are occupied and the antibonding ones are unoccupied.

Based on the COOP approach, the crystal-orbital Hamilton population (COHP)⁷⁵ was developed within density-functional theory which utilizes the Hamilton integral (hence its name).

$$\text{COHP} = H_{\mu\nu} \sum_{j,k} w_k c_{\mu,jk}^* c_{\nu,jk} \delta(\varepsilon_j(\mathbf{k}) - E) \quad (41)$$

The COHP is a partitioning scheme for the band structure energy that consists of the Kohn-Sham eigenvalues. Its appearance is very similar to the COOP with one important exception. Since the COHP is an *energetic* measure for the covalent bond strength, *negative* values indicate a bonding behavior while positive values are considered anti-bonding. The energy-integrated COHP (the ICOHP), is an energetic measure for the bond strength, but it does not equal the experimental bond energy because it only covers effective one-particle energies. In order to result in a formalism analogous to the COOP, negative COHP are plotted as a function of the energy. The general procedure is completely analogous to one-dimensional systems as it can be seen in **Fig. 9** for diamond which is a textbook example of covalency in the solid state.

Fig. 9 shows the schematic path from the band structure to the final bonding indicators. The band structure is analogous to the one-dimensional case of the linear hydrogen chain with one important exception: the quantum number k is replaced by a three-dimensional vector \mathbf{k} . This leads to an arbitrariness in the set-up of the path through the Brillouin zone (see discussion before) which usually follows certain high-symmetry points. However, this is done solely by convention and any other path is just as correct. A more unambiguous representation goes by the density of states which is derived from the band structure by integration over the whole Brillouin zone. That way, all \mathbf{k} -points are equally represented and the final result does not depend on their sequence. In the DOS, we encounter yet another convention: Chemists prefer to plot the energy as y-axis in order to illustrate the familiarity between DOS and band structure. Physicists, on the other side, plot the DOS with exchanged axes because mathematically, it is a function of the energy.

As said before, the DOS only tells us *where* the states are and not *what* they do, so an additional quantity must be incorporated, either the overlap matrix element $S_{\mu\nu}$ or the Hamilton matrix element $H_{\mu\nu}$, resulting in the COOP and COHP techniques. At low energies, the orbital interaction of 2s and 2p_{x/y/z} is strictly bonding. In the framework of valence bond theory, this interaction is

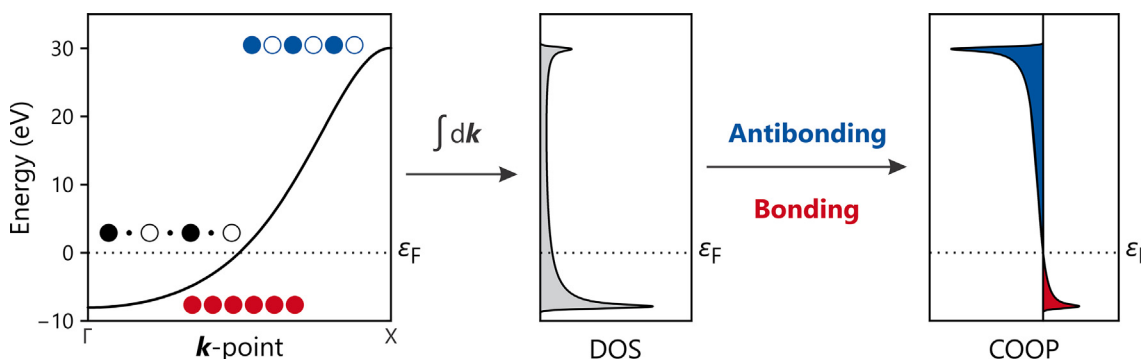


Fig. 8 Graphical derivation of the COOP. Left: Band structure of the linear hydrogen chain. Middle: Density of states (DOS) of the linear hydrogen chain. Right: Crystal orbital overlap population (COOP). The energy is relative to the Fermi-level.

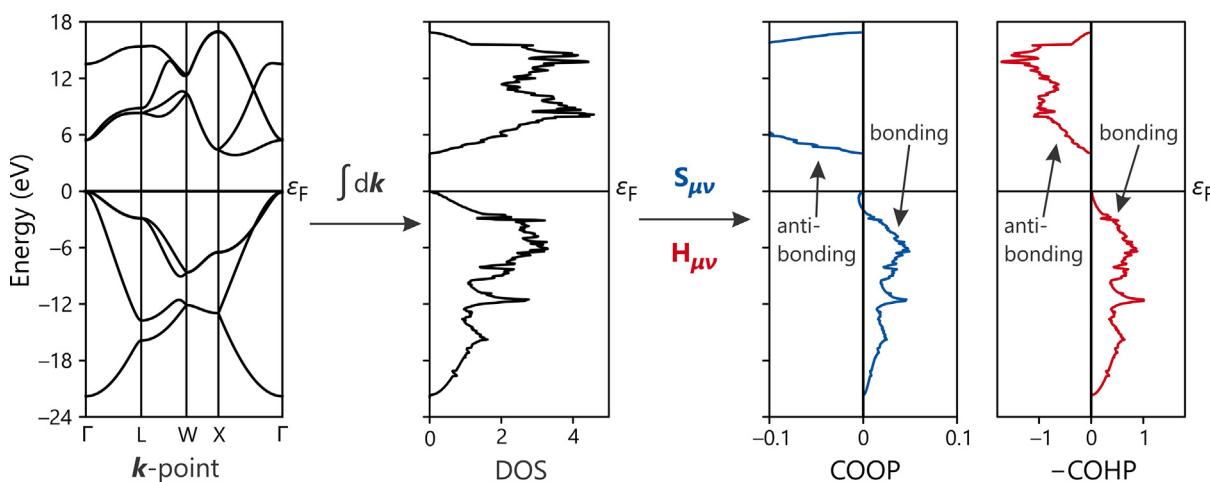


Fig. 9 Band structure, density of states, crystal orbital overlap population, and crystal orbital Hamilton population for diamond calculated using the LOBSTER program. The energy is shifted relative to the Fermi level. COOP and COHP are per bond.

formed by four sp^3 orbitals. The molecular orbital theory deals with less localized σ molecular orbitals that are formed by linear combination of one 2s and three $2p_{x/y/z}$ that are located on the carbon atoms. The bonding behavior persists up to the Fermi level, at least for the COHP. The COOP in Fig. 9 shows a very weak anti-bonding fraction, at least plausible by some over-estimation of anti-bonding seen above the Fermi level. In the COHP, this anti-bonding region is in the same order of magnitude, in fact it has the exact same integral as the bonding region, so both bonding and antibonding interaction cancel each other. This relation is quite reassuring as this is an analogy to molecular orbital theory where there is an antibonding (atomic orbital) interaction for each formed bonding AO-interaction.

In its original definition, the COHP suffered from a problem connected to its origin in the band energy. Within DFT, the total energy of a neutral system is constant for any arbitrary shift of the external electrostatic potential (i.e., the energetic zero-point). This does not apply to the band energy since it covers only the *electronic* energy, which refers to a charged system. The potential of a real crystal depends on its surface as well as its volume, but both have no meaning in the theoretical description of a solid-state material as it extends into infinity without any surface. Thus, the electrostatic potential has no physical meaning in a DFT framework and is usually defined arbitrarily. As a consequence, the comparison of (I)COHP of different crystal structures is highly questionable as they differ significantly in their Madelung fields. To solve this issue, a covalency energy E_{cov} was developed that subtracts the potential shift from the total COHP and arrives at a quantity that is supposed to be invariant towards said shifts.⁷⁶

$$E_{cov\ \mu,\nu} = \left(H_{\mu\nu} - \frac{H_{\mu\mu} + H_{\nu\nu}}{2} S_{\mu\nu} \right) \sum_j c_{\mu j}^* c_{\nu j} \delta(E - \varepsilon_j) \quad (42)$$

However, this issue can alternatively be solved when an orthonormal basis set is employed for the calculation of the COHP. Let us consider a Hamilton matrix element for an arbitrary electrostatic potential

$$H_{\mu\nu} = \langle \phi_\mu | \hat{H} | \phi_\nu \rangle \quad (43)$$

between two orbitals ϕ_μ and ϕ_ν . If the electrostatic potential is then shifted by a constant value of V_0 , this can be represented in the Hamilton integral by means of perturbation theory:

$$\begin{aligned} H_{\mu\nu}^{V_0} &= \langle \phi_\mu | \hat{H} + V_0 | \phi_\nu \rangle = \langle \phi_\mu | \hat{H} | \phi_\nu \rangle + \langle \phi_\mu | V_0 | \phi_\nu \rangle \\ &= H_{\mu\nu} + S_{\mu\nu} V_0 = H_{\mu\nu} \end{aligned} \quad (44)$$

The shift of the electrostatic potential does not affect the value of the Hamilton matrix element in case of an orthonormal basis set, that is $S_{\mu\nu} = 0$. This relation does not hold for on-site elements, as they have non-zero overlap:

$$\begin{aligned} H_{\mu\mu}^{V_0} &= \langle \phi_\mu | \hat{H} + V_0 | \phi_\mu \rangle = \langle \phi_\mu | \hat{H} | \phi_\mu \rangle + \langle \phi_\mu | V_0 | \phi_\mu \rangle \\ &= H_{\mu\mu} + S_{\mu\mu} V_0 = H_{\mu\mu} + V_0 \end{aligned} \quad (45)$$

This way, it is possible to compare *interatomic* COHP and ICOHP of different crystal structures without methodological errors that could render the final results useless. Although the mathematical formalism discussed above is quite straightforward, we will consider a number of systems in order to support it. Fig. 10 shows the ICOHP for several molecular compounds in gaseous as well as crystalline phases.

The ICOHP values of gaseous and crystalline molecules closely resemble a straight line, corroborating negligible impact of certainly differing electrostatic potentials. Another surprising feature of Fig. 10 is the separation of bonds that are qualitatively

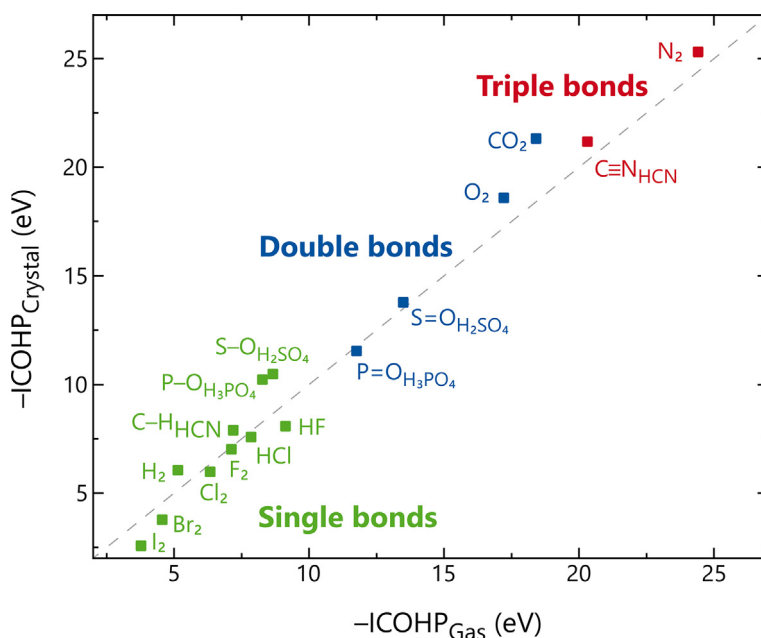


Fig. 10 ICOHP per bond for molecular compounds in crystalline and gaseous phase. The color code refers to the classically attributed bond order.

described as single, double and triple bonds. In the lower left corner, singly bonded molecules such as halogens, hydrogen halides, and S–O and P–O single bonds in sulfuric and phosphoric acid can be found with ICOHP values between -4.5 eV and -10 eV. The ICOHP value of diamond (-9.7 eV) fits very well into this context, as it is qualitatively interpreted as a single bond. At higher ICOHP, up to -20 eV, double bonds can be found as they exist in sulfuric and phosphoric acid as well as molecular oxygen and carbon dioxide. At even larger ICOHP values, the C–N and N–N triple bonds of hydrogen cyanide and molecular nitrogen form the upper end of the present example. Qualitatively speaking, the ICOHP values of classic double bonds are roughly twice as large as the single bonds and the ICOHP of triple bonds are approximately three times the size of single bonds. To a chemist, this correspondence comes to no surprise because a double bond includes twice the number of electrons as a single bond. However, this correlation between ICOHP as a quantitative bonding indicator and the long-known yet qualitative concept of bond multiplicity support the usefulness of the COHP as a measure for covalent bond strength.

3.07.2 Part II: Methods

3.07.2.1 Basis functions

A DFT calculation always starts with trial KS wave functions built with a set of basis functions, but how do we choose the most suitable basis set for our calculations? Since different kinds of bases have different mathematical properties, the most suitable basis for a given system is the one which fits the system. For instance, as described previously, PWs are periodic and naturally follow Bloch's theorem; therefore, they are suitable for crystalline systems with periodicity. On the other hand, local orbitals, such as atomic orbitals (AOs), are more appropriate for molecular systems because both are spatially localized. Nevertheless, it is not impossible to do the other way around, namely PWs for molecular systems and AOs for crystal systems, although this choice will be less efficient.

PWs are basically a combination of cosine and sine functions, which, thanks to Euler's identity, can be written compactly using a complex exponential: $e^{iG \cdot r} = \cos(G \cdot r) + i \sin(G \cdot r)$, here G and r , respectively, represent wavevectors and real-space positions. PWs also form a complete basis set, meaning that any real-space function in principle can be constructed by linearly combining PWs of different wavevectors. Another property of PWs is that they are orthonormal:

$$\frac{\Omega}{(2\pi)^3} \int d\mathbf{r} e^{i\mathbf{G} \cdot \mathbf{r}} e^{-i\mathbf{G}' \cdot \mathbf{r}} = \frac{\Omega}{(2\pi)^3} \int d\mathbf{r} e^{i(\mathbf{G}-\mathbf{G}') \cdot \mathbf{r}} = \delta_{\mathbf{G},\mathbf{G}'}, \quad (46)$$

where $\delta_{\mathbf{G},\mathbf{G}'}$ is the Kronecker delta and Ω is a large volume. In terms of PWs, the KS wave functions can be written as

$$\psi_{jk}(\mathbf{r}) = \frac{1}{\sqrt{\Omega}} \sum_{\mathbf{G}} C_{j(k+\mathbf{G})}^{\text{PW}} e^{i(k+\mathbf{G}) \cdot \mathbf{r}}, \quad (47)$$

where j and k , respectively, denote the band and crystal-wavevector indices, whereas $C_{j(k+\mathbf{G})}^{\text{PW}}$ are the PW coefficients. One can show that these wave functions also obey Bloch's theorem where the translationally invariant term $u_{jk}(\mathbf{r})$ is given by

$$u_{jk}(\mathbf{r}) = \frac{1}{\sqrt{\Omega_{\text{cell}}}} \sum_{\mathbf{G}} C_{j(k+\mathbf{G})}^{\text{PW}} e^{i\mathbf{G} \cdot \mathbf{r}}, \quad (48)$$

and Ω_{cell} is now the unit-cell volume. If we insert Eq. (47) into the original KS equations, they become:

$$\sum_{\mathbf{G}'} \left[\frac{\hbar^2}{2m} |\mathbf{k} + \mathbf{G}|^2 \delta_{GG'} + V(\mathbf{G} - \mathbf{G}') \right] C_{j(k+\mathbf{G}')}^{\text{PW}} = \varepsilon_j C_{j(k+\mathbf{G})}^{\text{PW}}. \quad (49)$$

Here, the first term of the left side represents the kinetic energy, whereas $V(\mathbf{G} - \mathbf{G}')$ is the Fourier transform (FT) of the potential given by Eq. (26). This simplicity in calculating the matrix elements of the kinetic energy and potential is one of the advantages of the PW basis.

Furthermore, since the PW basis is complete, in principle, the obtained wave functions will be exact if infinitely many PWs are used. In practice, however, a limited number of PWs must suffice due to the limitation of the computer memory. This will cause some inaccuracy of wave functions, especially the parts close to nuclei, one of the drawbacks of PWs. Fortunately, various methods, so-called pseudopotential methods, have been developed to soften the potential by dividing the electrons into the core and valence parts, so the pseudopotentials in the end reduce the number of PWs. The resulting wave functions are called pseudo-wave functions, which only accurately describe the valence part. These methods will be described in detail in a following section. Moreover, the number of PWs is set up through a parameter called the cutoff energy (E_{cut}) that determines the maximum kinetic energy of PWs allowed in a calculation:

$$\frac{\hbar^2}{2m} |\mathbf{k} + \mathbf{G}|^2 \leq E_{\text{cut}}. \quad (50)$$

This single parameter, which is another advantage of the PW basis, systematically controls the convergence of DFT calculations.

Unlike PWs, AOs, however, do not have a general form. Nevertheless, AOs can always be separated into two parts, namely, the radial and angular parts:

$$\phi_{nlm}(\mathbf{r}) \equiv \phi_{nlm}(r, \theta, \varphi) = R_{nl}(r) Y_{lm}(\theta, \varphi). \quad (51)$$

where, r, θ, φ are, respectively, the radius, polar, and azimuthal angles, whereas n, l, m are the principle, azimuthal, and magnetic quantum numbers. Here, Y_{lm} are spherical harmonics, which are orthonormal functions:

$$\int d\varphi d\theta \sin\theta Y_{lm}(\theta\varphi) Y_{l'm'}(\theta\varphi) = \delta_{ll'} \delta_{mm'}. \quad (52)$$

Cubic harmonics, however, are also often used for the angular parts because they yield real, instead of complex, values. The radial function $R_{nl}(r)$ determines how localized or "contracted" an AO is, whereas the spherical harmonics determine the symmetry or character of the AO. Eigenfunctions of a hydrogen atom are examples of AOs whose derivation and forms can be found in any quantum chemistry textbooks. One important property of hydrogen-like AOs is that they have nodes, i.e., crossing points through the radial axis, which are proportional to the principle quantum number n , the number of nodes being $n-l-1$ and l the angular momentum.

Various sets of AOs have been mathematically developed since the birth of quantum mechanics. However, the only part that differentiates them is the radial functions. Some of the earliest basis sets were calculated by Slater in 1930,⁷⁷ and unlike hydrogen-like AOs, Slater-type orbitals (STOs) do not have nodes since they are defined by taking the asymptotic form of the former at large distances:

$$R_{n\zeta}(r) = \frac{(2\zeta)^{n+1/2}}{\sqrt{(2n)!}} r^{n-1} e^{-\zeta r}. \quad (53)$$

Here, n is now called an *effective* principal quantum number, whereas the (contraction) exponent ζ is a quantity that is proportional to the nuclear charge and inversely proportional to n . In his paper Slater also tabulated n and ζ for many elements, and since then calculations of more complex systems have become feasible. The parameters n and ζ , however, need to be readjusted whenever the potential in a given system deviates significantly from the corresponding atomic potential.

Since AOs or local orbitals can also form a complete basis set, the KS wave functions can be constructed through a linear combination of atomic orbitals (LCAO):

$$\psi_{jk}(\mathbf{r}) = \sum_{\mu T} C_{\mu jk}^{\text{LCAO}} e^{i\mathbf{k} \cdot \mathbf{T}} \phi_{\mu}(\mathbf{r} - \mathbf{T}). \quad (54)$$

Here, μ represents all the orbital labels, i.e., $\{n, l, m\}$, whereas T denotes the lattice translation vectors. For molecular systems, the sum over T is omitted and the systems have no crystal-wavevectors. $C_{\mu jk}^{\text{LCAO}}$ are the LCAO coefficients. An AO basis may or may not be orthogonal. Two non-orthogonal AOs separated by a distance R can have an overlap given by

$$S_{\mu\nu}^R = \int d\mathbf{r} \phi_{\mu}(\mathbf{r}) \phi_{\nu}(\mathbf{r} - \mathbf{R}), \quad (55)$$

which is one of the ingredients of the COOP technique described in the previous section. The formulation of COOP is naturally facilitated by AOs because of the unambiguous sense of orbital assignment to the respective atoms; there are no atom labels assigned in any PWs. The corresponding Hamiltonian element in an AO basis is given by

$$H_{\mu\nu}^R = \int d\mathbf{r} \phi_\mu(\mathbf{r}) H_{KS} \phi_\nu(\mathbf{r} - \mathbf{R}), \quad (56)$$

which is also an ingredient of another bonding indicator, i.e., COHP.

Unlike using PWs, there is no easy way to calculate the elements of the KS Hamiltonian using AOs. Because the Hamiltonian also contains the potential terms, if expanded, Eq. (56) consists not only of one- and two-center integrals, but also of three-center integrals. The latter especially has become a challenge of AO-based calculations. Fortunately, there is a method first proposed by Boys⁷⁸ to ease the calculations of multi-integrals, namely to approximate STOs by linearly combining so-called Gaussian-type orbitals (GTOs). The difference between STOs and primitive GTOs is in the radial function, for which GTOs use Gaussians:

$$R_{n\zeta}(r) \sim e^{-\zeta r^2}. \quad (57)$$

One of the advantages of GTOs lies in one of their properties, namely the product of two GTOs is also a GTO which can be integrated analytically. Hence, two- and three-center integrals of GTOs can be reduced into one-center integrals to be calculated analytically. Fig. 11 shows the radial functions of a numerically calculated 3s AO of an Na atom, its STO approximation, and a GTO.

Unlike this hydrogen-like AO and STO, the GTO does not have any cusp (discontinuous derivative) at the nucleus because GTOs are natural solutions of a quantum harmonic oscillator which is quite different with Coulomb potentials. This downside makes GTOs poorly describe an electron's behavior at the nucleus. Nevertheless, using the right number of GTOs, the behavior of valence electrons can still be captured quite accurately as depicted by Fig. 11 in which all the orbitals converge at large distance.

Furthermore, due to the symmetry behavior of local orbitals, DFT calculations on molecules can usually be solved more efficiently using a right set of local orbitals than using PWs. Even a minimal basis set, not fully complete, often appears as "complete enough" to accommodate all the charges and to minimize the total energy. However, unlike the PW basis that uses one parameter to control completeness, a local basis does not have that single parameter, another difficulty of local orbitals. Whenever problems of incompleteness or over-completeness of the basis functions occur, some caution is advisable.

Nevertheless, there are two ways to improve the accuracy of local-orbital-based calculations. The first one is by adding orbitals with the same symmetry, i.e., different exponents. This basis set is called a double- or multiple- ζ basis if it gets more than doubled. Another improvement can be done by "polarizing" the basis set, i.e., adding orbitals with higher angular momenta; these orbitals will allow further orbital mixing that in the end may lower the total energy.

Up to this point, we have discussed how to do DFT calculations with a basis set that is chosen to give the most benefit to the study of our systems. Another idea is to harvest the advantages of both kinds of basis sets through a projection method that can transform both representations of the wave functions between each other. The method, which will be described in detail in a following section, allows us to take advantages of the simplicity of the PW basis for DFT calculations and, at the same time, enables us to accurately extract chemical information, such as chemical bonding, charge, etc., from any PW-based electronic structure.

3.07.2.2 Pseudopotentials in general

The sheer existence of the periodic table assures that valence electrons alone are an excellent starting point discussing chemical bonding. Since core electrons are chemically inert and seldomly contribute to interatomic properties, quantum chemists eventually came to realize that removing these core electrons and replacing them by effective, screened potentials will save a lot of computational resources since the computational effort increases fast with the atomic number. Often these so-called pseudopotentials (PP) allow to make calculations of heavy atoms possible to begin with. The whole idea is the separation of the exact wave function into a core and a valence part and to replace the core electrons by some weaker atom-centered potential, a pseudopotential, sometimes

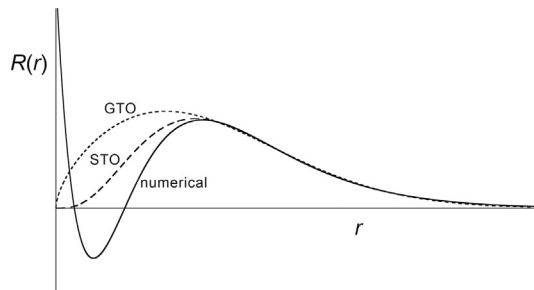


Fig. 11 Schematic plots of a numerically calculated 3s radial orbital (full line) of a Na atom, its Slater-type approximation (STO, dashed line), and a combination of three Gaussian-type functions (GTO, dotted line). Reprinted from Dronskowski, R. *Computational Chemistry of Solid State Materials: A Guide for Materials Scientists, Chemists, Physicists and Others*. Wiley-VCH: Weinheim (2005) with permission from John Wiley and Sons.

called effective-core potential (ECP), to reproduce the effects of the nucleus and the core electrons on the valence electrons. In 1935, Hellmann was the first to postulate this idea,^{79,80} thereby transferring the essence of the periodic table into quantum mechanics.

In solid-state quantum chemistry and DFT, omitting the core electrons and replacing them by pseudopotentials has this time and memory space-saving effect since the number of KS orbitals that have to be evaluated can be reduced, which also reduces the time and storage necessary for the orbital information and further operations on them like orthogonalization. An additional gain for the usage of pseudopotentials concerns the short-range and long-range behavior of a crystal wave function. The behavior in the interstitial sites could not be more different than in the region near the atom, as we have already seen when discussing plane waves. The smooth interatomic region can easily be approximated with one or only few plane waves, whereas the oscillation of the wave function near the nucleus, caused by the orthogonality to the core states, ideally requires a very large number of plane waves to describe the locality of atoms correctly. To reduce this high demand on plane waves, and therefore computational resources, the core electrons are approximated with a smoother, nodeless wave function, as explained above. With fewer oscillations in the vicinity of the atom, the cutoff energy E_{cut} for generating PWs can be reduced which requires less computational effort later.^{48,81–84}

There are a bunch of pseudopotential approaches for molecular and solid-state quantum chemistry.^{81,85–89} The two most important methods are norm-conserving⁸⁵ and (sometimes nonsingular) soft⁸⁹ PPs. In case of a norm-conserving PP, the electron density, generated by the pseudopotential wave functions and by the all-electron (AE) wave function must coincide. For a shape-consistent PP, the PP wave function and the AE must be identical to each other.⁸⁵ In case of the (ultra-) soft PP the norm constraint is relaxed to reduce the number of PW needed even more (the smaller the number of PWs the softer the PP) but with the cost of introducing a generalized KS eigenvalue formulation that has to be solved during a solid-state calculation using soft PPs.⁸⁹

A more generalized approach to PPs was introduced by Blöchl⁹⁰ within the projector augmented wave (PAW) method, which unifies the ideas behind AE and PP approaches, namely by defining a linear transformation operator \hat{T} that maps the auxiliary PW pseudo-wave function $\tilde{\Psi}$ onto the true AE wave functions Ψ_{AE}

$$\Psi_{\text{AE}} = \hat{T}\tilde{\Psi}. \quad (58)$$

Within the well-known frozen core approximation, the PAW method exhibits a pseudopotential character. Details on this method will be provided in the next sections.

To ensure the accuracy or suitability of a pseudopotential approach, the results from a calculation using PPs are compared to experimental values or an AE calculation, depending on the intention. Basic features that are analyzed for solids are the lattice parameters or the bulk modulus and, in case of molecules, the vibrational frequencies, bond distances and other geometrical details of the molecule are often inspected.^{48,84}

3.07.2.3 Projector augmented wave method

As described above, PW-based DFT calculations can be very expensive due to the large number of PWs required to capture accurately the rapidly oscillating parts of the wave functions close to the nuclei. In order to reduce the computational costs one can replace a true potential with softer pseudopotentials as explained before. However, the pseudo wave functions obtained from a pseudopotential are softer than the true wave functions, meaning their radial parts do not have the correct nodal structure, and thus close to nuclei they do not behave correctly as the true ones do.

In 1994 Blöchl proposed another alternative method called the projector augmented-wave (PAW) method to obtain the true wave functions while keeping the cost of using PWs low.⁹⁰ The method is basically the generalization (or the marriage) of the pseudopotential method and the linear augmented-plane-wave (LAPW) method.⁹¹

Before we continue, at this point it is thought necessary to briefly introduce the Dirac notation to simplify the writing of equations so that the methods can be more conveniently described. The Dirac notation makes use of the angle brackets to represent a general vector/state and its Hermitian conjugate. An arbitrary state and its Hermitian conjugate represented in a real-space are defined using the Dirac notation as the following:

$$\begin{aligned} f(\mathbf{r}) &\equiv \langle \mathbf{r} | f \rangle \\ f^*(\mathbf{r}) &\equiv \langle f | \mathbf{r} \rangle. \end{aligned} \quad (59)$$

Furthermore, a projection or an inner product of two vectors can be represented as:

$$\int d\mathbf{r} f^*(\mathbf{r}) g(\mathbf{r}) \equiv \langle f | g \rangle. \quad (60)$$

The last one also implies that

$$\int d\mathbf{r} |\mathbf{r}\rangle\langle\mathbf{r}| = 1. \quad (61)$$

Now, back to our topic. The idea behind the PAW method is to obtain the all-electron/true wave functions ψ_i , i.e., those with the correct nodal structure, through a linear transformation \mathcal{T} of the pseudo wave functions $\tilde{\psi}_i$, i.e.

$$|\psi_i\rangle = \mathcal{T}|\tilde{\psi}_i\rangle, \quad (62)$$

where $\tilde{\psi}_i$ are purely represented in terms of PWs and given by Eq. (47). Now, how do we define the transformation? Since the parts of the pseudo wave functions that need corrections are the ones close to nuclei, we can then define spheres, each with a radius r_c , surrounding the nuclei in which the transformation is only effective; outside the spheres the pseudo wave functions remain unchanged. Now inside any given sphere located at the position R , we can alternatively represent the pseudo wave functions in terms of smooth local orbitals which are called pseudo partial waves:

$$|\tilde{\psi}_i\rangle = \sum_{\mu} c_{\mu R} |\tilde{\phi}_{\mu R}\rangle, \quad (63)$$

for $|r - R| < r_c$. The corresponding true wave functions in the same sphere represented by the all-electron (AE) partial waves, ϕ , are given by

$$|\psi_i\rangle = \sum_{\mu} c_{\mu R} |\phi_{\mu R}\rangle, \quad (64)$$

The full wave functions for the whole space can then be written as

$$|\psi_i\rangle = |\tilde{\psi}_i\rangle + \sum_{\mu, R} c_{\mu R} (|\phi_{\mu R}\rangle - |\tilde{\phi}_{\mu R}\rangle). \quad (65)$$

Furthermore, because the PAW transformation is linear, the coefficients $c_{\mu R}$ can be obtained by projecting the pseudo-wave functions inside the corresponding spheres onto some local functions, \tilde{p} , which are dubbed the projector functions:

$$c_{\mu R} = \langle \tilde{p}_{\mu R} | \tilde{\psi}_i \rangle. \quad (66)$$

Since the pseudo-wave functions have to be recovered if Eq. (66) is inserted into Eq. (63), the projector functions should be biorthogonal to the pseudo partial waves, i.e.

$$\langle \tilde{p}_{\mu R'} | \tilde{\phi}_{\nu R} \rangle = \delta_{\mu\nu}. \quad (67)$$

After substituting the coefficients in Eq. (66) with Eq. (65) and comparing with Eq. (62), in the end the PAW transformation operator can be expressed as

$$\mathcal{T} = 1 + \sum_{\mu, R} (|\phi_{\mu R}\rangle - |\tilde{\phi}_{\mu R}\rangle) \langle \tilde{p}_{\mu R} |. \quad (68)$$

Furthermore, since the true wave functions have to be orthonormal, we have the following condition:

$$\langle \psi_i | \psi_j \rangle = \langle \tilde{\psi}_i | \mathcal{T}^\dagger \mathcal{T} \tilde{\psi}_j \rangle = \delta_{ij}, \quad (69)$$

where \mathcal{T}^\dagger is the Hermitian conjugate of \mathcal{T} . The AE partial waves for each chemical element are usually calculated by solving the Schrödinger equation for the isolated atoms; this method helps a quick convergence of KS wave functions. The pseudo partial waves and the projector functions, however, are not uniquely determined. Nevertheless, the pseudo partial waves are required to be identical to their AE counterparts outside the augmented sphere. They can be generated using polynomials⁹² or Bessel functions.⁹³ Lastly, the projectors are determined by implementing the orthogonalization given by Eq. (67) through a procedure described by Blöchl⁹⁰ or Vanderbilt.⁸⁹

3.07.2.4 Plane-wave-based quantum chemistry programs

Due to its simplicity and several other advantages, the PW basis has gained enormous popularity among various DFT implementations. Most of these DFT computer programs are free for academic purposes, although some are also available commercially. Instead of describing all the DFT programs available out there, we would like to mention briefly three PW-based DFT programs in connection to the implementation of the projection method that will be described in the next section; its implementation as a computer program has so far enabled processing of DFT data from these three DFT programs.

The first computer program is called the Vienna ab initio simulation package (VASP),^{93–96} which has been developed and maintained by the Kresse group of Vienna University, Austria. The program is written in Fortran and licensed as proprietary software and has very good support of pseudopotentials. It also offers various exchange-correlation functionals. Furthermore, the computational efficiency is achieved mainly through a parallel computing method called message passing interface (MPI), although the hybrid with another method called open multi-processing (openMP) has also been implemented.⁹⁷ Several attempts have also been made to speed up VASP further using graphical processing units (GPUs).^{98–100} VASP uses a universal naming system for its input and output files.

The next program is ABINIT which is developed by Gonze's group at the Catholic University of Louvain-la-Neuve, Belgium, and distributed under the GNU general public license (GPL) or open-source.^{101–104} ABINIT is also written in Fortran and parallelized

using MPI and openMP.^{105,106} The GPU implementation has also been experimented.¹⁰¹ ABINIT supports various kinds of exchange-correlations functionals and pseudopotentials/atomic datasets. The generation of PAW atomic datasets, furthermore, is collected in a library dubbed JTH atomic dataset¹⁰⁷ and is formatted using the extensible markup language (XML), which is a very efficient format to allow an easy extraction of the PAW atomic data.

The third DFT program is called Quantum ESPRESSO, which is also open-source.^{108–110} Its development is an open initiative through internationally collaborative work coordinated by the Quantum ESPRESSO foundation. The program used to be a stand-alone program called PWscf before the integration with other quantum programs by the same initiative. It is written mainly in Fortran, although C is also used to write some other parts, and like other two programs, it takes advantages of parallel computing through MPI and openMP. The GPU implementation using NVIDIA machines is currently available only in the ground state subprogram, i.e., pw.x.¹¹⁰ Various exchange correlation functionals and pseudopotentials are also supported by the program. Ready-to-use pseudopotentials are available on its website, but many other groups also share their own built-in pseudopotentials publicly.^{111–115} Furthermore, the pseudopotentials for Quantum ESPRESSO follow a format called unified pseudopotential format (UPF) which is very similar to XML, and currently the developer is transforming UPF to the true XML format to improve its I/O efficiency.

3.07.2.5 Projection method

Although the PW basis is preferred in many DFT calculations due to its simplicity, many other essential analyses on electronic structure, such as population⁵⁸ and chemical bonding^{26,51,74,75,116} analyses, require local-orbital descriptions of the electronic structure. Local orbitals can also be used as a basis to more compactly represent a tight-binding Hamiltonian for further advanced analyses or calculations.^{117,118} In order to facilitate this purpose, a projection method to transform the basis of the Kohn-Sham (KS) wave functions from the PW basis into a local orbital basis is required. Furthermore, due to their nature, only a small number of local orbitals, i.e., a minimal basis set, are usually utilized to represent KS wave functions.

An early projection method was proposed by Sánchez-Portal et al. to reconstruct the PW-based DFT wave functions using various local-orbital bases.^{119,120} The main idea of this method is to project the PW-based KS wave functions onto each orbital in a given set of local orbitals to the get so-called transfer matrix

$$\begin{aligned} T_{jk} &= \left\langle \chi_{\mu k} | \tilde{\psi}_{jk} \right\rangle \\ &= \frac{1}{\sqrt{\Omega}} \sum_G C_{j(k+G)}^{\text{PW}} \int d\mathbf{r} \chi_{jk}^*(\mathbf{r}) e^{i(\mathbf{k}+\mathbf{G}) \cdot \mathbf{r}} \end{aligned} \quad (70)$$

that basically describes the contribution of a local orbital $\chi_{\mu k}$ in the given PW-based wave function. Here, $\chi_{\mu k}$ is the reciprocal representation of a local orbital obtained through the Fourier transform:

$$|\chi_{\mu k}\rangle = \frac{1}{\sqrt{N_R}} \sum_R e^{i\mathbf{k} \cdot \mathbf{R}} |\chi_{\mu R}\rangle. \quad (71)$$

Furthermore, we can also expand the KS wave functions in terms of local orbitals using Eq. (54) to obtain another transfer-matrix representation

$$T_{jk} = \sum_v \langle \chi_{\mu k} | \chi_{vk} \rangle C_{vk}^{\text{LCAO}} = \sum_v S_{\mu v; k} C_{vk}^{\text{LCAO}}, \quad (72)$$

where $S_{\mu v; k}$ describes the overlap between two orbitals in the reciprocal space. The last equation forms a linear algebraic expression which can be solved, for instance with a matrix inversion method, to yield the LCAO coefficients. Furthermore, the orthonormality of the reconstructed KS wave functions can be quantified as

$$\hat{O}_{jk} = \left\langle \tilde{\psi}_{jk} | \tilde{\psi}_{jk} \right\rangle = \sum_{\mu v} C_{\mu jk}^{\text{LCAO}} S_{\mu v; k} C_{vjk}^{\text{LCAO}}. \quad (73)$$

Ideally, \hat{O}_{jk} should be one, but the reconstructed wave functions may deviate from the original ones. Therefore, in order to measure the average deviation, Sánchez-Portal et al. proposed a quantity called the spilling parameter,^{119,120}

$$\Omega \equiv \frac{1}{N_j N_k} \sum_{jk} f_{jk} (1 - \hat{O}_{jk}), \quad (74)$$

where N_j and N_k , respectively, are the number of bands and k -points, and f_{jk} is the occupation function. The spilling parameter basically checks the quality of a projection calculation with a given local basis set. Furthermore, since $f_{jk} = 0$ for all conduction bands, the parameter only considers the valence bands, that is, the occupied levels.

The projection method described above suits well any PW-based calculations. However, it needs a modification if one wants to use it for the more accurate PAW method. Clearly, the PAW method operates by a PW basis, but the pseudo wave functions in this method are allowed to be very soft, and thus less precise, such that they only capture correctly the interstitial parts, while other auxiliary local functions are added up through augmentation to obtain the corresponding true wave functions:

$$\left| \psi_{jk} \right\rangle = \left| \tilde{\psi}_{jk} \right\rangle + \sum_{\mu,R} \left(\left| \phi_{\mu R} \right\rangle - \left| \tilde{\phi}_{\mu R} \right\rangle \right) \left\langle \tilde{p}_{\mu R} \right| \tilde{\psi}_{jk} \rangle. \quad (75)$$

Consequently, the projection of any PAW wave function onto a local orbital, i.e., the transfer matrix, will yield two terms, namely the pseudo and augmented transfer matrices:

$$T_{juk} = \left\langle \chi_{\mu k} \right| \psi_{jk} \rangle = T_{juk}^{\text{PS}} + T_{juk}^{\text{aug}}. \quad (76)$$

Here, the pseudo and augmented transfer matrices are, respectively, given by

$$T_{juk}^{\text{PS}} = \left\langle \chi_{\mu k} \right| \tilde{\psi}_{jk} \rangle \quad (77)$$

and

$$T_{juk}^{\text{aug}} = \sum_{\nu,R} \left\langle \chi_{\mu k} \right| \bar{\phi}_{\nu R} \rangle \left\langle \tilde{p}_{\nu R} \right| \tilde{\psi}_{jk} \rangle, \quad (78)$$

where $\left| \bar{\phi}_{\nu R} \right\rangle = \left| \phi_{\nu R} \right\rangle - \left| \tilde{\phi}_{\nu R} \right\rangle$. The pseudo transfer matrix is exactly the same as the one from the PW-based projection, i.e., Eq. (70), whereas the augmented one involves two scalar products. The first scalar product comes from the projection of the difference between the AE and pseudo partial waves onto a local basis function, whereas the second one is the projection of the pseudo wave functions onto projector functions; the latter is also often called the wave function characters. The first scalar product can be simplified by using the fact that the AE and pseudo partial waves are identical outside the augmented spheres. Consequently, the product will only involve integrations carried out inside individual augmented spheres, independent of unit cell positions, and constrained by their corresponding radius r_c :

$$\left\langle \chi_{\mu k} \right| \bar{\phi}_{\nu R} \rangle = \frac{1}{\sqrt{N_R}} \sum_{R'} e^{-ik \cdot R'} \left\langle \chi_{\mu R'} \right| \bar{\phi}_{\nu R} \rangle = \frac{1}{\sqrt{N_R}} \sum_{R'} e^{-ik \cdot R'} \delta_{RR'} \left\langle \chi_{\mu} \right| \bar{\phi}_{\nu} \rangle = \frac{1}{\sqrt{N_R}} e^{-ik \cdot R} \left\langle \chi_{\mu} \right| \bar{\phi}_{\nu} \rangle, \quad (79)$$

where

$$\left\langle \chi_{\mu} \right| \bar{\phi}_{\nu} \rangle = \int_0^{r_c} dr \chi_{\mu}^*(r) \bar{\phi}_{\nu}(r). \quad (80)$$

By inserting (79) into (78), we then get

$$T_{juk}^{\text{aug}} = \sum_{\nu} \left\langle \chi_{\mu} \right| \bar{\phi}_{\nu} \rangle \frac{1}{\sqrt{N_R}} \sum_{R} e^{-ik \cdot R} \left\langle \tilde{p}_{\nu R} \right| \tilde{\psi}_{jk} \rangle, \quad (81)$$

which can be further simplified by realizing that the sum of projector functions over the translation vectors is just their Fourier transform:

$$T_{juk}^{\text{aug}} = \sum_{\nu} \left\langle \chi_{\mu} \right| \bar{\phi}_{\nu} \rangle \left\langle \tilde{p}_{\nu k} \right| \tilde{\psi}_{jk} \rangle, \quad (82)$$

Furthermore, since the second scalar product has the same form as the pseudo transfer matrix, its expression in terms of PW coefficients has the same form as Eq. (70), in which we substitute χ with \tilde{p} . Once these two transfer matrices are determined, we can then sum them to get the total transfer matrix and use Eq. (72) to calculate the LCAO coefficient matrix. The projection quality can also be checked again by calculating the spilling parameter defined by Eq. (74). We can also reconstruct the elements of the KS Hamiltonian using our local basis functions,

$$H_{\mu\nu} = \left\langle \chi_{\mu} \right| \left[\sum_j \left| \psi_{jk} \right\rangle \varepsilon_{jk} \left\langle \psi_{jk} \right| \right] \left| \chi_{\nu} \right\rangle = \sum_j T_{juk}^* \varepsilon_{jk} T_{juk}, \quad (83)$$

for COHP calculations.

The aforementioned PAW-based projection method has been realized in a computer program called Local Orbital Basis Suite Towards Electronic-Structure Reconstruction, or LOBSTER for short.^{121,122} The program post-processes PAW-based DFT data by projecting the wave functions onto local orbitals/basis functions to reconstruct the same wave functions in terms of LCAO, and thus to enable chemical bonding and population analyses. Fig. 12 shows the diagrammatic description of the data flow in LOBSTER. The process starts with the data from a PAW-based DFT calculation; there are three DFT programs so far whose data LOBSTER can handle, namely, VASP,^{93–96} ABINIT,^{101–104} and Quantum ESPRESSO (QE).^{108–110} A respective interface routine of LOBSTER then loads the data into the computer memory. After cleaning them up, the data are then transferred to the projection routine. Additionally, basis functions from one of the three built-in basis sets are prepared and then also transferred to the projection routine; their setup can be controlled through an input file called lobsterin using several keywords, which can be found in the manual. Further description of LOBSTER's basis sets is given in the next section.

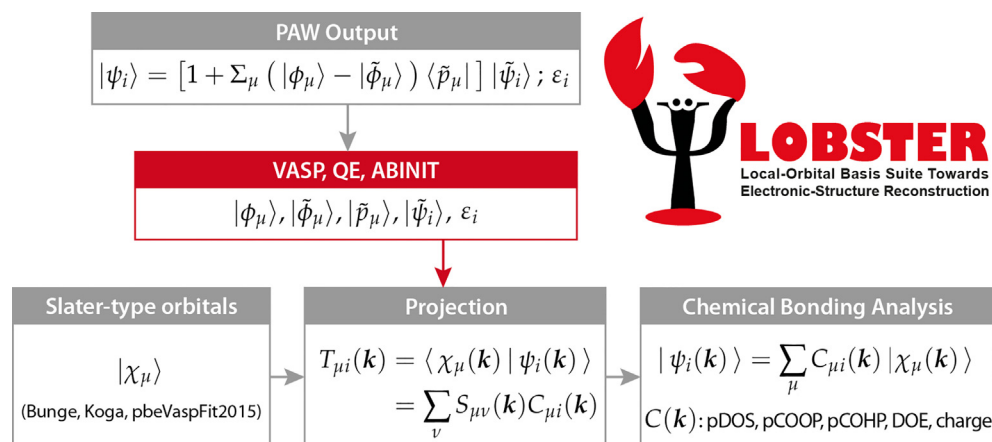


Fig. 12 Sketch of LOBSTER's flowchart. The process starts from a system of interest with its Kohn-Sham wave functions ψ_i and the corresponding eigenvalues ϵ_i calculated self-consistently by a DFT program using the projector-augmented wave (PAW) method. The wave functions and all related data are then acquired and loaded into the computer memory through I/O interfaces (red block) specifically designed to three DFT programs (VASP, ABINIT, and QE). A separate routine prepares a set of local basis functions χ_{μ} that are selected semi-automatically from a built-in database. Wave functions and basis functions are then brought into the projection routine to determine the overlap matrix $S_{\mu\nu}$ and the transfer matrix $T_{\mu i}$ between the delocalized and localized representations. From those, the projected coefficient and Hamiltonian matrices $C_{\mu i}$ and $H_{\mu\nu}$, respectively, are accessible and enable various bond-analytic tools. The LOBSTER logo is copyrighted by the Chair of Solid-State and Quantum Chemistry at RWTH Aachen University. Reprinted from Nelson, R.; Ertural, C.; George, J.; Deringer, V. L.; Hautier, G.; Druskowski, R. LOBSTER: Local Orbital Projections, Atomic Charges, and Chemical-Bonding Analysis From Projector-Augmented-Wave-Based Density-Functional Theory. *J. Comput. Chem.* **2020**, *41* (21), 1931–1940 with permission from John Wiley and Sons.

Once the data of wave functions and basis functions are available in the memory, the calculations of the transfer, overlap, and LCAO coefficient matrices are performed, respectively. Finally, the resulted LCAO coefficients are used to calculate the reconstructed electronic structure, chemical bonding indicators, and population quantities. These results will be described in detail in the next sections.

LOBSTER is written in object-oriented C++ and uses two external libraries (in addition to the standard C++ library), namely Boost¹²³ to handle various algorithms and memory management and Eigen¹²⁴ to efficiently deal with linear algebra, i.e., matrices, vectors, and related operations. To improve further the efficiency through parallelization, openMP has also been implemented in LOBSTER. The program can be downloaded free of charge for academic purposes at www.cohp.de.

3.07.2.6 Atomic basis sets in LOBSTER

There are many ways to build local basis functions for the projection methods. For instance, Sánchez-Portal et al.^{119,120} used two groups of local bases; the first one was obtained from numerical atomic calculations, whereas the second one was a group of Slater-type orbitals (STOs) built by linearly combining Gaussian-type orbitals (GTOs).

LOBSTER, however, provides three atomic basis sets. The first one goes back to Bunge et al., published in 1993,¹²⁵ hence for brevity it will be called the Bunge basis set. It supports atomic orbitals for atoms from He ($Z = 2$) up to Xe ($Z = 54$), and all the atomic orbitals were obtained by solving the Roothaan-Hartree-Fock (RHF) equations for atomic cases with energy error less than 0.6 meV.¹²⁵ In more detail, a finite number of STOs were employed as a more primitive basis and linearly combined to build the radial part of the atomic eigenfunctions/orbitals

$$\phi_{nl} = \sum_j c_{nlj} R_j. \quad (84)$$

Here, c_{nlj} are the linear combination coefficients obtained from solving the RHF equations, whereas the radial part of STOs, R_j is given by Eq. (53). Note that the index j here covers both n and ζ in Eq. (53). Furthermore, although STOs themselves do not have nodal structures, the resulted atomic orbitals do have a correct nodal structure through the linear combination.

The second basis set available in LOBSTER was produced by Koga et al. using the same HF method,^{126,127} and for shortness, we call it the Koga basis set. It provides atomic orbitals for elements up to Lr ($Z = 103$). Furthermore, compared to the Bunge basis set, the Koga basis set uses more STOs to build the atomic orbitals, and thus gives more accurate atomic energy with the average error less than 0.05 meV for $Z \leq 54$,¹²⁶ and not more than 5 meV for $55 \leq Z \leq 103$.¹²⁷ Moreover, the calculated atomic orbitals in this basis were constrained to optimally meet the nuclear-electron cusp condition^{128–130} and the asymptotic long-range behavior.^{131–134}

Although the previous two basis sets are already sufficient for most projection cases, some systems require unoccupied atomic orbitals for certain elements in order to correctly reconstruct the PAW wave functions. An example of this situation will be the high-temperature, body-centered cubic beryllium (β -Be).¹³⁵ A PAW-based DFT calculation was done for this system with ABINIT^{101–104}

using the GGA-PBE exchange-correlation functional¹³⁶ from the JTH table. Afterward, a projection calculation with LOBSTER^{121,122} proceeded with the reconstruction of the PAW electronic structure using local orbitals from the Bunge basis set.¹²⁵ The atomic configuration of Be, i.e., $1s^2 2s^2$, implies the sufficient use of the atomic orbitals 1s and 2s for the reconstruction. However, this set of orbitals turns out to be insufficient for the projection; 19% of the original charge was spilled through the projection. This high charge spilling can be significantly reduced by polarizing the basis, i.e., adding another (unoccupied) atomic orbital with a higher angular momentum, in this case 2p. This very 2p orbital was generated as part of the third and new basis set¹²² in LOBSTER. This new basis set takes the occupied orbitals as those of the Koga basis set. Additional (unoccupied) orbitals were then generated by fitting their radial part given by Eq. (84) to the radial part of the corresponding PAW wave function obtained by VASP using the PBE functional. The fitting then yielded the exponents and the linear combination coefficients for all STOs. The new basis set is named pbeVaspFit2015 after the generating method.

For β -Be, adding the new 2p orbital into the projection calculation lowers the charge spilling significantly to 1.73%, and thus the reconstructed wave function are considerably improved. Since the square of a wave functions results in the corresponding charge density, simple plotting allows the visualization of the difference of the electron densities obtained from the PAW and the projection calculations. Fig. 13 shows the isosurface plots of the density difference before (left) and after (right) adding the 2p orbital for the fourth band at the Γ point. Moreover, the plots are fixed at 65% of the maximum density difference.

As can be seen, the spilled charge is significantly reduced after the 2p orbital was included in the projection basis. This also confirms that in the solid state formerly unoccupied atomic orbitals may get involved in the bonding process, the well-known band broadening which makes Be metallic, and hence the formation of the valence bands. Another interesting thing worth noting here is that, although the atomic orbitals of the pbeVaspFit2015 basis set are based on the PAW wave functions of VASP, the orbitals are still very reliable for the construction of electronic structure calculated with the other DFT programs accommodated by LOBSTER, i.e., ABINIT and Quantum ESPRESSO.

3.07.2.7 The projected DOS, COOP, COHP, fatband, and k -dependent COHP and time-reversal symmetry

Using the LCAO coefficients $c_{\mu jk}$ obtained from the projection method, various quantities are directly accessible. The partial density of states (PDOS) is defined as

$$\text{PDOS}_\mu(E) = \sum_{\nu j k} c_{\mu j k}^* S_{\mu \nu}^k c_{\nu j k} \delta(\varepsilon_{j k} - E), \quad (85)$$

where $S_{\mu \nu}^k$ is the overlap between orbitals μ and ν in reciprocal space such that the sum of PDOS over all orbitals μ yields the total density of states (TDOS). To compare this DOS formula with the one based on the original PAW method, the TDOS and PDOS of diamond calculated with both methods are shown in Fig. 14A as taken from LOBSTER's publication.¹²¹ The PAW-based PDOS were calculated by projecting the wave functions onto PAW spheres, and hence ignoring the interstitial parts. On the other hand, the LOBSTER projection (new method) considers all spaces. The PAW-based TDOS and PDOS were calculated using VASP,^{93–96} whereas the projection-based ones using LOBSTER.^{121,122} As we can see the TDOS from both methods are virtually the same and agree with each other that the system is an insulator.

The PDOS, however, differ significantly. The PDOS from the PAW method (Fig. 14A (middle, colored shades)) are smaller than the ones from the projection method (Fig. 14A (right, colored shades)). By integrating each PDOS up to the Fermi level to yield the numbers of electrons occupying each orbital and then adding them, we can check the total electrons considered by each method; here the original number of electrons is 8 (four electrons per atom, two C atoms). For the PAW-based PDOS, we only get 5.11 electrons, whereas 7.99993 electrons are obtained using the projection-based formula. Therefore, compared to the PAW method, the projection method does not lose almost three electrons and allows for a more accurate distribution of electronic states.

Furthermore, the crystal orbital overlap population (COOP) can be calculated by taking the overlap of a pair of atoms (orbitals) in real space and weighted with the sum of the products of the corresponding LCAO coefficients.

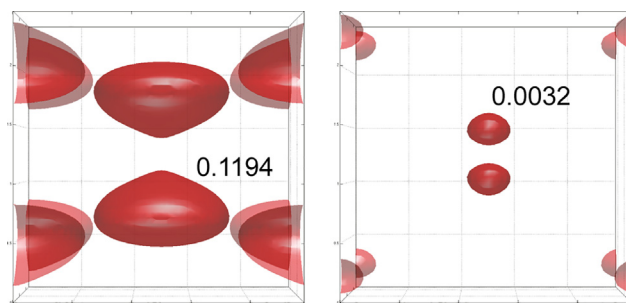


Fig. 13 Isosurface plots (\AA^{-3}) at 65% of the maximum difference between the electron densities from the PAW and projection calculations for the fourth band of β -Be at Γ . The left side only uses 1s and 2s of the Bunge basis set, whereas the right side has included the new 2p orbital from the fitting procedure described in the text. Reprinted from Maintz, S.; Deringer, V. L.; Tchougréeff, A. L.; Dronskowski, R., LOBSTER: A Tool to Extract Chemical Bonding From Plane-Wave Based DFT. *J. Comput. Chem.* **2016**, 37 (11), 1030–1035 with permission from John Wiley and Sons.

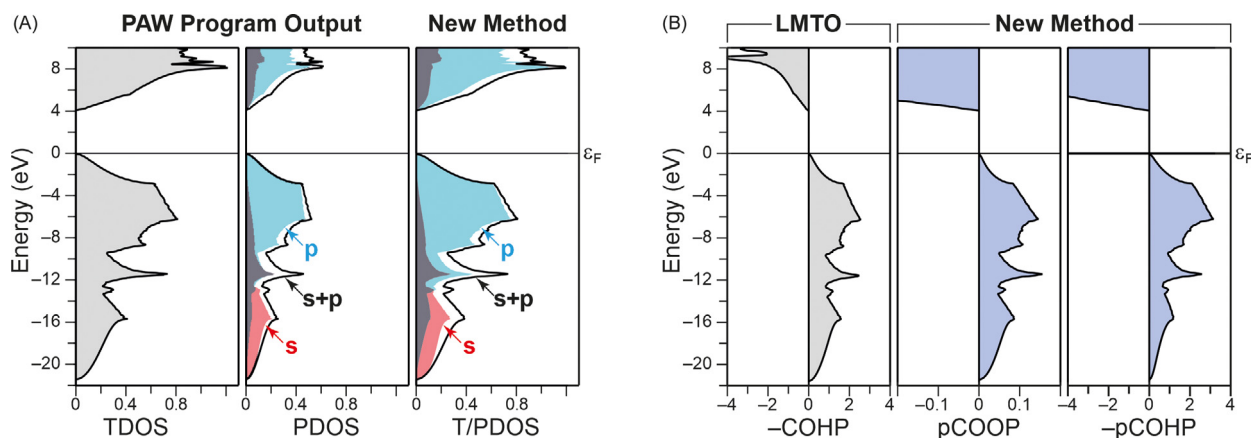


Fig. 14 (A) Left: Total DOS for diamond computed using the PAW method in VASP. Middle: partial DOS using the PAW-based method of VASP. Carbon s and p contributions are indicated by red and cyan shading, respectively. The sum of both is given by a solid line. Right: As before but, this time, obtained from the analytical projection method we describe here. (B) Chemical-bonding analysis for the C–C bond in diamond. Left: Traditional COHP analysis performed by the TB-LMTO-ASA approach. Right: pCOOP and Hamilton populations (pCOHP), obtained with the projection method. As is convention, all plots show bonding (stabilizing) contributions to the right of the vertical line, and antibonding (destabilizing) contributions to the left. In all plots, the energy zero is chosen to coincide with the Fermi level ϵ_F . Reprinted from Maintz, S.; Deringer, V. L.; Tchougréeff, A. L.; Dronskowski, R. Analytic Projection From Plane-Wave and PAW Wavefunctions and Application to Chemical-Bonding Analysis in Solids. *J. Comput. Chem.* **2013**, *34* (29), 2557–2567 with permission from John Wiley and Sons.

$$\text{COOP}_{\mu T; \nu T'}(E) = S_{\mu T; \nu T'} \sum_{jk} f_{jk} c_{\mu T; jk}^* c_{\nu T'; jk} \delta(\epsilon_{jk} - E). \quad (86)$$

where f_{jk} is the occupation number of the state $\{j, k\}$ or often just called the weight and

$$c_{\mu T; jk} = c_{\mu jk} e^{ik \cdot T} \quad (87)$$

to simplify the writing. The analogous crystal orbital Hamilton population (COHP) is calculated in a similar manner by using the Hamiltonian in real space:

$$\text{COHP}_{\mu T; \nu T'}(E) = H_{\mu T; \nu T'} \sum_{jk} f_{jk} c_{\mu T; jk}^* c_{\nu T'; jk} \delta(\epsilon_{jk} - E). \quad (88)$$

Here, $S_{\mu T; \nu T'}(H_{\mu T; \nu T'})$ is basically the Fourier transform of $S_{\mu\nu}^k(H_{\mu\nu})$. Keep in mind that positive values of COOP (COHP) describe bonding (antibonding) interactions and vice versa. Since all the ingredients in the formulas above are obtained through the projection method, they are also called “projected COOP” (pCOOP) and “projected COHP” (pCOHP). Using diamond again as an example, we show in Fig. 14B the negative COHP of the C–C bond (left) calculated with the traditional method of the Tight-Binding Linear Muffin-Tin Orbital Atomic-Sphere Approximation (TB-LMTO-ASA for which COHP was originally developed),^{91,137} as well as the pCOOP (middle) and negative pCOHP (right) calculated using the equations above. All three qualitatively agree with each other in that the whole valence bands are dominated by bonding interactions. Furthermore, since the conduction bands are antibonding throughout, any additional electron density would shift the Fermi level to the conduction bands, and thus destabilize the system. We will demonstrate further how the projection-based chemical bonding analysis has been used to benefit material studies.

The COOP/COHP formulas given above require a summation over all k -points in the first Brillouin zone (BZ). These calculations of COOP/COHP will become computationally more and more costly as the number of k -points increases. The computational cost, fortunately, can be reduced by a parallel technique such as openMP, which has been implemented since LOBSTER 1.1.¹²² In addition, one can also exploit symmetry to connect the wave functions of different k -points as to explicitly consider fewer number of k -points in the summation. One kind of symmetry that always exists in systems isolated from external fields, such as a magnetic field, is the time reversal (TR) symmetry. It describes the invariance of the aforementioned systems when the time is hypothetically reversed by the time-reversal operator t . The invariance of the systems can be shown mathematically using a so-called commutation relation between t and the Hamiltonian H :

$$[t, H] = tH - Ht = 0. \quad (89)$$

For proof, please refer to any advanced textbooks of symmetry, such as Ref. 138. This commutation relation implies that Bloch states of the momenta k and $-k$ share the same eigenenergy, i.e., $\epsilon_{jk} = \epsilon_{j(-k)}$.

Furthermore, an operation of t on a given Bloch wave function will transform the wave function into its complex conjugate. However, by inserting the complex conjugate into the KS equation, it can also be shown that the wave function's complex conjugate is actually just another wave function with the opposite momentum. Therefore, we get the following relationship:

$$t\psi_{jk}(\mathbf{r}) = \psi_{jk}^* = \psi_{j(-k)}(\mathbf{r}). \quad (90)$$

Since the COOP and COHP formulas only differ in the use of overlap and Hamiltonian, we will only derive the simplified formula of COOP; the same exact steps can be redone for COHP. The first step of the simplification is to split the summation of Eq. (86) into two groups, in which one group is the inversion of the other. Afterward, we realize that each \mathbf{k} -point and its inversion are energetically equal:

$$\text{COOP}_{\mu T; \nu T'}(E) = S_{\mu T; \nu T'} \sum_j \left[\sum_{\substack{\mathbf{k} \in (\text{BZ}) \\ k \in \left(\frac{\text{BZ}}{2}\right)}} f_{jk} c_{\mu T; jk}^* c_{\nu T'; jk} + \sum_{\mathbf{k}' = -\mathbf{k}} f_{jk'} c_{\mu T; jk'}^* c_{\nu T'; jk'} \right] \delta(\varepsilon_{jk} - E). \quad (91)$$

Next, we recall from Eq. (54) how the wave functions are represented in terms of AOs. Using cubic harmonics, instead of spherical harmonics, AOs can be made real functions, and thus unaffected by the operator t . Then if we insert Eq. (90) into Eq. (54), it can be shown that the time-reversal of the wave functions consequently yields

$$c_{\mu T; jk}^* = c_{\mu T; j(-k)}. \quad (92)$$

After putting Eq. (92) into Eq. (91), for every \mathbf{k} -point we will find a term that adds with its complex conjugate; this addition just equals twice the real part of the same term. In the end, we arrive at

$$\text{COOP}_{\mu T; \nu T'}(E) = S_{\mu T; \nu T'} \sum_{\substack{\mathbf{k} \in (\text{BZ}) \\ k \in \left(\frac{\text{BZ}}{2}\right)}} \tilde{f}_{jk} \Re \left\{ c_{\mu T; jk}^* c_{\nu T'; jk} \right\} \delta(\varepsilon_{jk} - E), \quad (93)$$

where $\tilde{f}_{jk} = 2f_{jk}$, and $\Re\{z\}$ means the real part of the complex value z . The summation over \mathbf{k} -points now only considers half of the BZ. Correspondingly, by substituting S with H , the COHP due to the TR symmetry becomes

$$\text{COHP}_{\mu T; \nu T'}(E) = H_{\mu T; \nu T'} \sum_{\substack{\mathbf{k} \in (\text{BZ}) \\ k \in \left(\frac{\text{BZ}}{2}\right)}} \tilde{f}_{jk} \Re \left\{ c_{\mu T; jk}^* c_{\nu T'; jk} \right\} \delta(\varepsilon_{jk} - E). \quad (94)$$

These last two formulas have been implemented in LOBSTER 4.0⁶³ to make the calculations of the projection and post-projection twice more efficient. The efficiency applies not only to the calculation time but also to data storage. Moreover, since LOBSTER can now take only half of the BZ, the DFT data for the projection can now also be obtained twice more efficient.

Now, back to chemistry! While COHP is useful in describing chemical bonding in energy space, the chemical bonding in real and reciprocal space is often direction-dependent, meaning bonding at some \mathbf{k} -points may be of special interest or at least more significant than bonding at any other \mathbf{k} -points; knowing this information can be crucial in studying a given material. Therefore, we define, based on the original definition of COHP, a new quantity called the \mathbf{k} -dependent COHP that resolves COHP into individual contributions from each \mathbf{k} -point and band:

$$\text{COHP}_{\mu \nu; jk} = c_{\mu; jk}^* H_{\mu \nu; k} c_{\nu; jk}. \quad (95)$$

Additionally, we can also define a band character, or often called a fatband, to describe the character amount of an orbital on a given band:

$$\text{FATBAND}_{\mu; jk} = \sum_{\nu} C_{\mu; jk}^* S_{\mu \nu; k} C_{\nu; jk}. \quad (96)$$

To see the last two features in action let us now consider thallium fluoride (TlF). The compound has an orthorhombic (*Pbcm*) crystal structure with 8 atoms per unit cell (Fig. 15A). However, the orthorhombic structure of TlF is somewhat unusual because electrostatic repulsions among ions would make higher symmetric structures, such as rock-salt or CsCl structures, more favorable for TlF, just like in the TlCl case. More interestingly, a study by Häussermann et al. showed that a high pressure up to 40 GPa applied on TlF also did not trigger any structural change to a higher symmetric structure.¹³⁹

To shed light on this puzzle, in addition to the electrostatic interactions, we need to consider orbital-orbital interactions that can be properly analyzed by means of chemical bonding analysis of individual bands, i.e., \mathbf{k} -dependent COHP. In order to do that, the required DFT data were obtained using VASP within the PAW framework. Furthermore, to ensure the convergence a mesh of 763 \mathbf{k} -points and a cutoff energy of 520 eV were set up. The resulting PAW wavefunctions were then projected by LOBSTER to obtain the LCAO coefficients for calculating FATBAND and \mathbf{k} -dependent COHP.

Let us first have a look at the FATBAND of the orbitals Tl 6s and 6p on individual bands plotted, respectively, on the left and right sides of Fig. 15B. From the left plot we can see clearly that the s electrons of Tl reside in two groups of relatively dispersed valence bands, i.e., around -2 and -4 eV, in between is another group of valence bands basically formed by F 2p (not shown). From here we can infer that the electrons of Tl 6s are not as inert as it is commonly assumed. Furthermore, the right plot clearly indicates that Tl

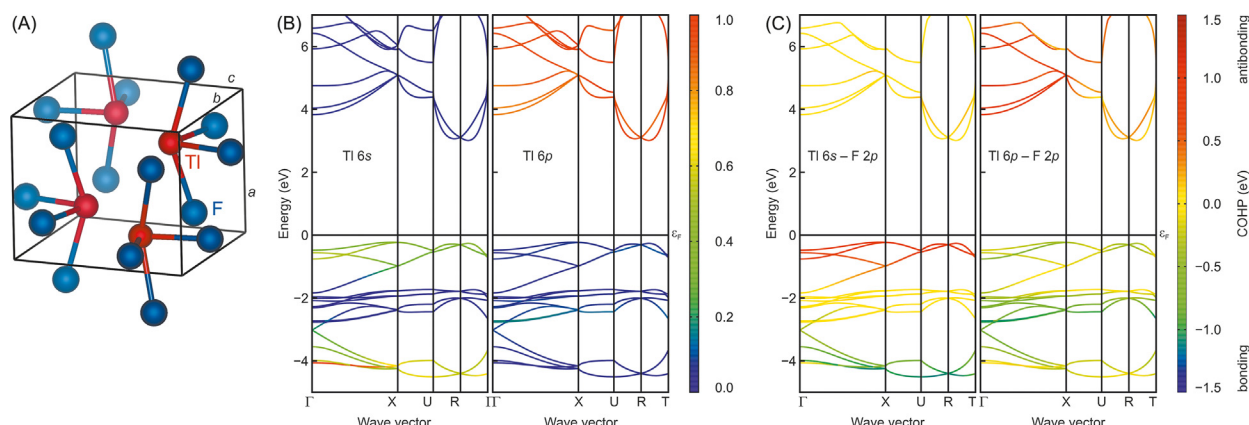


Fig. 15 (A) The crystal structure of Thallium fluoride (TlF). Contributions to TlF electronic structure from (B) fatbands of Tl 6s (left) and Tl 6p (right) as well as (C) \mathbf{k} -dependent Tl–F COHP of 6s–2p (left) and 6p–2p (right). Reprinted from Nelson, R.; Ertural, C.; George, J.; Deringer, V. L.; Hautier, G.; Dronskowski, R., LOBSTER: Local Orbital Projections, Atomic Charges, and Chemical-Bonding Analysis From Projector-Augmented-Wave-Based Density-Functional Theory. *J. Comput. Chem.* **2020**, 41 (21), 1931–1940 with permission from John Wiley and Sons.

6p mostly contributes to the conduction bands. However, its little contribution can also be seen on some of the valence bands especially around -3 eV, although the interactions involving Tl 6p on those bands are not explicitly resolved.

To explicitly resolve orbital-orbital interactions on individual bands we turn to \mathbf{k} -dependent COHP. Fig. 15C shows the \mathbf{k} -dependent COHP of Tl 6s–F 2p (left) and Tl 6p–F 2p (right) interactions. Negative (positive) values as usual describe bonding (antibonding) interactions. A broad view of these plots shows us that some narrow energy windows comprise a wide range of interactions such that nonbonding interactions will be superimposed by bonding/antibonding interactions and will not be noticeable in regular COHP. From the left plot we can see clearly that the valence bands around -2 and -4 eV, respectively, result from the bonding and antibonding interactions between Tl 6s and F 2p orbitals. This emphasizes the previous observation from the FATBAND that the inert pair of Tl 6s is not so inert after all. It is also obvious from the plot that the bonding and antibonding interactions are comparable in strength, and therefore cannot take a role in stabilizing the system. If these were the only interactions to consider, then the electrostatic interactions would dictate TlF to adopt a more symmetric structure. Surprisingly, as shown by the right plot, there exist bonding interactions between Tl 6p and F 2p orbitals spreading through the valence bands. These interactions counter the electrostatic interactions and are only possible because the less symmetric orthorhombic structure adopted by TlF allows for overlaps between Tl 6p and F 2p orbitals. However, this is not the only reason for the existence of Tl 6p–F 2p interactions; they are possible also because Tl 6p and F 2p are relatively closer in energy. This is not the case in TlCl where the energy difference between Tl 6p and Cl 3p is larger and does not allow for cation p-anion p mixing. Therefore, only electrostatic interactions govern and TlCl adopts the high-symmetry CsCl structure. As a last remark we can also see clearly that if conduction bands are occupied, Tl 6p–F 2p antibonding interactions will be activated and their strength will depend strongly on the direction in reciprocal space, with most destabilizing at Γ but rather weak in other directions.

The \mathbf{k} -dependent COHP feature is now available in LOBSTER 4.0⁶³ and has been employed in several studies. The feature was firstly employed as part of the machinery in a study to identify a novel strategy to enhance the thermoelectric material n-type Mg₃Sb₂.¹⁴⁰ More specifically, the \mathbf{k} -dependent COHP clearly shows that the conduction-band minimum (CBM) is dominated by covalent interactions. This finding, furthermore, along with the band structure and Fermi surface analyses, culminated in a new proposal to use partial substitution of Mg with more ionic cations to significantly improve the thermoelectric property; a more detailed description will be given in a following section. A high-throughput computational screening also utilized \mathbf{k} -dependent COHP to help recognizing more efficiently a high Curie-temperature ferromagnetic semiconductor In₂Mn₂O₇.¹⁴¹ The \mathbf{k} -dependent COHP also played a similar role in another high-throughput screening project to help forecasting new diamond-like ABX₂ materials with excellent and promising thermoelectric properties.¹⁴² The most recent application of the feature is to rationalize the trend in experimental band gaps of the Bi₂MO₄Cl (M = Y, La, Bi) photocatalysts.¹⁴³ In this study, the dominant interactions on the CBM revealed by the \mathbf{k} -dependent COHP provide support for a molecular orbital model explaining the cause of the CBM (i.e., band gap) shift in Bi₂MO₄Cl. The model also hints at controllable conduction bands of Bi₂MO₄Cl to find derived exceptional photocatalysts.

3.07.2.8 Mulliken and Löwdin population analysis

When the square-integrable crystal wave function $\psi_j(\mathbf{k})$ is constructed as a linear combination of atomic orbitals $\chi_\mu(\mathbf{k})$ with the normalized, non-orthogonal basis set χ in the LCAO-CO approximation^{45,64} like

$$\left| \psi_j(\mathbf{k}) \right\rangle = \sum_{\mu} c_{\mu j}(\mathbf{k}) \left| \chi_{\mu}(\mathbf{k}) \right\rangle, \quad (97)$$

the LCAO-CO coefficient $c_{\mu j}(\mathbf{k})$ in reciprocal space can be used to compute the density matrix elements $P_{\mu\nu}(\mathbf{k})$, which are essential for the population analyses. As already mentioned above, both Mulliken and Löwdin charges q_A are calculated from the so-called gross population (GP), (Eq. 36), numerical quantities to determine the number of electrons, e.g., in an orbital or atom. In particular, GP_μ is the gross orbital population including all orbitals μ belonging to atom A. Its calculation goes as follows: the electron density distribution in a molecule or solid is divided into a *net population* (NP) and an *overlap population* (OP) by using the normalization condition of a square-integrable wave function

$$\begin{aligned}\int \psi_j^*(\mathbf{k})\psi_j(\mathbf{k}) d\tau &= 1 = \sum_{\mu} c_{\mu j}^2(\mathbf{k}) \int \chi_{\mu}^2(\mathbf{k}) d\tau + \sum_{\mu < \nu} 2 c_{\mu j}(\mathbf{k}) c_{\nu j}(\mathbf{k}) \int \chi_{\mu}(\mathbf{k}) \chi_{\nu}(\mathbf{k}) d\tau \\ &= \sum_{\mu} c_{\mu j}^2(\mathbf{k}) + \sum_{\mu < \nu} 2 c_{\mu j}(\mathbf{k}) c_{\nu j}(\mathbf{k}) S_{\mu\nu}(\mathbf{k}) \\ &= \sum_{\mu} NP_{\mu} + \sum_{\mu < \nu} OP_{\mu\nu},\end{aligned}\quad (98)$$

so that the Mulliken gross orbital population GP_μ can be written as

$$GP_\mu = NP_\mu + \frac{1}{2} \sum_{\nu} OP_{\mu\nu}. \quad (99)$$

In the density-matrix formalism, GP_μ is defined as

$$GP_\mu = \sum_{\mathbf{k}} \sum_{\nu} P_{\mu\nu}(\mathbf{k}) S_{\mu\nu}(\mathbf{k}) w(\mathbf{k}), \quad (100)$$

where $w(\mathbf{k})$ is the weight of delta-function integration of the corresponding \mathbf{k} -point and $P_{\mu\nu}(\mathbf{k})$ and $S_{\mu\nu}(\mathbf{k})$ are the \mathbf{k} -dependent density and overlap matrix elements for orbitals μ and ν , respectively,

$$P_{\mu\nu}(\mathbf{k}) = \sum_j f_j(\mathbf{k}) c_{\mu j}^*(\mathbf{k}) c_{\nu j}(\mathbf{k}), \quad (101)$$

$$S_{\mu\nu}(\mathbf{k}) = \langle \chi_{\mu}(\mathbf{k}) | \chi_{\nu}(\mathbf{k}) \rangle. \quad (102)$$

with the occupation number f_j of band j and the LCAO-CO coefficients $c_{\mu j}(\mathbf{k})$ in reciprocal space. To proceed with Löwdin population analysis, the basis set χ is orthogonalized, by applying Löwdin's symmetric orthogonalization (LSO).^{59,60} Using linear transformation, new basis sets χ' and new coefficient matrices C' are constructed from the old ones

$$\chi'(\mathbf{k}) = S^{-1/2}(\mathbf{k}) \chi(\mathbf{k}), \quad (103)$$

$$C'(\mathbf{k}) = S^{1/2}(\mathbf{k}) C(\mathbf{k}). \quad (104)$$

The new orthogonalized basis functions in Hilbert space are least distant from the original functions.⁶⁰ A new density matrix $P' = S^{1/2} P S^{1/2}$ is obtained and the Löwdin gross orbital population GP'_μ is computed as

$$GP'_\mu = \sum_{\mathbf{k}} P'_{\mu\mu}(\mathbf{k}) w(\mathbf{k}), \quad (105)$$

considering that the overlap matrix is the identity matrix in an orthonormal basis.

As mentioned above, wave function-based population analyses have been reported as basis sets dependent, which is true for molecular quantum chemistry. By projection of plane waves onto an auxiliary local basis set, like in the case of LOBSTER, this problem seemingly vanishes, so the new approach of plane waves based Mulliken and Löwdin charges in LOBSTER excels by combining the advantages of the plane waves (delocalization) and a local basis set, as illustrated in the figure below.⁶¹

The results for the 10-electron series of HF, H₂O, NH₃ and CH₄ are shown in Fig. 16. The panels on top provide the Mulliken and Löwdin hydrogen charges, respectively, from HF calculations.¹² Clearly, the charges first increase by expanding the basis set (STO-3G → 4-31G → 6-31G*) but then decrease for 6-31G**, showing a basis set dependence. This is not the case for charges calculated by LOBSTER as the lower panels provide H charges (now from plane-wave LDA calculation) calculated after LOBSTER projection. The calculation quality was successively increased by increasing the energy cutoff. At about 300 eV, the charges are independent of the basis set. As of now, an energy cutoff of about 500 eV is the de facto standard, so Mulliken and Löwdin analyses turn out as effectively basis-set-independent. This fortunate behavior results from the synergy of (i) the nonlocality of the plane-wave DFT basis set (which does not "know" about atoms) to begin with and (ii) the superb quality (completeness) of the local basis sets for analysis. The latter may be considered essentially complete because they consist of contracted multiple- ζ STO,^{125,126} known for supreme accuracy of only a few μ Hartrees above the numerical Hartree-Fock limit and ca. 0.002% concerning the average error of the electron density of the free atoms in the first and second period.

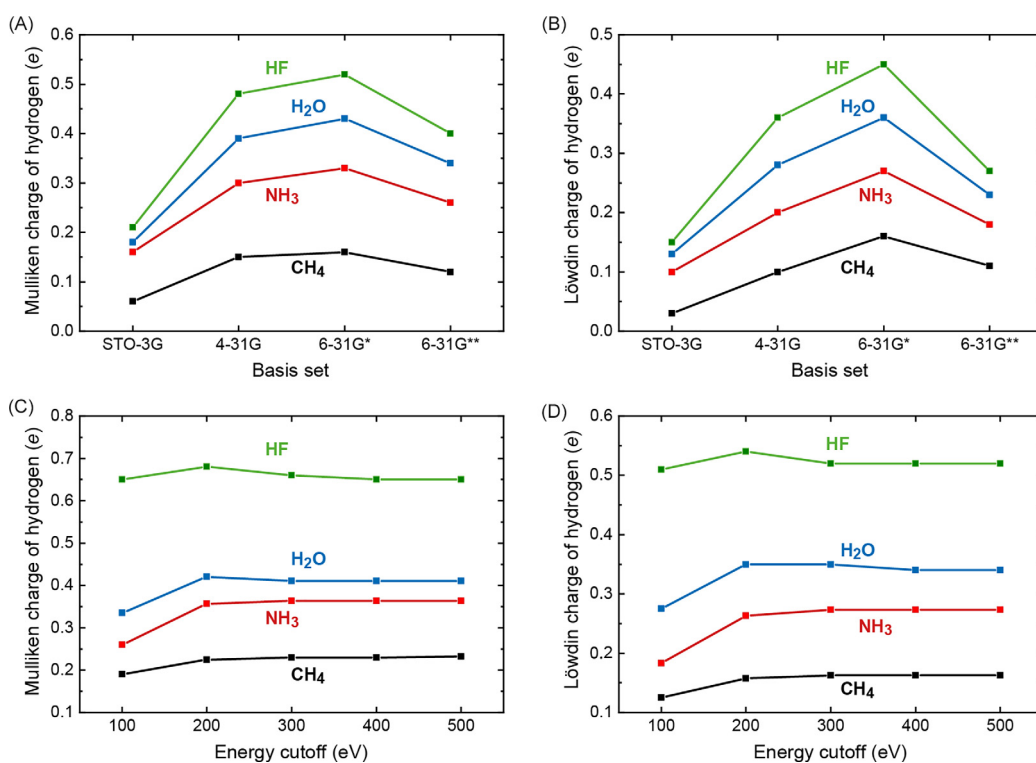


Fig. 16 A comparison of population analyses for methane, ammonia, water and hydrogen fluoride. (A) Mulliken and (B) Löwdin charges of the hydrogen atom based on Hartree-Fock calculations for different basis sets (STO-3G, 4-31G, 6-31G* and 6-31G**); data from.¹² (C) Mulliken and (D) Löwdin charges of the hydrogen atom based on PAW LDA calculations with varying energy cutoffs (= size of the plane-wave basis set).⁶¹ Reproduced with permission from Ertural, C.; Steinberg, S.; Dronskowski, R., Development of a Robust Tool to Extract Mulliken and Löwdin Charges From Plane Waves and Its Application to Solid-State Materials. *RSC Adv.* **2019**, *9* (51), 29821–29830—Published by The Royal Society of Chemistry.

3.07.2.9 Crystal orbital bond index

Apart from the COOP and COHP approaches, a similar and alternative quantity has been introduced in 2021,¹⁴⁴ which is the Crystal Orbital Bond Index (COBI). Its general idea is based on the bond index that was originally introduced by Wiberg in the framework of the CNDO (Complete Neglect of Differential Overlap) approximation.^{145–148} Because the Mulliken-type overlap integral cannot be used in case of an orthonormal basis set (as all overlap is zero), Wiberg developed a quantity referring to the absolute square of the off-diagonal elements of the density matrix¹⁴⁵:

$$\text{BI}_{\text{Wiberg}} = \text{Tr} |P_{\mu\nu}|^2. \quad (106)$$

This index was found to coincide exceedingly well with another quantity that chemists use intuitively, the chemical bond order. As an example, Fig. 17 shows the bond indices for the propene molecule. The C–H as well as the C–C single bonds possess bond indices of ≈ 1 while the C=C double bond has a value of ≈ 2.

Wiberg's bond index was later generalized by Mayer for a non-orthonormal basis set.^{149,150} This generalized bond index then reads

$$\text{BI}_{\text{Mayer}} = \text{Tr} (P_{\mu\nu} P_{\nu\mu}). \quad (107)$$

Both quantities can be used to quantify the covalent bond strength in an MO-type framework. The projection scheme introduced in section 3.07.2.5 is based on the same approach. Here, the total wave function is set up by an LCAO ansatz which allows for calculating a quantity that combines the ideas of the Wiberg/Mayer bond index with the COOP/COHP approach such as to

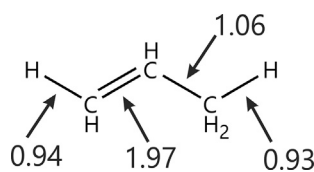


Fig. 17 Wiberg bond index for the propene molecule. Values calculated using LOBSTER.

incorporate the translational invariance of a solid-state material. For obvious reasons, it has been dubbed Crystal Orbital Bond Index (COBI) and it is completely analogous to the already established COOP and COHP methods, but with a significant advantage: Its integrated value, the ICOBI, equals the chemical bond order which is almost trivial to interpret for a chemist. The COBI reads very similar to the COOP and COHP, with the overlap and Hamilton matrix element replaced by a *density* matrix element:

$$\text{COBI}_{\mu\nu}(E) = P_{\mu\nu} \sum_{j,k} w_k \text{Re} \left(c_{\mu,jk}^* c_{\nu,jk} \right) \cdot \delta(\varepsilon_j(\mathbf{k}) - E) \quad (108)$$

The application of the COBI is shown for some textbook examples of materials with covalent and ionic interactions in Fig. 18.

The total bond index for the C–C-bond in diamond is almost as large as the classical value for a C–C single bond, just as expected from a covalently bonded diamond crystal. SiO_2 is another example of a covalent material, judging from its Si–O bond index of 0.76. At the same time, ionic interactions are also visible from the relatively large Löwdin charges for O (-0.9 e) and Si ($+1.81\text{ e}$). In NaCl, the ionic interactions are dominant judging from the charge transfer of 0.66 e from sodium onto chlorine. At the same time, the covalent interactions are negligible with an Na–Cl bond index of 0.09.

Analogously to the COHP and COOP, the COBI can be split into contributions from the orbitals that form the respective bond. In Fig. 19, all three bonding indicators are shown in an orbital wise description for the case of the $\text{N}\equiv\text{N}$ dinitrogen molecule. The advantage of the COBI formalism is obvious since not only does the ICOBI equal the chemical bond order — which makes it trivial to interpret—but the ratio of σ to π bonding is *exactly* the same as resulting from the familiar picture of the Lewis structure in which one electron pair makes a single σ bond and two electron pairs are responsible for the π bond. A similar correspondence is found neither for the COOP nor the COHP. Additionally, the COOP and the COHP show weak interactions at -3.5 eV and 0 eV belonging to the non-bonding states formed by the lone pairs. These states are caused by unequal bonding and antibonding interactions between the respective atomic orbitals of both nitrogen atoms. In the COBI, these states do not occur which indicates that the COBI allows a radically simpler understanding of chemical bonding in solid state materials.

An additional COBI feature is the possibility to examine interactions with more than two atoms. While COOP and COHP are limited, by their definition, to two-center interactions, the COBI can be extended to (theoretically) any number of atoms. Nonetheless, we will restrict ourselves to the three-center case for simplicity. The general procedure of the $\text{COBI}^{(n)}$ follows the n -center bond index that was introduced by Giambiagi et al.¹⁵¹ and Sannigrahi and Kar^{152,153} in the early 90s independently from each other. Their idea was to include additional density matrices into the calculation of the bond index:

$$\text{BI}_{\mu\nu\chi} = \text{Tr}(P_{\mu\nu} P_{\nu\chi} P_{\chi\mu}) \quad (109)$$

In its original definition, the three-center bond index cannot be set into context with bond indices of other rank. This follows from the idempotency of the density matrix which is

$$\text{Tr}(P^2) = \text{Tr}(2P) = 2N \quad (110)$$

for two atoms and

$$\text{Tr}(P^z) = 2^{z-1}N \quad (111)$$

for any number of z atoms. By including this relation into its definition, the comparability of bond indices of different rank can be ensured. Its final form then reads as¹⁵⁴

$$\text{BI}_{\mu\nu\chi\dots\zeta} = \frac{1}{2^{z-1}} \text{Tr}(P_{\mu\nu} P_{\nu\chi} \dots P_{\zeta\mu}) = N. \quad (112)$$

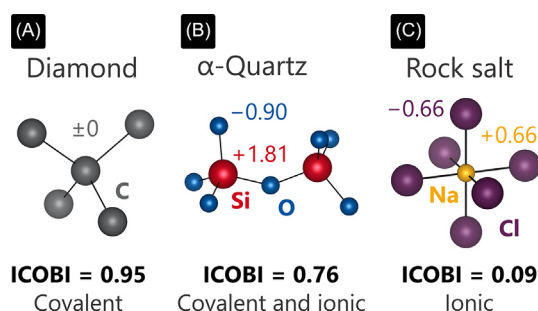


Fig. 18 Integrated Crystal Orbital Bond Index (ICOBI) and Löwdin charges for three model compounds: (A) Diamond as a completely covalent material. (B) SiO_2 in α -quartz structure as a compound with covalent as well as ionic interactions. (C) NaCl in rock salt structure as an ionic crystal with negligible covalent interactions. Adapted with permission from Müller, P. C.; Ertural, C.; Hempelmann, J.; Dronskowski, R., Crystal Orbital Bond Index: Covalent Bond Orders in Solids. *J. Phys. Chem. C* 2021, 125 (14), 7959-7970 Copyright (2021) American Chemical Society.

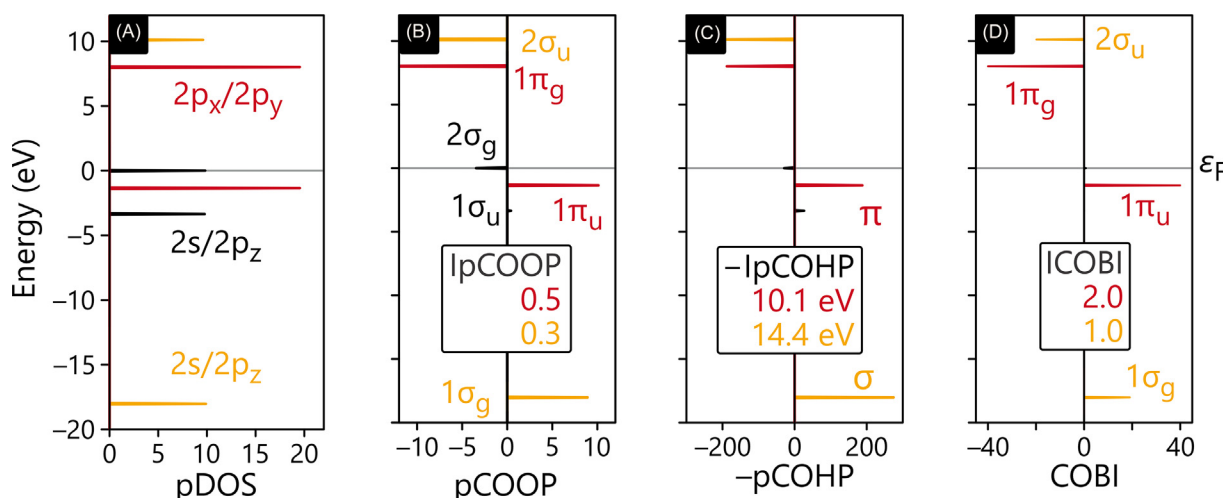


Fig. 19 (A) Density of states, (B) Crystal orbital overlap population, (C) crystal orbital Hamilton population and (D) Crystal orbital bond index of the dinitrogen molecule. Adapted with permission from Müller, P. C.; Ertural, C.; Hempelmann, J.; Dranskowsky, R., Crystal Orbital Bond Index: Covalent Bond Orders in Solids. *J. Phys. Chem. C* **2021**, *125* (14), 7959–7970. Copyright (2021) American Chemical Society.

The number of electrons that contribute to a certain interaction then is the sum over all permutations of the respective atoms. This can be accelerated by employing an orthonormal basis as in this case, the order of atoms in these permutations does not affect the final result. In a two- and three-center framework, the respective bond indices are

$$N_{\mu\nu}^{(2)} = \text{BI}_{\mu\nu} \quad (113)$$

$$N_{\mu\nu\chi}^{(3)} = \frac{3}{4} (\text{BI}_{\mu\nu\chi} + \text{BI}_{\nu\mu\chi}) = \frac{6}{4} \text{BI}_{\mu\nu\chi} \quad (114)$$

The n-center bond index can be generalized to the translationally invariant solid, just as the original two-center bond index:

$$\text{COBI}_{\mu\nu\chi}^{(3)}(E) = P_{\mu\nu} \cdot P_{\nu\chi} \cdot \sum_j w_k \text{Re} \left(c_{\chi,j\mathbf{k}}^* c_{\mu,j\mathbf{k}} \right) \cdot \delta(\varepsilon_j(\mathbf{k}) - E). \quad (115)$$

Note, however, that the simplification in Eq. (114) is only applicable to some degree. Since the density matrix already contains information on the occupation of molecular orbitals or bands, the energy dependence of the interactions between μ and ν as well as ν and χ in Eq. (115) is lost. This problem can be solved by summing over all cyclic permutations. The factor $\frac{1}{2}$ originates from the re-normalization factor that was multiplied by the number of cyclic permutations in Eq. (116).

$$\text{COBI}^{(3)}(E) = \frac{1}{2} \left(\text{COBI}_{\mu\nu\chi}^{(3)}(E) + \text{COBI}_{\nu\chi\mu}^{(3)}(E) + \text{COBI}_{\chi\mu\nu}^{(3)}(E) \right) \quad (116)$$

This three-center bond index can then be used to examine the presence of multi-center bonding in solid-state materials from a local-orbital perspective. In molecular chemistry, the octet rule is a guiding concept to judge molecular stability. As such, more or less labile compounds like B_2H_6 ¹⁵⁵ as well as XeF_2 ¹⁵⁶ violating $8-N$ can nonetheless be isolated. Since XeF_2 will be covered in section 3.07.3.1, we will focus on the case of B_2H_6 in the following example. Fig. 20 shows the respective DOS for boron as well as hydrogen, the two-centered COBI for the B–B as well as the B–H interactions, and the three-center COBI of the B–H–B three-center two-electron bond.

Upon comparing the respective DOS and the COBI, the origin of the three-center interaction becomes obvious: In the $\text{COBI}^{(3)}$, there are only three occupied levels that can clearly be attributed to the b_{1u} molecular orbital formed by the $2p_z$ and $2s$ orbitals of boron and the $1s$ orbitals of hydrogen (shown in red), and the a_g molecular orbital that results from the $2p_y$ orbitals of boron and $1s$ orbital of hydrogen (shown in blue). The $2p_x$ orbital of boron as well as the terminal hydrogen atoms do not contribute to the three-center two-electron bonds in the diborane molecule.

When comparing the three-center interaction to the two-center case, a connection between the B–B two-center bond and the B–H–B three-center bond becomes apparent. The main peaks in the $\text{COBI}^{(2)}$ are at exactly the same levels as the peaks in the $\text{COBI}^{(3)}$. From that, one can directly conclude that the boron atoms in B_2H_6 are not directly bonded but rather indirectly via the B–H–B bond. Direct bonding that may originate in a p_x-p_x or a p_z-p_z are negligible. These observations are in perfect agreement with the early models proposed by Longuet-Higgins and Lipscomb who suggested a bridging bond between two boron atoms and one hydrogen atom.^{157–159}

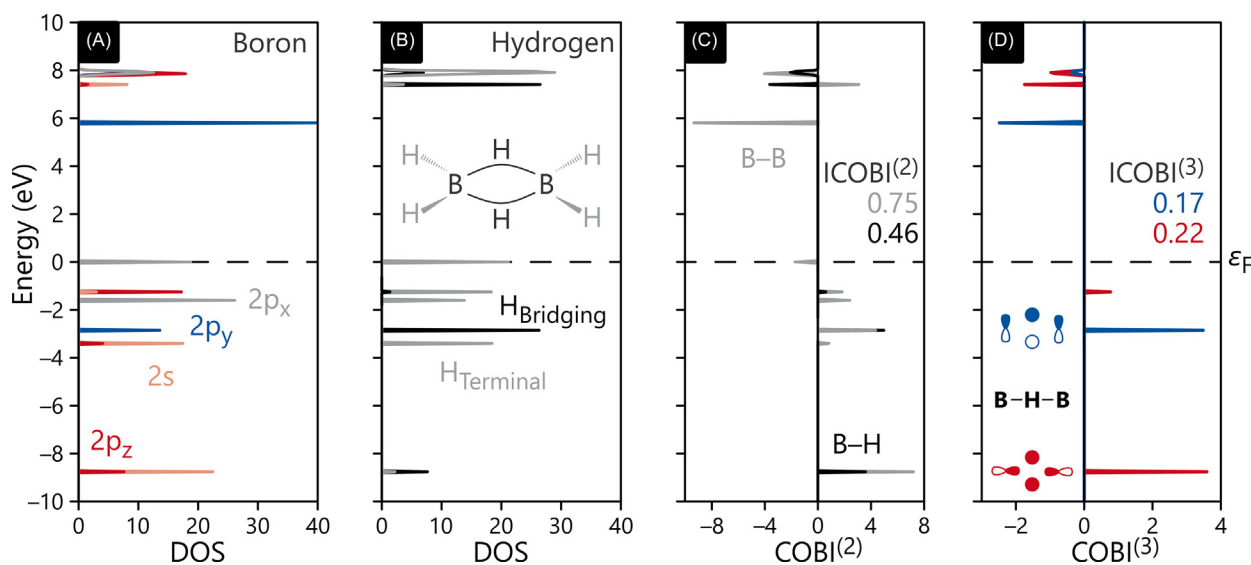


Fig. 20 (A) Density of states of boron, (B) Density of states of hydrogen, (C) 2-Center crystal orbital bond index for the B–H and B–B bonds in B₂H₆. (D) Orbitalwise 3-center crystal orbital bond index for the B–H–B bond in B₂H₆.

3.07.2.10 Averaged bonding descriptors

Due to their extended structural character, solid state materials can rarely be described using only one kind of interaction. Apart from simple compounds such as rock salt or diamond where the bonding situation is clear from the very beginning, a generalization is needed in order to extract a single quantity for a given crystal structure. In the following section, we will discuss some of these quantities that can generally be divided into two kinds of bonding mechanisms: covalency and ionicity.

3.07.2.10.1 Covalent bonding indicators: Averaged COHP and effective interaction number

For trivial reasons, an averaged COHP can be used to determine the average bond strength in a solid-state material.¹⁶⁰ Calculating an arithmetic average value, however, leads to certain problems: First, it is necessary to define some kind of cut-off for the bond length since long-ranged interactions tend to decrease in their strength and, thereby, lead to strengths close to zero. Second, this cut-off introduces an arbitrariness into the concept of an average which is somewhat questionable, especially for complex structures not allowing for an obvious definition of a spatial cut-off. The solution to this issue can be found in a *weighted average* COHP(E) that includes the bond strength ICOHP _{i} of a bond i relative to the total bond capacity ICOHP_{total} as present in the given structural unit.

$$\begin{aligned} \text{COHP}(E) &= \sum_i (w_i \cdot \text{COHP}_i(E)) \\ w_i &= \frac{\text{ICOHP}_i}{\text{ICOHP}_{\text{total}}} \end{aligned} \quad (117)$$

In this weighted average, long-ranged interactions have very small weights and consequently do not significantly affect the total result. Thereby, the crucial definition of an arbitrary cut-off is no longer needed. The course of the COHP(E) features all characteristics of the most “important” bonds in the given crystal, as can be seen in Fig. 21 for typical examples of covalent materials: Metallic silver, covalent diamond and the phase-change material GeTe. Just as the non-averaged COHP, the COHP can be integrated up to the Fermi-level. The resulting ICOPH can be interpreted as the average bond strength inside the given material:

$$\text{ICOPH} = \int_{-\infty}^{\epsilon_F} \text{COHP}(E) dE \quad (118)$$

It goes without saying that the weighted average can be applied to any analogous bonding indicator such as the COOP or the COBI in exactly the same way.

Apart from the strength of each bond, their sheer number is another important information for understanding the stability and reactivity of a chemical compound. In order to examine this kind of structural correlations, the concept of a coordination number (CN) was first introduced for coordinative compounds and later generalized for solid-state materials.^{161,162} In the first case, the definition of coordinating atoms is straightforward such as in cisplatin [PtCl₂(NH₃)₂]. Obviously, the platinum atom is coordinated by two chloride ions and two ammonia molecules resulting in a total coordination number of four. In solid state materials, this definition is not that simple because there are a lot more atoms in close vicinity to each other. In structures of the rock-salt type, the ions are octahedrally coordinated, resulting in a coordination number of six. However, there are contacts between ions that go beyond the first coordination sphere, which depends on the relative ion size as well as the structure type.¹⁶³

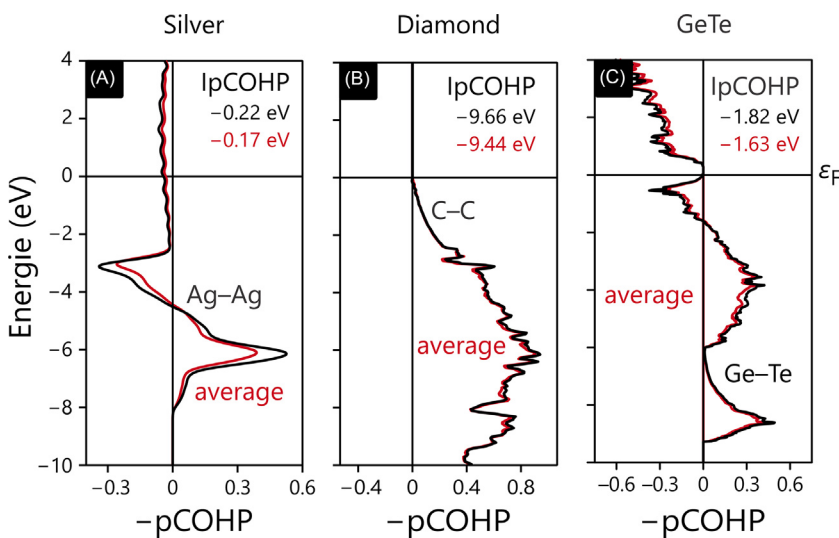


Fig. 21 COHP for the respective shortest bond and averaged COHP for (A) silver, (B) diamond and (C) cubic GeTe. The energy is relative to the Fermi level. The black curve corresponds to the respective shortest bonds in all three cases.

Fig. 22 elucidates this issue for the examples of LiI and KF, both crystallizing in the rock-salt structure type but differing significantly in the contacts of each ion. As the difference in ionic radii between Li^+ and I^- is large, there are I–I contacts while lithium only participates in Li–I interactions and no Li–Li can be found. In KF, the situation is different. Here, both ions have similar size, hence the coordination is mainly formed by K–F contacts and no significant K–K or F–F contacts exist. In order to achieve a quantitative interpretation of this picture, an effective coordination number (eCN) can be defined which includes higher coordination spheres into the calculation of the coordination number. This procedure may include the shape and surfaces of coordination polyhedra,¹⁶³ ratio of ionic radii,¹⁶⁴ or a scaling factor that decreases with increasing distance between ions.¹⁶⁵ However, the definition of a distance-based weighting factor is somewhat difficult because there is no general correspondence between the strength and the distance of a chemical bond.²⁶ In order to arrive at a quantity based on chemical bonding analysis, an effective interaction number (EIN) can be defined.¹⁶⁰ It is based on the averaged COHP that was introduced above.

$$\text{EIN} = \frac{\text{ICOHP}_{\text{total}}}{\text{ICOHP}} \cdot \frac{2}{N_{\text{Atoms}}} \quad (119)$$

The ratio of the total bond strength ICOHP_{total} and the average bond strength ICOHP corresponds to the total number of bonds inside a given unit cell. When this number is divided by the number of atoms N_{Atoms}, the number of bonds per atom is obtained, while the factor 2 leads to a quantity that is comparable to a coordination number. In **Fig. 23**, the effective interaction numbers are compared to the classical coordination numbers for three very different compounds: Silver as an example of metals with very large coordination numbers, diamond as a covalent material that usually possess low coordination numbers, and β -GeTe which crystallizes in [NaCl] structure type despite covalent dominance.

Silver crystallizes in the face-centered cubic structure with a coordination number of 12. This first coordination sphere contains a bond length of 2.9 Å which will likely be strongest. The second coordination sphere is at 4.1 Å and contains six atoms. The larger distance hints towards a weaker bond but larger than zero which manifests itself in an EIN of 22.4, almost twice the simple

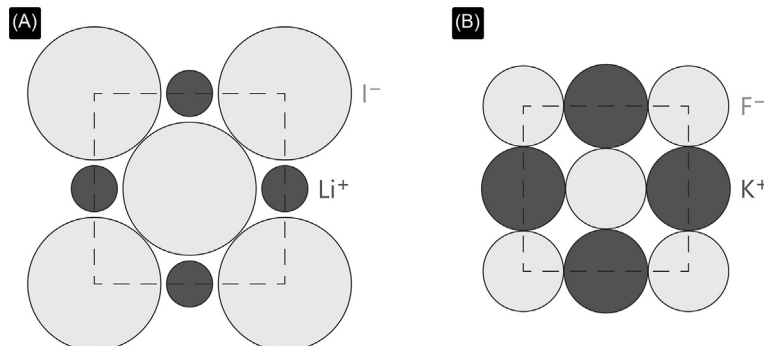


Fig. 22 (A) Coordination of I^- in LiI. (B) Coordination of F^- in KF. Based on reference Hoppe, R., The Coordination Number—An “Inorganic Chameleon”. *Angew. Chem. Int. Ed. Engl.* **1970**, 9 (1), 25–34.

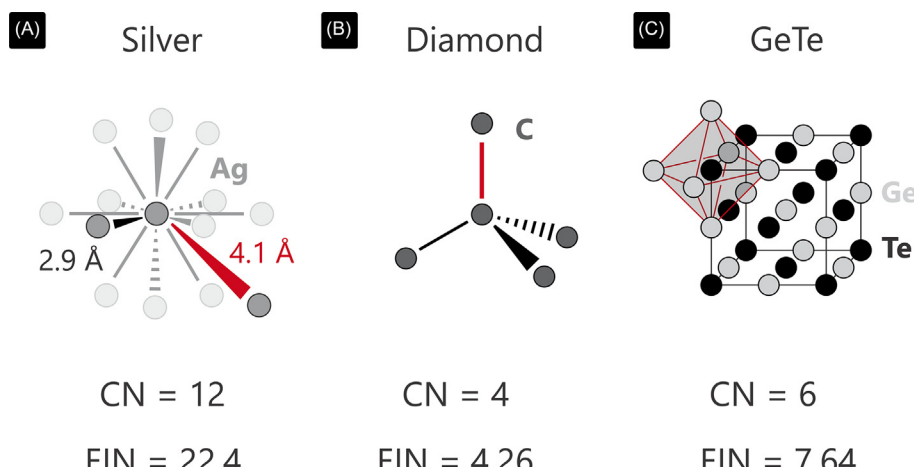


Fig. 23 (A) Coordination environment of silver in a face-centered cubic lattice. One representative bond of the first and the second coordination sphere are highlighted. (B) Coordination of carbon in diamond. (C) Unit cell of GeTe in the [NaCl] structure with highlighted coordination polyhedron of germanium.

coordination number. Diamond, on the other hand, does not show any significant long-ranged interaction. As such, the effective interaction number does not exceed the coordination number significantly, and the electrons are localized in the covalent bonds. The last example is GeTe, a phase-change material whose bonding properties have been extensively discussed.^{166–170} The EIN of 7.64 exceeds the coordination number by 27%, and this hints towards the presence of significant long-ranged interactions that will be analyzed further in section 3.07.3.8 within a local orbital framework. The ratio of EIN and CN can thus be seen as a measure of “electron delocalization” which has been postulated in the proposed bonding mechanisms. The larger this ratio is, the more delocalized the electrons. Trivially, values close to one indicate electron localization.

The effective interaction number can be applied to compounds where an effective coordination number faces difficulties. This could be, for example, defect structures with vacant or substituted atom positions, distorted and even amorphous compounds where a coordination sphere is very hard to define and, consequently, the effective coordination number is not applicable while the effective *interaction* number is. Additionally, the EIN combines features of structural chemistry and chemical-bonding analysis as a hole-in-one.

3.07.2.10.2 Ionic bonding indicators: Ionicity and Madelung energy

In addition to covalency, the ionic bond is a main source of a crystal’s cohesive energy. In order to quantify the strength of an ionic bond, a multitude of methods have been proposed in the literature. Probably the most famous one is the method by Pauling³ that scales with the difference in electronegativities X_A between the two members of a bond between A and B:

$$I_{\text{Pauling}}(\text{AB}) = 1 - \exp\left(-\frac{(X_A - X_B)^2}{4}\right) \quad (120)$$

This original definition yields the ionicity of a single bond, and it correlates well with the experimentally found ionicity based on electric dipole moments. If it is to be applied to a crystalline material of the composition A^NB^{8-N} with cationic valence N and coordination number CN, it has to be modified in order to respect influences of structure and valence electron count¹⁷¹:

$$I_{\text{Pauling,crystal}} = 1 - \frac{N}{\text{CN}} + \frac{N \cdot I_{\text{Pauling}}(\text{AB})}{\text{CN}} \quad (121)$$

This modification originates from resonating valence bond theory, stating that a covalent bond is distributed over all atoms in the direct coordination environment. Although Pauling’s approach has been useful especially in the field of molecular chemistry, it comes with certain disadvantages if one is interested in an ab initio approach. First, it is limited to a rigid class of compounds concerning stoichiometric and elemental composition. Second, it uses electronegativities that depend on experimental quantities. Third, the dependence on the structure complicates comparing values for strongly differing compounds.

The ionicity as defined by Esser et al.¹⁷² is based on quantum mechanically derived charges q_i that are put into relation of the valence v_i of each respective atom. The total ionicity is then averaged over all N_{Atoms} atoms in the unit cell:

$$I_{\text{Charges,old}} = \frac{1}{N_{\text{Atoms}}} \sum_i^{N_{\text{Atoms}}} \left(\left| 1 - \frac{\text{GP}_i}{v_i} \right| \right) = \frac{1}{N_{\text{Atoms}}} \sum_i^{N_{\text{Atoms}}} \left(\left| \frac{q_i}{v_i} \right| \right) \quad (122)$$

The original definition uses the number of valence electrons for an atom’s valence. This leads to certain issues considering anions which can easily be demonstrated at the example of sodium chloride. If we assume total charge transfer from the cation to the anion,

the ionicity should be 100%, but Eq. (122) only arrives at 0.57. In a real crystal, this value will be even smaller since charges rarely equal ideal oxidation states. With a small modification of its original definition, this problem can be solved. If an *effective* valence is employed, +1 for Na and -1 for Cl, the ionicity yields the expected values of 100% when total charge transfer is assumed in NaCl.

$$I_{\text{Charges}} = \frac{1}{N_{\text{Atoms}}} \sum_i^{N_{\text{Atoms}}} \left(\frac{q_i}{v_{\text{eff},i}} \right) \quad (123)$$

The definition of an effective valence is trivial for main group elements, where cations simply use their number of valence electrons and anions use the negative number of electrons missing for the noble gas configuration. The ionicities of some selected 8-N compounds are shown in Fig. 24 and compared to Pauling's definition that is based on electronegativities.

As is obvious from Fig. 24, both definitions of ionicity have large values for alkaline halides of which CsF is the largest in both, as expected. More covalent materials such as GaP possess very low ionicities in both, too. Besides this qualitative similarity, a 1:1 correspondence does not exist, especially when we look at halides such as LiI. In Pauling's scale, it has an ionicity of 0.89, whereas the charge is relatively small with a value of 0.55. A similar relation is found for many other compounds. This correspondence is due to a shortcoming of Pauling's definition that predicts large values and tends to overestimate ionicities.¹⁷³

In addition to the aforementioned problematic definition of valence for anions, the picture becomes even more difficult when transition metals are present. Here, it is not feasible to treat all electrons as valence, at least for the late metals. Copper and zinc have 11 and 12 electrons outside the [Ar] configuration but expecting every electron to participate in chemical bonding, being it covalent or ionic, contradicts all chemical knowledge, hence using an *effective* valence is the natural way to model this behavior, e.g., by treating the maximally achievable oxidation state as the number of valence electrons.¹⁷⁴ This results in an increase of valence from scandium to manganese and a decrease for the following elements, at least under standard conditions. For heavier metals, higher valences are found which is caused by a stronger shielding of the valence electrons by occupied 3d and potentially 4d levels.

Another way to quantify the electrostatic interactions in solid-state materials are Madelung energies,¹⁷⁵ the *electrostatic* part of the lattice energy; the latter equals the difference between isolated ions in the gaseous and the crystalline phase. The underlying mechanism is the Born-Haber cycle^{176,177} shown in Fig. 25 that is, the energy given as a state function: if all but one energy in the cycle are known, the remaining one is their difference. The lattice energy E_L is defined as energy difference (including the repulsion terms, those going beyond electrostatics) between ions in the gas phase and the crystal.

Admittedly, the Madelung energy is the largest part of the lattice energy, and the whole concept of Madelung energies depends on the ions being stable as gas species, which is not the case even for "simple" ions like O^{2-} and N^{3-} e.g., in TaON. Another difficulty lies in the long-ranged behavior of the Coulomb potential. As it scales with $\frac{1}{r}$, it will never vanish, even at very large distances. In combination with the number of ions in a crystal (infinite in theory), this hinders convergence of the sum of an infinite number of charges. In order to enforce convergence, numerous mathematical tricks have been developed by Ewald⁷¹ and others.^{69,178-180} The literature reflects that electrostatic calculations of the past often relied on the use of idealized atomic charges (= oxidation states) in solid-state materials, a clear oversimplification. In materials such as GaAs, Ga^{3+} and As^{3-} charges are unlikely as GaAs is covalent in its bonding properties and there is only a small difference in electronegativity between Ga (1.81) and As (2.18) within Pauling's scale. Also, the small coordination number of four hints towards a dominance of covalency and weak ionic contributions.¹⁸¹ An additional difficulty arises when molecular ions such as CO_3^{2-} in $CaCO_3$ or $N CN^{2-}$ in $HgCN$ are present in the crystal. In these molecules, it is almost impossible to assign reasonable charges, and the same is true for intermetallic and polar-covalent compounds.^{182,183} In order to solve this issue, wave function-based ion charges (Mulliken and Löwdin) appear handy, so the Ewald

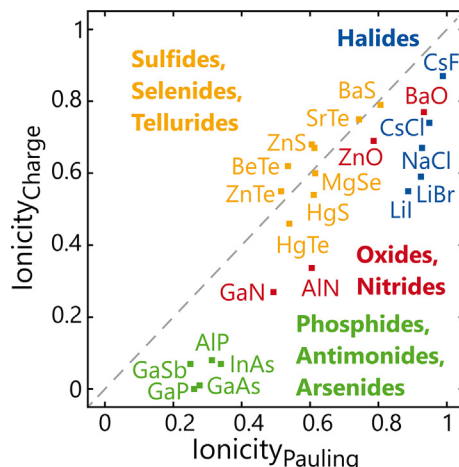


Fig. 24 Correlation between ionicity from quantum chemical charges and Pauling's definition of ionicity from electronegativities. The dashed line indicates a 1:1 correspondence.

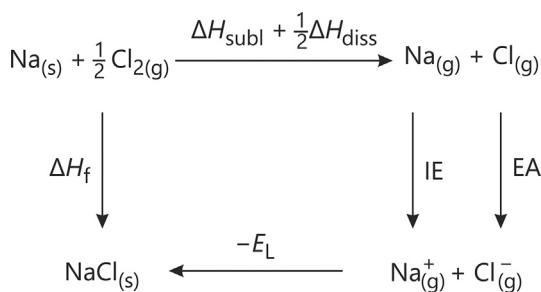


Fig. 25 Born-Haber cycle for the formation of NaCl. The lattice energy E_L can be calculated from the sublimation enthalpy of solid sodium ΔH_{subl} , the dissociation enthalpy of chlorine gas ΔH_{diss} , the ionization energy of the sodium atom IE, and the electron affinity of the chlorine atom EA. Reprinted from Dronskowski, R. *Computational Chemistry of Solid State Materials: A Guide for Materials Scientists, Chemists, Physicists and Others*. Wiley-VCH: Weinheim (2005) with permission from John Wiley and Sons.

method⁷¹ has also been implemented into LOBSTER.¹⁴⁴ This very method splits the Coulomb-potential into two sums that converge independently from each other.

$$\nu_{\text{total}}(j) = \nu_1(j) + \nu_2(j) \quad (124)$$

The first potential ν_1 is a Gaussian distribution of charges excluding the ion at the reference position j .

$$\nu_1(j) = \frac{4\pi}{V} \sum_G S(G) G^{-2} \exp\left(-\frac{G^2}{4\eta}\right) - 2q_j \sqrt{\frac{\eta}{\pi}} \quad (125)$$

In this potential, V is the unit cell volume, G is a vector in reciprocal space, q_j is the charge of the atom j , η is the Ewald splitting parameter that determines the splitting of the total potential into real and reciprocal space. The long-ranged interactions are dealt with by the structure factor $S(G)$ which is built over all charges q_k of atoms k inside the given unit cell and their distance d_{jk} from the reference atom j .

$$S_j(G) = \sum_k q_k \exp(iG \cdot d_{jk}) \quad (126)$$

The second potential ν_2 determines the short-ranged interactions. Convergence is achieved by the complementary error function $\text{erfc}(x) = \frac{2}{\sqrt{\pi}} \int_x^\infty e^{-t^2} dt$.

$$\nu_2(j) = \sum_l \frac{q_l}{r_l} \text{erfc}(\sqrt{\eta} r_l) \quad (127)$$

As both potentials converge independently from each other, so does their sum. As such, the total electrostatic energy can be determined as

$$\varepsilon_M = \frac{1}{2} \sum_j q_j \nu_{\text{total}}(j). \quad (128)$$

The splitting parameter η in Eqs. (126) and (127) is the only user-defined quantity. Small values mean fast convergence of ν_1 and slow convergence of ν_2 , whereas for large values of η , the relation is reversed. In practice, a compromise has to be found for simultaneous convergence of both potentials. The cutoff radii in reciprocal space k_{cutoff} and real space a_{cutoff} can be estimated for a given accuracy ε ¹⁸⁴:

$$k_{\text{cutoff}} = 2 \cdot \sqrt{\eta} \cdot \sqrt{-\ln(\varepsilon)}, \quad (129)$$

$$a_{\text{cutoff}} = \frac{\sqrt{-\ln(\varepsilon)}}{\sqrt{\eta}}. \quad (130)$$

For the optimal ratio η_{opt} , a dependence of number of atoms N_{Atoms} and volume V of the unit cell was found:

$$\eta_{\text{opt}} = \pi \left(\frac{N_{\text{Atoms}}}{V} \right)^{\frac{1}{3}} \quad (131)$$

Based on this method, it is possible to determine the relative stability of any crystalline material, purely based on electrostatic considerations. Other phenomena such as covalency and lattice dynamics (at finite temperature), however, may have influences that can lead to different structures being found in reality.¹⁸⁵

3.07.3 Part III: Applications

3.07.3.1 Molecular systems

In the introductory part, we have demonstrated how chemical-bond formation in a molecule is handled within MO theory. Because PW-based DFT calculations are not restricted to periodic systems, molecular systems can also be treated using PW based quantum chemical programs like VASP. An interesting type of molecular systems is seen in molecules involving noble gas elements. Peculiar compounds, such as XeF_4 or XeF_2 are, at first sight, seemingly unstable molecules because of completely filled valence orbitals of the noble gases to begin with. We are now covering hypervalent molecules whose bonding situation cannot be explained by the recipes given so far. A glimpse into the structure and MO diagram is given in Fig. 26.

The MO bonding situation with the Pimentel-Rundle model includes the 5p orbital of Xe and the 2p orbitals of the two F atoms in a σ -type manner (cf. Fig. 26). The energetically lowest lying molecular orbital consists of p orbitals of all three atoms. The next occupied MO is a non-bonding level while the energetically highest antibonding level remains unoccupied. In total, this gives us a stabilizing interaction between Xe and F in a Pimentel-Rundle three-center-four-electron (3c4e) bond model.^{186–188} With the crystal orbital bond index (COBI) gained by a projection from a PAW based DFT calculation with LOBSTER,¹⁴⁴ the MO theory picture of the Pimentel-Rundle model as in Fig. 26 can be confirmed.

The two-center as well as the three-center (Fig. 27) COBI show three interactions for F–F and F–Xe–F and two for Xe–F. The energetically lowest COBI⁽²⁾ interaction type is bonding for Xe–F and antibonding for F–F, whereas the level between -2 eV and the Fermi energy is bonding for F–F and not present (therefore non-bonding) for Xe–F. In the energetically highest, unoccupied level, it is antibonding for both interactions. With a percentage of 86.6% for the ICOBI⁽³⁾ p–p–p interaction on the total ICOBI⁽³⁾, the three-center bond is clearly dominated by p-orbital interaction. The ICOBI⁽²⁾(p–p) in the F–F interaction has the same ratio to the total ICOBI⁽²⁾ like ICOBI⁽³⁾(p–p–p) to total ICOBI⁽³⁾, so we may conclude that the F–F interaction is consequence of the three-center F–Xe–F bond. A ICOBI⁽³⁾ value being negative is an indication for an electron-rich bond. The total ICOBI⁽²⁾(Xe–F) = 0.49 also coincides with the expected bond order of 0.5 derived from the MO diagram in Fig. 26.¹⁴⁴

Lying between the realm of non-periodic (i.e., molecular) systems and 3D-periodic (i.e., ideal crystal) systems, a carbon nanotube and C_{60} fullerene are interesting objects to study and to compare them with graphite. The structure of a single nanotube is translationally invariant in only one dimension (like in Fig. 28B shown along c). Since it can be seen as a single graphene layer wrapped up into a tube, the bonding nature of the nanotube is expected to be pretty close to that in graphite. Because of the structural connection, a change in the electronic structure from graphite to the carbon nanotube can be observed.¹²¹

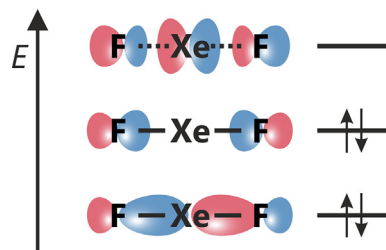


Fig. 26 The linear structure and representation of molecular orbitals of XeF_2 modeled according to the Pimentel-Rundle model^{186–188} of the 3c4e σ -type bond.

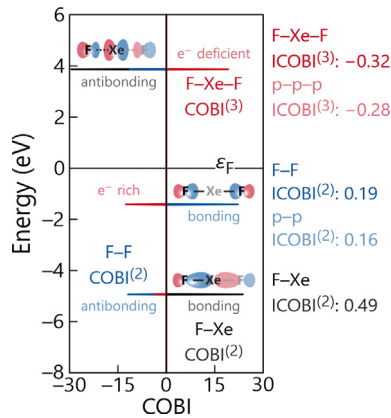


Fig. 27 Two-center (COBI⁽²⁾) for F–F and Xe–F as well as three-center (COBI⁽³⁾) COBI for F–Xe–F interaction in XeF_2 . Corresponding MOs of XeF_2 are exemplarily emphasized for one bonding Xe–F, one bonding F–F and one antibonding Xe–F interaction.

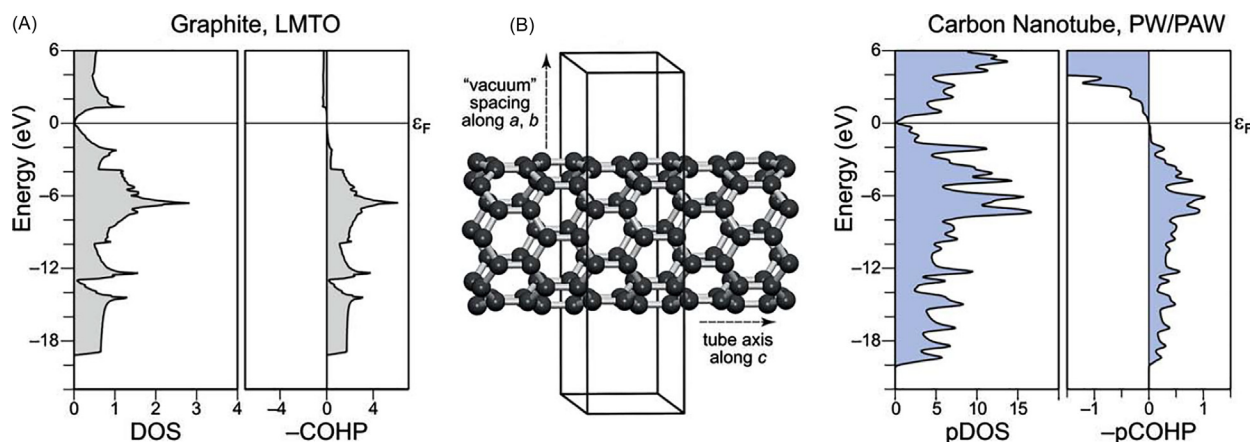


Fig. 28 (A) DOS and $-COHP$ for graphite (obtained with the traditional TB-LMTO-ASA).^{91,189} (B) Simulation cell of the carbon nanotube and (C) the pDOS and $-pCOHP$ for the nanotube obtained with LOBSTER.¹²¹ From Maintz, S.; Deringer, V. L.; Tchougréeff, A. L.; Dronskowski, R., Analytic Projection From Plane-Wave and PAW Wavefunctions and Application to Chemical-Bonding Analysis in Solids. *J. Comput. Chem.* **2013**, *34*, 2557–2567.

As seen in Fig. 28A and C, the (p)DOS and the negative (p)COHP of graphite and carbon nanotube are very similar to each other. The most obvious difference is that the curves of the nanotube show more discretization in form of “spikes” and therefore less smoothness which stems from the finite diameter of the tube. With a larger radius of the tube, the material’s properties would become more similar to that of graphite¹⁹⁰ since the bending distortion decreases. A chemical bonding feature that graphite and this carbon nanotube share is the energy region right below the Fermi level: upon going from the Fermi level to -2 eV, nonbonding levels (as seen in the (p)COHP plot) can be observed, followed by bonding levels up to -19 eV. The energy window between -19 eV and -12 eV, as pointed out by Hoffmann,¹⁹¹ appears as a fingerprint area for “ sp^2 ” hybridized, quasi 2D-extended structures, from which graphite is an archetypical representative. It seems that the carbon nanotube does not show this type of fingerprint which probably is also a consequence of the bending of the structure and the resulting distortion of the planar “ sp^2 ” hybridized orbital structure.¹²¹

Another type of interesting nanostructure and allotrope of carbon is the C_{60} fullerene molecule.

Compared to graphite and the carbon nanotube, a progressing discretization can be seen in the pDOS and pCOHP plot, which is expected since C_{60} is a zero-dimensional molecule. Still the similarity in pDOS and pCOHP from C_{60} fullerene to graphite and the carbon nanotube remain to some extent. Two interatomic distances between carbon can be observed in the C_{60} fullerene molecule (cf. Fig. 29A), a “single” bond with a bond length of 1.45 \AA and a “double” bond with 1.40 \AA . The inset in Fig. 29B evidences that in case of the “double” bond, all bonding levels are fully occupied, whereas the “single” bond shows nonbonding levels just below the Fermi level. With an $IpCOHP$ value of 6.4 eV, the “double” bond is also slightly stronger than the “single” bond ($IpCOHP = 5.9$ eV).¹²¹

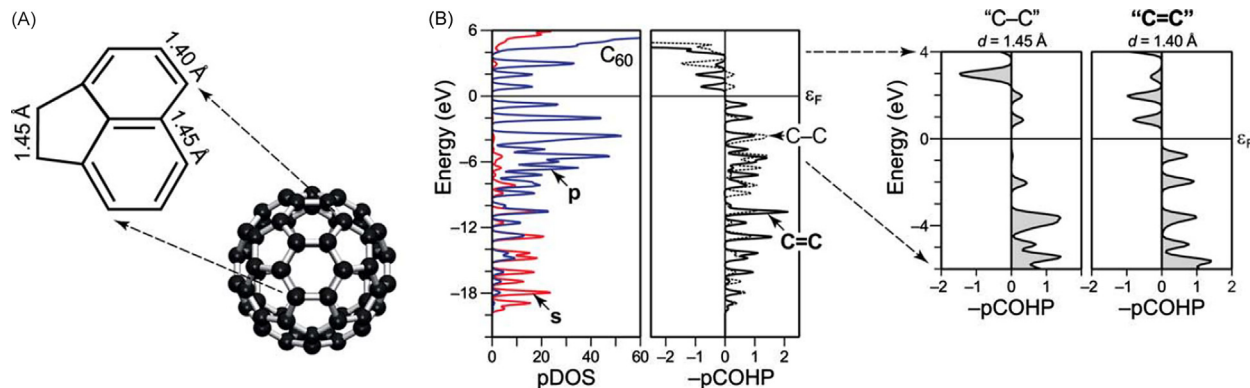


Fig. 29 (A) Model of the C_{60} fullerene molecule highlighting the two different bond lengths. (B) pDOS analysis for s and p orbitals in C_{60} and $-pCOHP$ analysis for the two bonds highlighted in (A). The inset on the right zooms to a smaller energy window around the Fermi level.¹²¹ From Maintz, S.; Deringer, V. L.; Tchougréeff, A. L.; Dronskowski, R., Analytic Projection From Plane-Wave and PAW Wavefunctions and Application to Chemical-Bonding Analysis in Solids. *J. Comput. Chem.* **2013**, *34*, 2557–2567.

3.07.3.2 Bonding between molecules (H and X bonding), bonding on surfaces

In addition to the aforementioned (largely covalent) bonding interactions in textbook molecules, the crystalline state in particular lets us witness other bonding types, even when they are already known from the molecular world. Probably the most important example is given by the ubiquitous hydrogen bond^{8,9} already introduced before. Let's reiterate that H bonding is not a bonding type of its own but a complicated mélange between covalency, ionicity, and also dispersion interactions. Because it is so important (in particular for storing genetic information), it is often referred to as bonding type no. 5. Generally speaking, we talk about a hydrogen bond D–H···A if a covalent, polar D^{δ−}–H^{δ+} bond and a polar atom A^{δ−} interact; here, D is called the donor and A the acceptor atom. One may also classify hydrogen bonds based on their energy, namely strong (>63 kJ mol^{−1}), moderate (17–63 kJ mol^{−1}), and weak (<17 kJ mol^{−1}). Strong hydrogen bonds are usually short with an almost linear D–H···A shape.

The crystal structure of guanidine is an excellent example of a system held together by a complex array of hydrogen bonds, and its complexity may be the reason why guanidine was structurally clarified only belatedly, namely in the 21st century although the molecule is known since the late 19th century; guanidine is astonishingly difficult to crystallize.¹⁹² Fortunately, plane-wave DFT is able to quantitatively model the hydrogen bonds despite the fact that the presence of dispersion interactions would require wave-function-based methods such as CCSD(T) for that,¹⁹³ at least in principle. That is to say that in such a case DFT needs to be modified or augmented, in a sense, for example by adding a somewhat empirical dispersion correction ("+D") to the exchange-correlation functional.¹⁹⁴ Likewise, nonempirical, essentially DFT-derived correction parameters are possible as well,¹⁹⁵ even entire van-der-Waals functionals¹⁹⁶ are known. The true power of plane-wave DFT is then due to the fact that it is entirely free of local-orbital bias and of basis-set superposition errors, and the method may also put molecules and solids on equal footing.

When crystalline guanidine and its eight symmetry-independent hydrogen bonds are looked at using such plane-wave DFT+D approach, the H-bonding strength is easily quantified by systematic calculations of dimers, chains, layers, and the three-dimensional crystal itself,¹⁹⁷ namely by computationally compressing and stretching those entities. It then turns out that five out of eight hydrogen bonds are of moderate strength, two are strong, and one hydrogen "bond" is surprisingly nonbonding, so the initial structure-derived assignment of H-bonding is invalid in this particular case. Eventually, the cooperativity of hydrogen bonding (telling us whether or not the whole is more or less than the sum of its ingredients) automatically falls off from the calculations. One finds both cooperativity (more energy gain) and anti-cooperativity (less), and the entire guanidine crystal enjoys an energetic H-bonding cooperativity of 14%.

A related plane-wave study targeting hydrogen bonding exists for α -chitin, the abundant biopolymer stabilizing the exoskeleton of insects and giving structure to plants. DFT-D confirms previous propositions of interchain links via the acetylamine moieties, caused by strongly cooperative N–H···O=C bonds, and the overall interchain stabilization exceeds 250 kJ mol^{−1}. In addition, the crystallographically known disorder is found to originate from the necessity of allowing for both intra- and interlayer stabilization because α -chitin requires two different H-bonding motifs to stabilize its rigid three-dimensional structure.¹⁹⁸

Eventually, the question of covalency of a hydrogen bond may be investigated, but only when plane-wave electronic-structure data are projected on a local orbital basis by means of LOBSTER. The covalency of H-bonding has been under debate for long,¹⁹⁹ most often looked at from the experimental electron density and its topology. Fortunately, the crystalline compound *N,N*-dimethylbiguanidinium bis(hydrogensquare)ate for which accurate experimental data are available allows for a decisive analysis. Its anion dimer, depicted in the left part of Fig. 30, contains two O–H···O bonds at 1.421(4) Å and 1.569(4) Å.

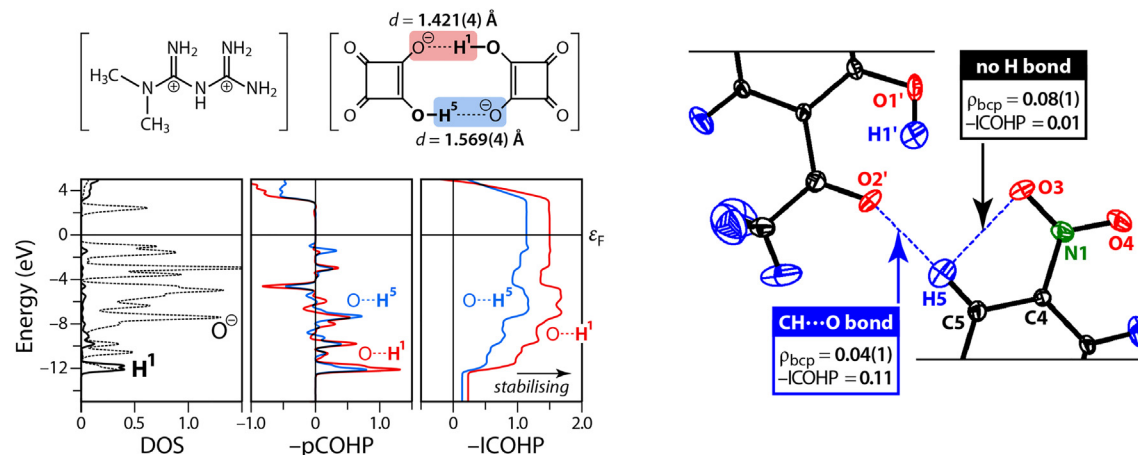


Fig. 30 Quantifying H-bonding in dimers of hydrogensquare anions (top left) and the corresponding DOS, projected COHP and ICOHP diagrams (bottom left), revealing strength differences in covalency. Detecting existent and non-existent H-bonds by means of ICOHP in 1-(2-hydroxy-5-nitrophenyl)ethanone (right). Reproduced from Ref. Deringer, V. L.; Englert, U.; Dronskowski, R., Covalency of Hydrogen Bonds in Solids Revisited. *Chem. Commun.* 2014, 50 (78), 11547–11549 with permission from the Royal Society of Chemistry.

particular, their ICOHP energy integrals arrive at 149 and 104 kJ mol⁻¹, respectively, corroborating their different strengths.²⁰⁰ In fact, the entire set of hydrogen bonds in this molecule involving O and N atoms rapidly decays with increasing H···X distances, unlike those involving C atoms.

As a hole-in-one, such wave-function-based analysis exhibits a great advantage over density-based schemes, as easily shown for the molecule 1-(2-hydroxy-5-nitrophenyl)ethanone visualized in the right part of Fig. 30. If one were to detect hydrogen bonding based on the electron density of the bond-critical point, one would not only spot an intermolecular H bond between O2' and H5, but an even stronger *intramolecular* H bond between O3 and H5, incorrectly so. Only the wave-function-based ICOHP value, however, shows the latter to be nonexistent. We iterate that COHP (but not the density) involves the *phases* of the interacting atomic orbitals, defining the difference between bonding (constructive interference) and antibonding (destructive interference).²⁰⁰ The density does not provide that information.

Interactions which involve second-nearest atomic neighbors, to put it this way, not only exist under the name hydrogen bonding. Likewise, halogen bonding (and also chalcogen, pnictogen, and even tetrel bonding) have recently come to the surface in molecular chemistry, in particular in supramolecular chemistry although the first report goes back to the 19th century.²⁰¹ We use the term halogen bond (XB) to group those relatively weak bonding interactions of a halogen atom that is otherwise covalently bonded and whose local electronic structure corresponds to an already filled noble gas shell, as depicted in Fig. 31A, and chalcogen, pnictogen, and tetrel bonds follow an analogous definition. The X atom possesses a sigma-hole (a region of positive electrostatic potential, ESP) to which a suitable partner with an outer negative ESP may be electrostatically attracted. To study the cooperativity of such bonds in the crystal, plane-wave DFT is perfectly capable because it treats molecular dimers, trimers, etc. as well as the infinite solid exactly with the same computational methodology. Hence, Fig. 31B directly visualizes how the interaction energy grows with the amount of condensation, and this very energy between dimers of ICN and a one-dimensional ICN crystal increases from 22.8 to 40.8 kJ mol⁻¹, an 82% boost.²⁰² As shown in Fig. 31C, the amount of interaction energy and also cooperativity in molecular cyanides then increases while moving from halogens to chalcogens to pnictogens, and the heavier homologues of each main group excel both in interaction strength and cooperativity,^{202,203} clearly a function of growing electronic polarizability of those atoms, as exemplified before.²⁰⁴

The extreme case is found for tetrel bonding, as expected, for which cooperativity may amplify up to 60% such that tetrel bonds (say, in $\text{Tr}(\text{CN})_4$) can amount up to 70% of the overall interaction energy within some crystals. The tetrel bonds of the heavy Sn atom are significantly shorter and stronger than those of C, Si, and Ge, and one finds strong covalency (by COHP analysis) mirroring the interaction energies.²⁰⁵

And yet, there is surface bonding, either between atoms within the surface, thereby defining the structure of a crystal's surface, or between the surface and a molecule interacting with that surface. For obvious reasons, a surface is the strongest possible perturbation of a crystal, so there is a long tradition in trying to structurally characterize a surface, say, by scanning tunneling microscopy (STM) or spectroscopy (STS) or even X-ray photoelectron spectroscopy (XPS). Because it is notoriously difficult to achieve a structural resolution comparable to standard XRD measurements for extended crystals, density-functional theory may be of tremendous help, in particular plane-wave DFT using so-called supercells.²⁶ For reasons that will become clear in the next section, the so-called (111) surface of germanium telluride is a fine starting point because the underlying crystal structure is relatively simple (close to rock salt, NaCl) but still electronically exciting, too. That being said, it is rather straightforward to model such a GeTe(111) surface, yielding results which sound familiar and intuitively reasonable to every chemist: whatever the chemical surrounding, a pristine Te-covered (111) surface is energetically favorable over a purely Ge-terminated surface by about 60 meV Å⁻². The former surface directs all the anions (formally Te²⁻ with all frontier orbitals and the electronic octet completely filled) to the vacuum while the latter involves two 4s² surplus electrons on each formal Ge²⁺ such that various structural reconstructions are about to happen, simply to make better use of those two nonbonded electrons.²⁰⁶ When such surfaces are exposed to molecular and atomic oxygen, it does not come as a surprise that the Te-terminated surface is repulsive to O₂ as it would represent a nonmetal-nonmetal surface reaction. The corresponding Ge-terminated (111) surface of GeTe, however, readily sucks in molecular oxygen, and given the right absorption site this may lead to a rupture of the O₂ molecule, resulting in an O²⁻ anion slightly below the surface and an isolated O atom bonded on top of that surface.²⁰⁷ Such plane-wave DFT results afford a detailed, atom-resolved picture of the initial GeTe surface oxidation of GeTe, in harmony with independent XPS studies.²⁰⁸

Eventually, the entire GeTe surface will corrode and consist of germanium's most stable oxide, germanium dioxide. While bulk GeO₂ is known to adopt the quartz type, just like the lighter homologue SiO₂, a plane-wave DFT study allows to straightforwardly model the most relevant GeO₂ surfaces, both freshly cleaved and structurally optimized, the numerical optimization including time-consuming density-functional molecular-dynamics runs. Among all the surfaces, those dubbed (100)_α and (100)_β are particularly relevant, and they are depicted in the upper part of Fig. 32:

Both surfaces contain GeO₄ tetrahedra, as expected, but they are corner-sharing in the α surface polymorph and edge-sharing in the β polymorph. At the same time, α lies significantly lower in energy than β , in particular after reconstruction. The chemical reason for that phenomenon is found in the lower part of Fig. 32 showing a projected COOP analysis of the Ge–O bonds directly at the surface (in blue) and below ("slab center"). Note that the COOP integral at the surface (1.02 for α and 0.94 for β) corresponds to the bond population, and the lower value for the β polymorph exemplifies what is known as Pauling's third rule, but now for the surface, that is, beyond the bulk. Because there is more strain upon edge-sharing (or more electrostatic repulsion between the central Ge "cations", thereby allowing for an electrostatic interpretation), the (100)_β is the less stable surface polymorph, in full accordance with Pauling's third rule. It is a reassuring sign of modern electronic-structure and bonding theory that such findings which relate to Ge–Te covalent bond strengths may be (semi-)automatically generated by means of locally projected density-functional theory.

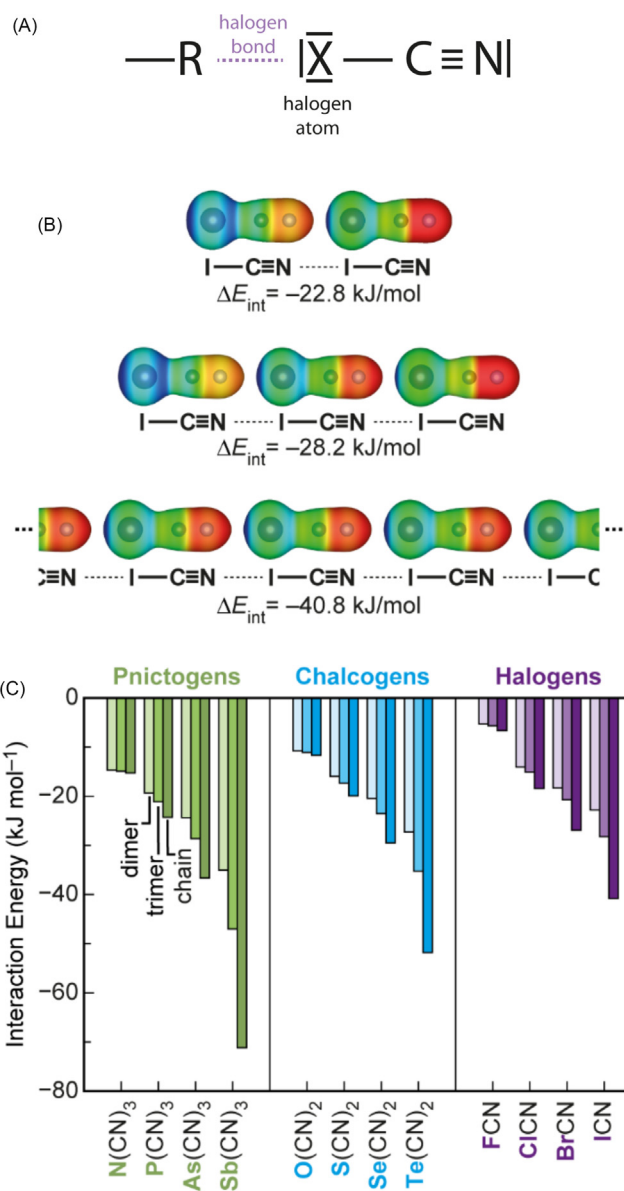


Fig. 31 (A) Sketch of a halogen bond in a molecular cyanide. (B) Charge-density isosurface ($0.05 \text{ electrons } \text{\AA}^{-3}$) plots of dimers, trimers, and infinite chains of halogen-bonded ICN molecules and their interaction energies. (C) Cooperativity diagram for pnictogen, chalcogen, and halogen bonds in various cyanide molecules. Reprinted with permission from George, J.; Deringer, V. L.; Dronskowski, R., Cooperativity of Halogen, Chalcogen, and Pnictogen Bonds in Infinite Molecular Chains by Electronic Structure Theory. *Chem. A Eur. J.* **2014**, *118* (17), 3193–3200. Copyright (2014) American Chemical Society.

By doing so, one may build a bridge between first-principles theory and classical chemical reasoning which we consider a value in itself.²⁰⁹

3.07.3.3 Semiconductors such as GaAs and Phase-change materials

For elemental semiconductors, the electronic structure of diamond and its density-of-states (DOS) diagram as depicted in Fig. 14 provides a perfect starting point. Irrespective of the method of calculation, there is massive 2s-2p mixing which, given the correct electron filling of four electrons per atom, leads to an entirely C–C bonding valence and antibonding conduction band. Moving down in main-group IV towards the heavier homologues Si and Ge, there is quantitative change in semiconductor physics but not so much in terms of bonding. The band gap of diamond (5.5 eV) shrinks to reach values of 1.14 eV (Si) and 0.67 eV (Ge), just as expected while approaching metallic tin and lead, but the bonding character of valence and conduction band stays about the same, with perfectly optimized homoatomic single bonds.

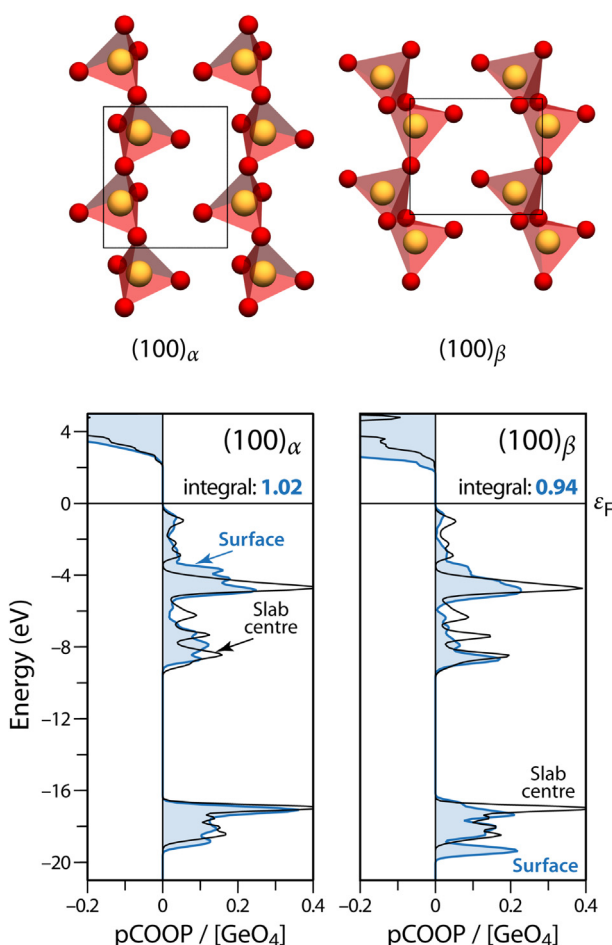


Fig. 32 Structural sketches of two different (100) surfaces of germanium dioxide involving corner- and edge-sharing GeO_4 tetrahedra (top) and their Ge–O chemical-bonding analysis (bottom) by means of projected COOP, distinguishing between atoms within the slab center and on the surface (blue shading). Reproduced from Deringer, V. L.; Dronskowski, R., Pauling's Third Rule Beyond the Bulk: Chemical Bonding at Quartz-Type GeO_2 Surfaces. *Chem. Sci.* **2014**, 5 (3), 894–903 with permission from the Royal Society of Chemistry.

For the germanium example, an “electronegativity perturbation” would consist in replacing two Ge atoms by one Ga and one As atom such that the average electron number of GaAs, $\frac{1}{2}(3 + 5) = 4$, stays the same, so the III–V semiconductor GaAs is isoelectronic with Ge. Even stronger but still isoelectronic perturbations are given by GaP and GaN. Their electronic DOS results are depicted in Fig. 33.

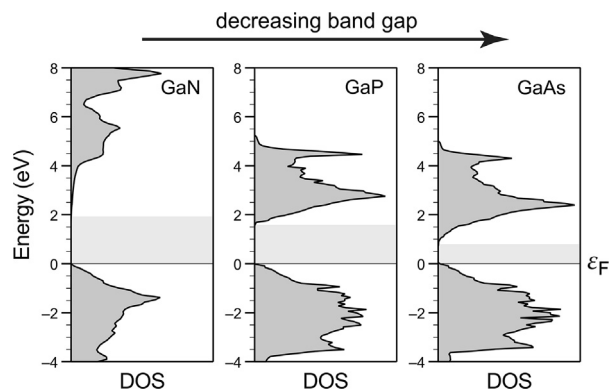


Fig. 33 Electronic DOS of GaN, GaP, and GaAs, showing a decrease in ionicity and band gap as function of decreasing electronegativity difference. Reprinted from Deringer, V. L.; Dronskowski, R., Computational Methods for Solids. In *Comprehensive Inorganic Chemistry II: From Elements to Applications*, Reedijk, J.; Poeppelmeier, K., Eds. Elsevier: Amsterdam, 2013; vol. 9, pp 59–87 with permission from Elsevier.

Just as expected, a stronger electronegativity perturbation leads to a larger band gap, and vice versa, but the valence/conduction band remains bonding/antibonding. In contrast to the elemental semiconductor and not shown here for brevity reasons, however, one finds a direct band gap instead of an indirect one. It is important to emphasize that GaN, GaP, and GaAs all fulfill the $8 - N$ rule since the total number of valence electrons arrives at 8, either calculated as $3 + 5 = 8$ for the neutral atoms or as $0 + 8 = 8$ for the formal ions Ga^{3+} and N^{3-} , for example. Such primitive calculus even holds true for the even more ionic examples of CaSe and KBr.

For an iconic IV-VI phase-change material such as GeTe, however, both chemistry and physics drastically change as a consequence of the electron count, either calculated as $4 + 6 = 10$ for Ge and Te, or as $2 + 8 = 10$ for Ge^{2+} and Te^{2-} . Before discussing the structure, we recall that phase-change materials (PCMs) operate by employing at least two solid-state phases of distinctly different physical properties, which can be used to encode “one” and “zero” bits, and rapidly switched back and forth. The original idea²¹⁰ is sketched in the upper part of Fig. 34, and it forms the basis of modern data-storage technologies such as re-writeable Blu-ray discs.²¹¹

Coming back to germanium telluride, this 1934 material²¹² adopts a NaCl-like crystal structure depicted in the lower part of Fig. 34 in which both Ge and Te are octahedrally coordinated.²¹³ The presence of “lone-pair” $4s^2$ electrons on divalent Ge, however, is visible, indirectly so, because these electrons lead to a small but significant symmetry lowering which no longer allows for the cubic but the hexagonal crystal system. Alternatively expressed, the formally “nonbonding” leftover electrons of divalent Ge make the GeTe_6 octahedra distort a little such that we have shorter and longer Ge–Te bonds, a phenomenon sometimes expressed by the “directional lone pair” effect in the chemical literature. In the language of band theory, we are witnessing yet another Peierls distortion with a loss of translational symmetry,⁵² but now three-dimensional in nature and no longer one-dimensional like the one in Section 3.07.1.6.

More quantum-chemical insight can directly be visualized from first-principles calculations of α -GeTe crystallizing in space group $R\bar{3}m$, in particular by looking at the electronic DOS and the projected COOP analysis which are shown in the upper part of Fig. 35. The occupied DOS region consists of three parts which turn out of as Ge–Te bonding at lowest energies (part A), a little bonding and nonbonding at medium energies (part B), and bonding as well as antibonding below the Fermi energy (part C).²¹⁴

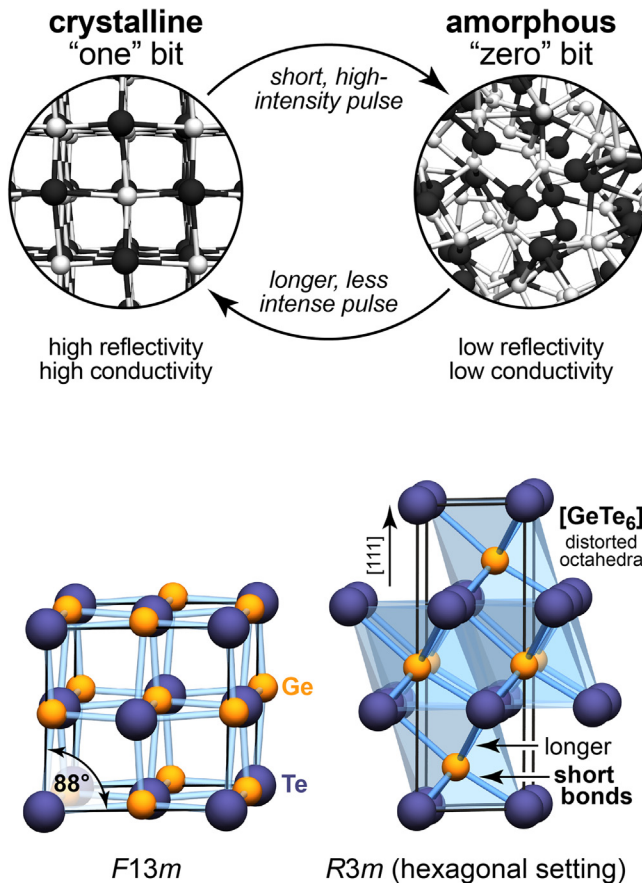


Fig. 34 The functional idea of phase-change data storage (top) switching between crystalline and amorphous phases, thereby writing and reading information encoded as “one” and “zero”, carried out using either laser or current pulses. The Peierls-distorted crystal structure of germanium telluride (α phase) adopting a quasi-rocksalt structure (bottom left) with space group $F13m$, usually described with a hexagonal setting and space group $R\bar{3}m$ (bottom right). Reprinted from Deringer, V. L.; Dronskowski, R.; Wuttig, M., Microscopic Complexity in Phase-Change Materials and Its Role for Applications. *Adv. Funct. Mater.* **2015**, 25 (40), 6343–6359 with permission from John Wiley and Sons.

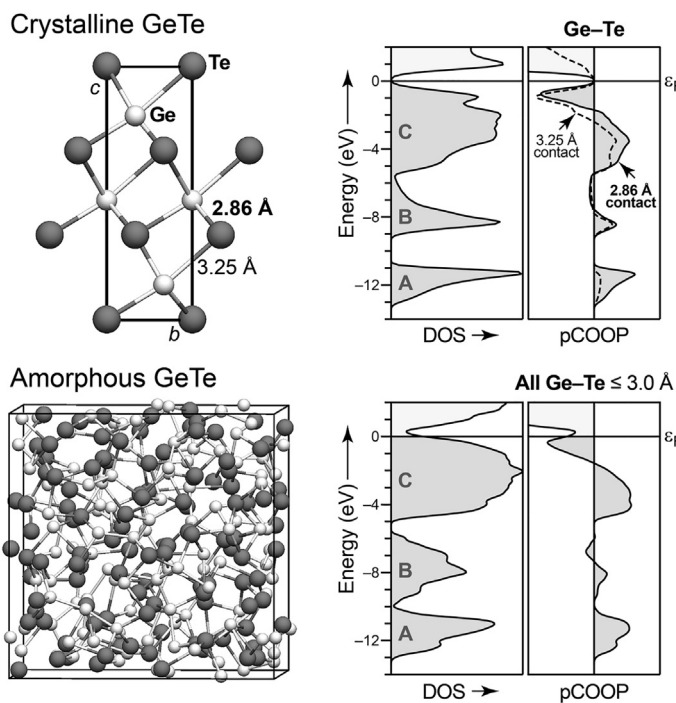


Fig. 35 Structural sketches of crystalline and amorphous GeTe (left) and corresponding DOS and Ge–Te projected COOP analysis (right). Reprinted from Deringer, V. L.; Zhang, W.; Lumeij, M.; Maintz, S.; Wuttig, M.; Mazzarello, R.; Dronskowski, R., Bonding Nature of Local Structural Motifs in Amorphous GeTe. *Angew. Chem. Int. Ed.* **2014**, *53* (40), 10817–10820 with permission from John Wiley and Sons.

Simplifying things a bit, germanium's $4s^2$ "lone pair" shows up from those antibonding effects, somewhat destabilizing the structure and allowing for alternative structures which do not differ much in terms of energy.

In fact, amorphous GeTe is such an alternative (although non-crystalline) structure. We provide a sketch of its computational model generated by ab initio molecular dynamics,²¹⁵ together with DOS and pCOOP in the lower part of Fig. 35. Just like in the crystalline phase, there are unfavorable antibonding Ge–Te levels close to the Fermi level, and the amount of antibonding is even a little larger than in the crystalline case, so GeTe cannot escape from the consequences of its two excess electrons.²¹⁴ A closer analysis, not shown here for reasons of brevity but employing the definition of a "bond-weighted distribution function" (BWDF), reveals that the amorphous phase also includes GeTe_4 fragments and even Ge–Ge bonds, thereby trying to locally "heal" the unfavorable electron count which is too large to begin with. Recall that GeTe, with 10 valence electrons, does not fulfill the $8 - N$ rule.

Similar observations have been made much earlier, in the context of PCMs being chemically closer to those really being industrially used in nowadays technology. There is a material with the approximate composition $\text{Ge}_2\text{Sb}_2\text{Te}_5$ (dubbed as "GST" by physicists and engineers) which, in addition to its ground-state structure, also crystallizes in a metastable NaCl-like phase, and the phase is known to always contain Ge vacancies, strangely enough (but only at first sight). For comparison, we note that the formation of Si vacancies in crystalline Si costs about 3.3 eV. After having set up a simplified computational model of a NaCl-like supercell of " $\text{Ge}_2\text{Sb}_2\text{Te}_4$ ", taking out Ge atoms one after the other leads to a fascinating consequence which we present in Fig. 36.

Those earlier DFT calculations, carried out using local-orbital methods and the original COHP approach, once again evidence filled antibonding levels close to the Fermi levels,²¹⁶ so the Ge–Te and Sb–Te bonds suffer from the too large electron count (10.5) of $\text{Ge}_{0.5}\text{Sb}_{0.5}\text{Te}$ ($= \frac{1}{2} \text{Ge}_2\text{Sb}_2\text{Te}_4$), just like in GeTe itself. Nonetheless, nature partially alleviates the problem by kicking out Ge atoms. Grossly simplified, the germaniums are the least electronegative atoms, hence they are the most "cationic" to begin with, and they provide the electrons taken by the "anionic" Te atoms. This immediately explains why less Ge-rich materials have a lower Fermi energy and fewer populated antibonding interactions. Of course, fewer Ge atoms also translate into fewer Ge–Te bonds, so there is a tentative compositional optimum for $\text{Ge}_{1.5}\text{Sb}_2\text{Te}_4$. Consequently, one would also expect Ge vacancies for the original GeTe composition, and there is experimental evidence for GeTe being slightly berthollide, too.²¹⁷

That being said, PCMs owe their physical properties to their unfavorable valence-electron count violating the $8 - N$ rule, and nature annihilates the resulting antibonding interactions, at least in part, by symmetry lowering (Peierls case) to begin with and/or vacancy formation (lowering of the electron count). The latter optimization of the electron count, however, can also be chemically tailored, on purpose. InTe with an electron count of $3 + 6 = 9$ also contains too many electrons, and one may fabricate a good phase-change material *without* structural defects adopting the [NaCl]-like lattice,²¹⁸ namely by replacing one third of the tellurium atoms by antimony atoms, so we have $\frac{1}{3}(\text{In}_3\text{Sb}_2\text{Te}_2)$ with an electron count of 8.67. For $\text{In}_3\text{Sb}_2\text{Te}_2$ dubbed "IST", there is a similar reduction of antibonding levels, and "IST" is a fine phase-change material indeed, even more stable at distinctly higher temperatures than "GST".²¹⁹

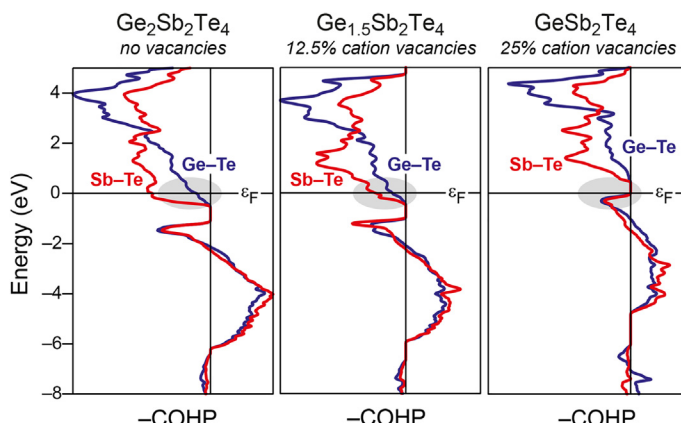


Fig. 36 COHP chemical-bonding analysis of Ge–Te and Sb–Te interactions in stoichiometric and Ge-defect variants of $\text{Ge}_2\text{Sb}_2\text{Te}_4$. Upon lowering the electron-delivering Ge-cation concentration, nature diminishes unfavorable antibonding interactions (grey shadings). Reprinted from Deringer, V. L.; Dronskowski, R.; Wuttig, M., Microscopic Complexity in Phase-Change Materials and Its Role for Applications. *Adv. Funct. Mater.* **2015**, *25* (40), 6343–6359 with permission from John Wiley and Sons.

And yet, there is another way to reduce or even annihilate such antibonding interactions, accidentally found by clarifying existence, stoichiometry, and crystal structure of a selenium-rich material dubbed “ $\text{GeSe}_{1-x}\text{Te}_x$ ” first reported in the 1960s.²²⁰ When single crystals of the mica-like material with the correct composition $\text{Ge}_4\text{Se}_3\text{Te}$ were eventually grown by advanced chemical transport employing molecular GeI_4 , the subsequent structural characterization by XRD and high-resolution transmission electron microscopy²²¹ allowed for proper understanding, as illustrated from Fig. 37A. $\text{Ge}_4\text{Se}_3\text{Te}$ is a descendant of the α -GeTe structure type in which a single $\text{GeSe}(\text{Te})$ layer is flipped by 180° such as to realize a *layered* crystal structure, see Fig. 37B, with van-der-Waals contacts between Se/Te atoms (hence the mica-like appearance) and also close Ge–Ge contacts of about 2.94 \AA , wider than those Ge–Ge single bonds in elemental Ge but still significant. Plane-wave DFT+D in combination with local-orbital projection using LOBSTER then rounds off the picture and provides a simple chemical interpretation which is visualized in Fig. 37C.

If $\text{Ge}_4\text{Se}_3\text{Te}$ were to crystallize in the α -GeTe structure with space group $R\bar{3}m$, it would suffer from the same antibonding Ge–Se and Ge–Te interactions close to the Fermi level which we already witnessed in Fig. 35 (top), the reason being the too large electron count. By flipping one $\text{GeSe}(\text{Te})$ layer and adopting hexagonal $P\bar{6}_3mc$ symmetry, however, nature dumps those formerly antibonding electrons in newly established Ge–Ge bonds, highlighted in red in the right part of Fig. 37C. By doing so, nature also strengthens the Ge–Se(Te) bonds as well.²²¹ Those chemical-bonding arguments can even be extended to include all interactions in the crystal, thereby partitioning the band-structure energy and generating an electronic “fingerprint” of all stabilizing and destabilizing effects in their entirety, a technique dubbed as “density-of-energy” or simply DOE. All that, however, requires the automatic reconstruction of the electronic structure by means of atomic orbitals, now so easily done.

3.07.3.4 Spin polarization and magnetic systems

It seems puzzling, at first sight, that the influence of the electron’s spin on chemical bonding usually gets underestimated, although any quantum-chemical treatment using a first-principles or ab initio technique (in contrast to a semi-empirical one such as extended Hückel theory) does require an explicit treatment of spin-dependent phenomena. In addition to electronic *correlation* (which sums up all leftover interelectronic repulsion even when the Pauli principle²¹ has been properly accounted for) there is electronic *exchange* which makes us take care of both spin-up (α) and spin-down (β) orientations of the electron’s spin, so easily done within Hartree-Fock theory and a single Slater determinant for the molecule under question, (see Section 3.07.1.3).

Take molecular hydrogen, H_2 , for example. As detailed before in Section 3.07.1.2, there are two electrons which occupy the lowest σ_g molecular orbital, one spin-up, the other spin-down. This “spin-pairing” is usually regarded, incorrectly so, as a fingerprint of chemical bonding although it clearly *costs* energy to keep both electrons in the bonding molecular orbital; to relieve the inter-electronic repulsion, this would be accounted for by configuration interaction, so there is still a little correlation energy to gain by (partially) unpairing the two electrons and occupying the antibonding σ_u^* molecular orbital.

The qualitative energetics of such “spin-pairing” or “spin-unpairing” is easily demonstrated from the physically transparent model of an electron gas, and we are then facing what has been coined as the “exchange hole” (by the physicists) or the “Fermi hole” (by the chemists). Without going too much into the details, which have been described elsewhere,²⁶ the chance of finding a spin-up/spin-down ($\alpha\beta$) pair is exactly $1/2$, irrespective of the interelectronic distances, so we will find 1 electron (either α or β) wherever we look. On the other side, when two α electrons or two β electrons will come very close to each other, the $\alpha\alpha$ or $\beta\beta$ pair density will rapidly drop to zero because the Pauli principle is at play, so these electrons should also differ in their spin orientations. While this spin-dependency has no immediate consequences for a system with equal numbers of α and β spins (say, two α and two β), it has tremendous consequences if, say, one electron flips its spin orientation such that we arrive at three α and one

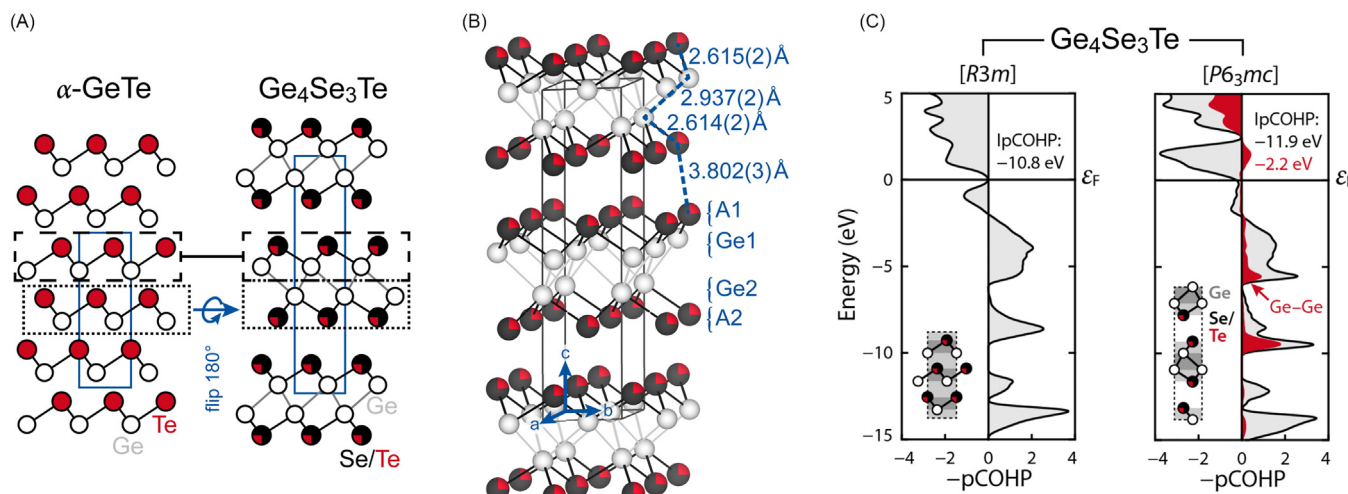


Fig. 37 (A) Principle of the structural evolution from α -GeTe to $\text{Ge}_4\text{Se}_3\text{Te}$ by flipping one layer. (B) Actual crystal structure of $\text{Ge}_4\text{Se}_3\text{Te}$ involving weak van-der-Waals contacts between Se/Te atoms and stronger Ge–Ge bonds. (C) Chemical bonding in $\text{Ge}_4\text{Se}_3\text{Te}$ assuming the GeTe structure and the real crystal structure; by flipping one layer, nature redistributes electrons from formerly Ge–Te antibonding levels into bonding Ge–Ge levels (in red). Reprinted from Küpers, M.; Konze, P. M.; Maintz, S.; Steinberg, S.; Mio, A. M.; Cojocaru-Mirédin, O.; Zhu, M.; Müller, M.; Luysberg, M.; Mayer, J.; Wuttig, M.; Dronskowski, R., Unexpected Ge–Ge Contacts in the Two-Dimensional $\text{Ge}_4\text{Se}_3\text{Te}$ Phase and Analysis of Their Chemical Cause with the Density of Energy (DOE) Function. *Angew. Chem. Int. Ed.* **2017**, *56* (34), 10204–10208 with permission from John Wiley and Sons.

β electrons. Because of the exchange hole, the majority α electrons cannot shield the other α electrons very well (remember that they cannot get too close to each other) whereas the minority β electrons are very well shielded by the majority α electrons. Hence, the majority α electrons experience a *higher* nuclear charge and go *down* in energy whereas the minority β electrons see a *lower* nuclear charge and *rise* energetically.

Chemistry holds a great molecular example for this effect, molecular triplet oxygen, ${}^3\text{O}_2$. Compared to N_2 with a triple bond, there are two more electrons which occupy the doubly degenerate π^* antibonding molecular orbitals, resulting in a double bond, and these two electrons will immediately *unpair* and thereby slightly strengthen O–O bonding; the spin-paired ${}^1\text{O}_2$ is less stable by ca. 0.95 eV. Upon unpairing, the two electrons also both adopt the same spin orientation (α), as expected from Hund's rules. Because of the higher effective nuclear charge felt by the α electrons, they go down in energy and their associated spin orbitals contract. A corresponding β electron (of which there is none in this case) would be more shielded, move up in energy, and its spin orbital would become more diffuse, as nicely visualized in Fig. 38.

In that difference plot of the α and β spin orbitals,²²³ it is easy to recognize the spatial domain of the majority spins, in red and close to the nuclei, and the one of the minority spins, in blue in the outer region. It is important to remember that spin-majority orbitals are more contracted, less available for interatomic bonding, in contrast to the more diffuse spin-minority orbitals. And all that happens to strengthen the O–O bonding as the chemist would phrase it. A simple comparison with the higher homologue, sulfur, and its ${}^3\text{S}_2$ molecule shows that the effect of spin polarization is less profound here. The reason is that the 3p electrons of sulfur are already shielded by the inner 2p electrons (not so for oxygen because there are no 1p electrons), so the effective nuclear has been lowered already, and so the exchange splitting will be smaller.

Something similar also happens in the 3d transition metals which our physicist friends usually call "itinerant" (= delocalized) metals. If we calculate the band structure, the DOS, and the COHP of body-centered cubic iron using local orbitals, even the simplest functional (LDA) assuming no spin polarization lets us witness a fundamental effect, depicted in Fig. 39. In the band structure, there is one 4s band and three 3d bands going up and down in energy. The corresponding DOS has a characteristic three-peaked shape (typical for bcc metals), and practically everything, except the grey 4s contribution, is 3d in character. The COHP shows, however, not only bonding but one occupied *antibonding* Fe–Fe interaction at the Fermi level which looks extraordinarily for a stable system. One would surely expect such system to undergo a structural distortion (say, Peierls-like) in order to get rid of the

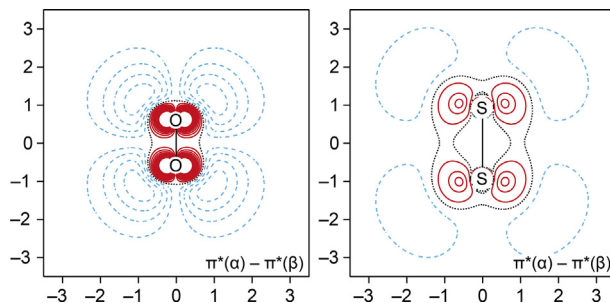


Fig. 38 Difference plots for the π^* antibonding orbitals of ${}^3\text{O}_2$ and ${}^3\text{S}_2$. Reprinted from Landrum, G. A.; Dronskowski, R., The Orbital Origins of Magnetism: From Atoms to Molecules to Ferromagnetic Alloys. *Angew. Chem. Int. Ed.* **2000**, *39* (9), 1560–1585 with permission from John Wiley and Sons.

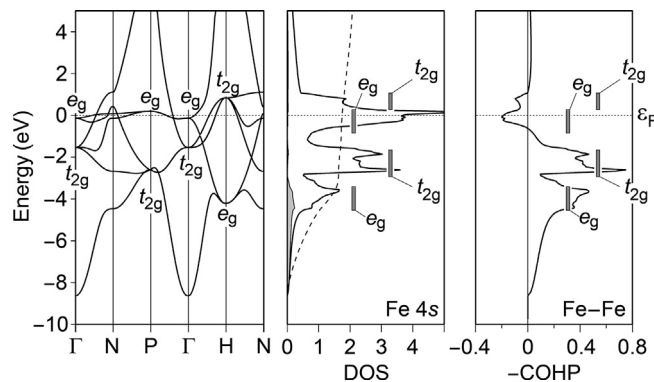


Fig. 39 Non-spin-polarized band structure, densities-of-states and Crystal Orbital Hamilton Population (COHP) of body-centered cubic iron, as calculated using local orbitals (TB-LMTO-ASA) and the LDA. Note the occupied antibonding interaction at the Fermi level on the right. Reprinted from Landrum, G. A.; Dronskowski, R., The Orbital Origins of Magnetism: From Atoms to Molecules to Ferromagnetic Alloys. *Angew. Chem. Int. Ed.* **2000**, *39* (9), 1560–1585 with permission from John Wiley and Sons.

antibonding combination but there is yet another way to electronically "heal" the system: spin polarization (or unpairing), just like in molecular oxygen.²²³

This very consequence of spin polarization (or spin unpairing) can be nicely visualized, not only from local orbitals, but also from plane waves if the chemical information has been properly extracted, that is, projected using auxiliary local orbitals.¹²² The result is presented in Fig. 40.

In the non-spin-polarized scenario on the left, one finds Fe–Fe antibonding in a nonmagnetic metal. If we allow for spin polarization as depicted in the right part, the majority spins lower in energy while the minority spins move up; as a result, there will be about 2.2 unpaired electrons (or Bohr magnetons) as given from a corresponding DOS plot (not shown). Because of the different contraction/expansion of the α and β spin orbitals, the formerly antibonding peak at the Fermi level has practically disappeared, the total energy has lowered, and the chemical bonding has strengthened by about 5%. Please note that the COHP integral of the α spins (in red) below the Fermi level is smaller than the one of the β spins, one of the reasons being that the more diffuse β orbitals are more engaged in Fe–Fe bonding simply due to their larger expansion. This also explains why the lattice parameter of magnetic bcc-Fe is slightly *larger* than in nonmagnetic bcc-Fe, needed by nature to maximize the overlap between the more diffuse β spin orbitals.

The aforementioned findings are easily transferred to the likewise ferromagnetic elements Co and Ni, with very similar results, and they allow to predict body-centered cubic Mn to be predicted as being a ferromagnet as well. In addition, this chemical theory of itinerant magnetism²²³ also allows for understanding itinerant anti-ferromagnetism such as in bcc-Cr.²²⁴ Likewise, intermetallic compounds with tailored magnetic properties can be easily designed and also synthetically realized.²²⁵

The great advantage of plane-wave theory, however, shows up from its ability to easily deal with "open" systems such as clusters or surfaces. In particular for the latter, the question of magnetism is of extraordinary importance, so we will look at it in more detail. It has been predicted quite a while ago that a monolayer of ruthenium, if put on a slab of silver atoms, will show ferromagnetic properties. That being said, a chemical-bonding analysis of Ru–Ru bonding seems appropriate, as depicted in Fig. 41.

Just like for the iron case, the higher homologue also shows significant exchange splitting and, as a consequence, a strengthening of Ru–Ru bonding while unpairing the spins.¹²² And what seems exceptional at first sight, looks like a general principle for systems that tend to spin-polarize due to sufficient exchange splitting. For example, transition-metal carbodiimides such as MnNCN, the nitrogen cousin of MnO, also show similar phenomena because COHP analysis evidences that adopting the ground-state magnetic structures is achieved by optimizing the cation-anion bonds through annihilating instabilities, that is, the existence of antibonding states in the vicinity of the Fermi level.²²⁶

3.07.3.5 Rechargeable battery electrode materials

Bonding indicators and charge algorithms can significantly help to improve and further develop battery materials, even finding new compounds with improved qualities and higher efficiency. Understanding such materials on an atomic scale may lead to rechargeable batteries with improved longevity, safety and duration, an essential step for the battery and communication technology.^{227–235} The energy in batteries is electrochemically stored via reversible conversion or intercalation reactions. For the more prevalent intercalation batteries, metal oxides, silicates or phosphates are often used for the cathodes, whereas graphite-based anode materials are widespread.^{227,233,236–241} Having a look at anode materials for Li and Na ion batteries is particularly interesting and important because Li and Na behave differently when intercalated into graphite based anode compounds. Anode lithium materials usually consist of Li atoms intercalated into pristine graphite sheets^{236,241,242} (like LiC₆ or LiC₁₂ which are commonly used) while Na

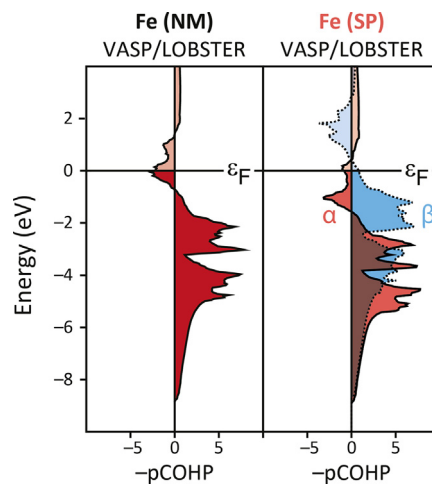


Fig. 40 Projected COHP analysis of Fe–Fe bonding in body-centered cubic iron, assuming no spin polarization (before spin unpairing) and with spin polarization (after spin unpairing) calculated using plane waves and the GGA. Reprinted from Maintz, S.; Deringer, V. L.; Tchougréff, A. L.; Dranskiowski, R., LOBSTER: A Tool to Extract Chemical Bonding From Plane-Wave Based DFT. *J. Comput. Chem.* **2016**, 37 (11), 1030–1035 with permission from John Wiley and Sons.

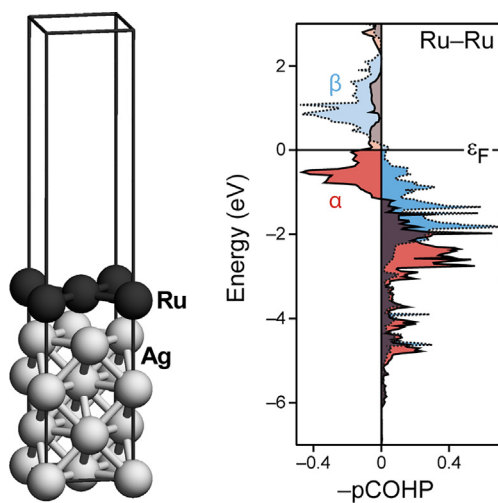


Fig. 41 Projected COHP analysis of Ru–Ru bonding in a monolayer of Ru on top of a face-centered cubic Ag(001) surface after spin polarization, modeled using plane waves and the GGA. Reprinted from Maintz, S.; Deringer, V. L.; Tchougréeff, A. L.; Dronskowski, R., LOBSTER: A Tool to Extract Chemical Bonding From Plane-Wave Based DFT. *J. Comput. Chem.* **2016**, 37 (11), 1030–1035 with permission from John Wiley and Sons.

does not intercalate in a comparable way, making alternatives like nanoporous graphite-type compounds necessary.^{238,241,243–246} In Fig. 42, crystal structures of LiC₆ and LiC₁₂ are depicted. Both compounds exhibit a layered structure and crystallize in space group P6/mmm (No. 191),²⁴⁷ the only structural difference being that LiC₁₂ only has half of Li layers of LiC₆. Theoretically, the compounds were structurally optimized using the meta-GGA functional SCAN (strongly constrained and appropriately normed semilocal density functional) as implemented in VASP.^[248,62]

It is no surprise that the Löwdin charge⁶¹ of Li (+0.83 e) in LiC₆ and LiC₁₂ is exactly the same for both compounds and the charge of C in LiC₆ (−0.14 e) is half the value in LiC₁₂ (−0.07 e). These constant Löwdin charges nicely mirror that there is only one symmetry-independent Li/C atom, both in LiC₆ and LiC₁₂. Because the Bader algorithm^{249–252} operates on the electron density in real space and a partitioning of the density in terms of its second derivative, tiny inaccuracies of the latter may lead to a small scatter of the atomic basins such that a Bader charge distribution is found for carbon in LiC₆ (−0.05 e to −0.23 e, average: −0.14 e) and LiC₁₂ (−0.02 e to −0.14 e, average: −0.07 e) with lithium having a charge of +0.86 e in both cases. While it has been impossible to directly calculate charges from plane waves in the past because of severe technical difficulties, indirectly deriving Bader charges from the real-space plane-wave density was the way to go. The relatively low speed of the latter is due to the resource-hungry all-electron calculations for the core charge densities as a prerequisite for Bader, and this is the numerical price paid for working with the density. Mulliken and Löwdin charges directly from the wave function are less time-consuming by around one order of magnitude.⁶¹

Charge analysis based on densities splendidly fails^{63,244} for another type of anode materials, carbonaceous nanoporous compounds.^{235,241,244} They are promising candidates to tackle problems with common anode materials, especially in case of Na.^{235,241,244} For example, negative Bader charges for some Na ions in a MD-simulated nanoporous compound with the composition of Na₁₄C₂₀₆ were found.²⁴⁴ This finding contradicts not only chemical intuition, but also experimental results like small-angle X-ray scattering data which indicates a formation of metallic or cationic Na species during the intercalation process.^{253,254} *Operando* solid-state NMR measurements on Li²⁵⁵ and Na²⁵⁶ also show that Li and Na species exhibit a metallic or cationic, but never anionic, character while moving in or out of the structure in the cycling process. Hence, reexamining the MD-simulated

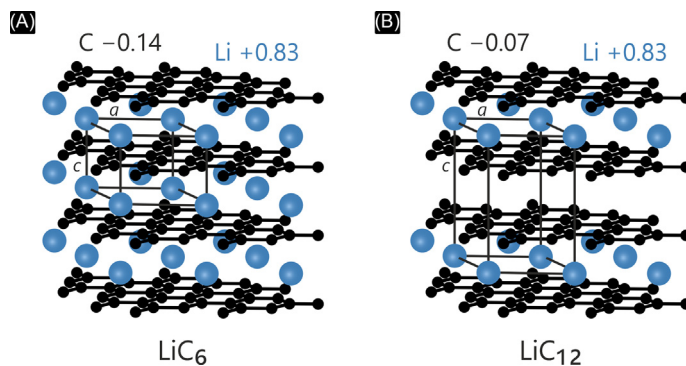


Fig. 42 The crystal structures of (A) LiC₆ and (B) LiC₁₂. The unit cell and the Li and C Löwdin charges are shown.

nano porous structure $\text{Li}_{48}\text{C}_{216}$ ^{63,241} with the Löwdin population analysis and the Bader charge analysis seems required (summarized in Fig. 43).

The Bader charges reveal that the Li ion in the pore center of the carbon backbone exhibits a (unreasonable) negative charge, while the Li ions surrounding the pore have a charge of almost +1 without any charge distribution. This finding contradicts the experimental results mentioned above. Löwdin's population analysis (Fig. 43A), on the other hand, makes it clear that the central Li ion exhibits a weakly cationic, almost metallic character and the surrounding ions show a nice charge distribution around the pore, with a constantly growing cationic character when moving from the center of the pore to the outer area of the simulation cell, in agreement with experimental findings.²⁵⁵ By using nanoporous carbonaceous materials, these result in partially reduced charges of the Li and Na ions, and one may expect that this property improves the materials' intercalation behavior as a consequence of weaker Coulomb attractions resulting from that.^[257,62]

3.07.3.6 Thermoelectrics and Zintl phases

As indicated by their name, thermoelectric materials exploit the thermoelectrical effect, in particular the Seebeck effect, in a convenient way to contribute to so-called "clean-energy" technologies. Zintl phases and, in general, intermetallic compounds, including polar intermetallics, are of special interest here and show potential use as thermoelectrics.^{140,258–261} Many Zintl phases, such as n-type Mg_3Sb_2 ,¹⁴⁰ allow for band engineering (e.g., band convergence for increasing band degeneracy). One crucial step in optimizing thermoelectric materials is to determine the bonding (or antibonding) character of a certain band in the entire band structure which can be accomplished by using a band-resolved projected COHP to identify the bonding tendency.¹⁴⁰ In the specific case of n-type Mg_3Sb_2 , the band degeneracy is improved by introducing more ionic cations to partially occupy octahedral Mg sites, accomplished by substitution of Mg by Yb, denoted as Yb_{Mg} . This mechanism is revealed by band-resolved pCOHP showing that the bonding character between adjacent Mg atoms in the octahedral (Mg_{octa}) and tetrahedral (Mg_{tetra}) sites (Fig. 44) is covalent and bonding when walking through reciprocal space.¹⁴⁰

As indicated by band-resolved pCOHP, this very bonding interaction between the adjacent Mg sites is the reason why the so-called conduction-band minimum (CBM) is located so low at the U^* point (cf. Fig. 44). Therefore, by substituting an "electropositive" atom, such as Yb, between Mg_{octa} and Mg_{tetra} the bonding covalency of the CBM bands will decrease and alter the band edge significantly, so that the band shape and band degeneracy at the CBM can be changed for benefits of the electrical transport properties of the thermoelectrics.¹⁴⁰ At least theoretically, $\text{Mg}_{2.75}\text{Yb}_{0.25}\text{Sb}_2$ exceeds Mg_3Sb_2 three times in terms of zT .

Tuning the ionicity of Zintl phases or other (polar) intermetallics to improve the material properties also requires the detailed knowledge of atomic charges. Non-quantum mechanical electron partitioning models like the Zintl-Klemm concept^{262–264} have already been established by assuming idealized ionic charges to rationalize the relationship between the crystal structure of a solid state material and its electron structure, especially the valence electron distribution. This procedure is reaching its limit with some

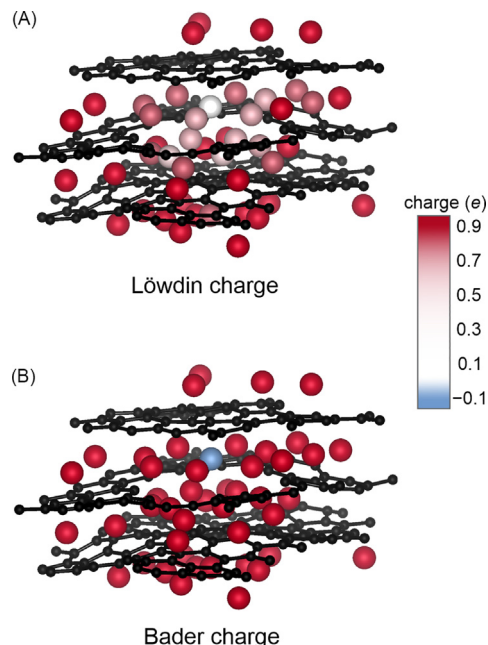


Fig. 43 (A) Löwdin charges and (B) Bader charges for the Li-rich nanoporous structure $\text{Li}_{48}\text{C}_{216}$. The figure only shows a section of the whole simulation cell²⁴¹ to focus on the atomic environment around the center pore. From Nelson, R.; Ertural, C.; George, J.; Deringer, V. L.; Hautier, G.; Dranskowski, R., LOBSTER: Local Orbital Projections, Atomic Charges, and Chemical-Bonding Analysis From Projector-Augmented-Wave-Based Density-Functional Theory. *J. Comput. Chem.* **2020**, *41* (21), 1931–1940.

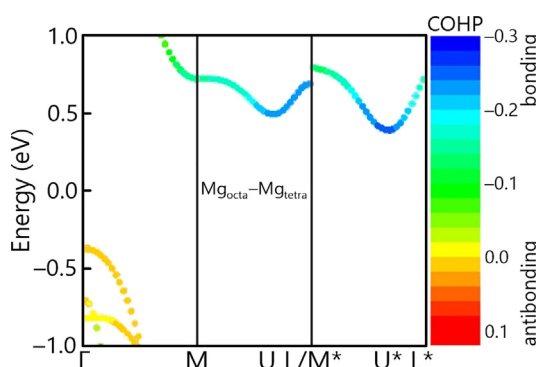
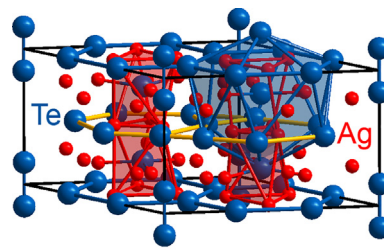


Fig. 44 Band-resolved projected COHP, obtained from LOBSTER, for the interaction between the different Mg sites (Mg_{octa} and Mg_{tetra}) showing nonbonding states at valence band maximum (VBM) and bonding states at conducting band minimum (CBM, U/U^*).¹⁴⁰ From Sun, X.; Li, X.; Yang, J.; Xi, J.; Nelson, R.; Ertural, C.; Dronskowski, R.; Liu, W.; Snyder, G. J.; Singh, D. J.; Zhang, W., Achieving Band Convergence by Tuning the Bonding Ionicity in n-type Mg_3Sb_2 . *J. Comput. Chem.* **2019**, *40* (18), 1693–1700.

intermetallic compounds containing low-dimensional fragments that lead to electron imprecise charges. Such an example is the mineral stützite $Ag_{5-x}Te_3$ ^{61,265} ($x = -0.25$ to $x = 1.44$). The crystal structure with space group $P\bar{6}2m$ (Fig. 45) is composed of Te dumbbells $[Te^-]_2$, as well as stacked honeycomb (h) and Kagome Te nets (K) in a $-h-K-h-K-$ sequence. The Ag atoms form different polyhedra and are distributed around the Te atoms.

Depending on the composition, stützite can barely be described as $(Ag^+)^{34}(Te^{2-})^{13}([Te^-]_2)_4$ and $(Ag^+)^{36}(Te^{2-})^{13}([Te^-]_2)_4(e^-)_2$ for silver-rich compositions such as “ $Ag_{34}Te_{21}$ ” and “ $Ag_{36}Te_{21}$ ”. The existence of a silver-poorer relative to the electron-precise $Ag_{34}Te_{21}$ ($= Ag_{4.86}Te_3$) phase is known,^{266–268} however, so the question of how to describe the valence electron distribution in electron poorer intermetallics rises. Another detail that disapproves the Zintl-Klemm usability or other simple electron counting rules, is that the difference between absolute electronegativities²⁶⁹ of silver (4.44 eV) and tellurium (5.49 eV) is rather small. To overcome oversimplification of this kind of electron counting rules, quantum mechanically derived charges like those of Mulliken or Löwdin can come to our rescue and reveal the (albeit not very) ionic nature of stützite. When analyzing three stützite models with varying silver content ($Ag_{32}Te_{21}$, $Ag_{34}Te_{21}$, $Ag_{36}Te_{21}$), all from within the homogeneity range, phonon calculations indicate dynamic stability throughout, and DOS and COHP data also show only subtle (albeit significant) differences between the three models, favoring the Zintl-Klemm precise $Ag_{34}Te_{21}$ model as most metastable.²⁶⁵ Analyzing the electronic structure of stützite with Mulliken's population analysis yields $(Ag^{+0.37})^{32}(Te^{-0.66})^{13}([Te^{-0.40}]_2)_4$ for the structure model “ $Ag_{32}Te_{21}$ ”, $(Ag^{+0.36})^{34}(Te^{-0.68})^{13}([Te^{-0.36}]_2)_4$ for “ $Ag_{34}Te_{21}$ ”, and $(Ag^{+0.33})^{36}(Te^{-0.64})^{13}([Te^{-0.42}]_2)_4$ for “ $Ag_{36}Te_{21}$ ” (averaged charges since the crystal structure is disordered), so the expected charge transfer from Ag to Te can be clearly observed. In terms of the Zintl-Klemm concept, the Te atoms with lesser charge play the role of X halogen atoms and form X_2 dumbbells, while the other Te atoms resemble noble gas atoms and stay structurally rather isolated. Even if the average charge does not change much with the different composition models for stützite, automatic Madelung energies ϵ_M calculated based on the Mulliken charges from LOBSTER¹⁴⁴ give more insight into the stability tendency depending on the composition.

Including the formation enthalpy ΔH_f derived from total energies^{26,61,116} into the analysis (Table 1), the Ag-richest composition “ $Ag_{36}Te_{21}$ ” exhibits the lowest stability, followed by the Ag-poorest composition “ $Ag_{32}Te_{21}$ ”. Among the three compositions, only the Zintl-Klemm electron precise composition “ $Ag_{34}Te_{21}$ ” is the most stable one and therefore the “optimum” composition,⁶¹ agreeing with recent research.²⁶⁵ So the Madelung energy nicely mirrors the total energies and formation enthalpies, which is quite surprising given the fact that Ag and Te have similar absolute electronegativities (as mentioned before). Despite the subtle charge



$Ag_{5-x}Te_3$

Fig. 45 Crystal structure of stützite. Kagome Te nets are highlighted in yellow. Reproduced with permission from Ertural, C.; Steinberg, S.; Dronskowski, R., Development of a Robust Tool to Extract Mulliken and Löwdin Charges From Plane Waves and Its Application to Solid-State Materials. *RSC Adv.* **2019**, *9* (51), 29821–29830 – Published by The Royal Society of Chemistry.

Table 1 Formation enthalpy ΔH_f and Madelung energy ε_M (per unit cell) for the three stützite model compositions.

Compound	ΔH_f (kJ · mol ⁻¹) ⁶¹	ε_M (kJ · mol ⁻¹)
"Ag ₃₂ Te ₂₁ "	-275.8	-4140
"Ag ₃₄ Te ₂₁ "	-301.0	-4292
"Ag ₃₆ Te ₂₁ "	-221.4	-3803

differences for the three simulation models for stützite, the Madelung energy acts as a tool that straightforwardly provides new insight into the trend of the stability and complexity of the structure of this intermetallic compound.

3.07.3.7 Materials mapping

What theorists usually call "mapping" of materials is a useful way to classify materials according to their bonding (and other) properties. It all started with the triangle by Van Arkel and Ketelaar^{1,2,270} (see introductory Section 3.07.1.1) who plotted a descriptor of covalency, namely the average electronegativity, against an ionic descriptor, namely the difference in electronegativities. This way, one easily and naturally separates materials from each other, based on their chemical bonding properties. Once the *microscopic* concept of bonding is understood, one may explain and even predict certain *macroscopic* properties like reactivity and stability, similar to organic chemists synthesizing target molecules.²⁷¹ In the field of solid-state chemistry, there has been some effort to categorize functional materials such as phase-change materials (see Section 3.07.3.3) and thermoelectrics (see Section 3.07.3.6) to be found in characteristic places of material maps. On the basis of these maps, new synthetic targets of promising functional materials may be identified via purely computational means. In previous works, maps were set up by descriptors for different concurring bonding mechanisms such as a covalent descriptor and an ionicity descriptor. For covalency, orbital mixing, orbital occupations, shared electrons, and effective coordination numbers are possible descriptors while for ionicity, a charge transfer is often used by either real-space partitioning of electron density or a wave-function based approach.^{166,168,172,272}

The material map in Fig. 46 places the functional materials such as GeTe and multiple compounds of the pseudo binary GeTe-Sb₂Te₃ system in a region of weak ionicity and medium sp³ mixing. The compounds inside the triangle between GeTe, GeSb₄Te₇ and Ge₂Sb₂Te₅ were identified as potential candidates of phase change materials as they show a similar bonding because the separation from non-phase change active materials is clear. Oxides, sulfides and selenides are separated by the ionicity scale while the covalency axis leads to a separation of compounds like elemental phosphorus from the functional materials.

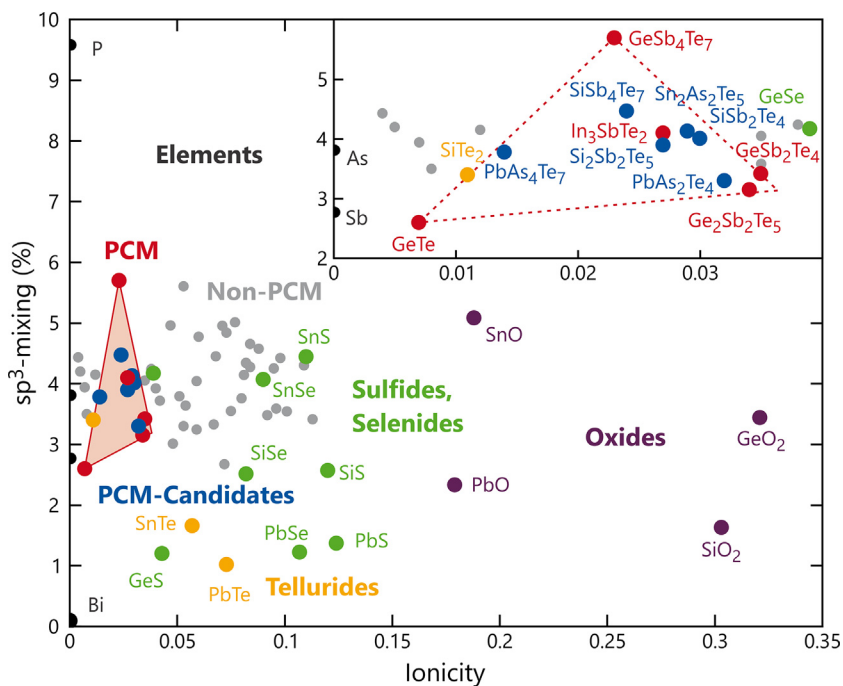


Fig. 46 Material map using the fraction of sp³ mixing and the heuristic ionicity as indicators for covalent and ionic bonding in the search for promising candidates of phase change materials (PCM). Inlay: Enlarged material map for the region of industrially used and potential candidate PCM. Figure produced reusing data from reference.²⁸⁸

As alternative bonding indicators, the descriptors introduced in [Section 3.07.2.10](#), namely $\overline{\text{ICOHP}}$, effective interaction number and a revised definition of the ionicity, provide a similar identification of materials.¹⁶⁰

The prototypical material map in [Fig. 47](#) uses the integrated averaged crystal orbital Hamilton population ($\overline{\text{ICOHP}}$) as a measure of covalency and the ionicity derived from Löwdin charges to characterize the chemical bonding properties. To no surprise, the elemental phases copper, diamond and graphite possess no ionic contributions, while zincblende, rock salt and cesium chloride show a significant charge transfer which grows with the coordination number. The course of covalency is just as expected: The ionic compounds have negligible covalent properties due to strong ionic forces. Metals such as copper appear as covalent materials but with a strong electron deficit, compensated by the formation of electron bands to distribute the few valence electrons over a large number of atoms, leading to weak metal-metal interactions.^{273,274} The more covalent a material is, the larger is the achieved $\overline{\text{ICOHP}}$. Consequently, the carbon allotropes occupy regions in the top left corner of the material map in [Fig. 47](#) with graphite being more covalent, which is due to the π -system that results in a higher bond order.

As this proof of concept evidences the applicability of the $\overline{\text{ICOHP}}$ and ionicity for modelling the chemical bonding behavior in solid-state materials, let us consider a larger variety of compounds. The map in [Fig. 48](#) uses the same descriptors as above.

Extreme values of bonding mechanisms are found—as expected—for the covalent carbon allotropes diamond and graphite with $\overline{\text{ICOHP}}$ of -9.4 eV and -10.8 eV, respectively, and no ionicity. In the case of ionic compounds, the fluorides of cesium, calcium and potassium have the largest values of ionicity which are 87%, 82%, and 81%, respectively. Covalency does not play any role in these compounds, judging from the $\overline{\text{ICOHP}}$ of -0.4 eV, -0.5 eV, and -0.4 eV, respectively. For a fixed cation, the ionicity decreases when going to higher periods for the anion. As such, the value for ZnO is largest for the chalcogenides of zinc and decreases from 69% to 62% for ZnS, 60% for ZnSe, and 55% for ZnTe. Metals such as copper are generally found in regions with small covalency and small ionicity. When covalency increases, we reach the region of semiconductors with small ionicity and moderate covalency. Here, there are phase-change materials such as GeTe, $\text{Ge}_2\text{Sb}_2\text{Te}_5$, and Sb_2Te_3 with $\overline{\text{ICOHP}}$ between -1 eV and -3 eV and ionicities between 0% and 10%. Non-phase changing semiconductors such as silicon, germanium, and GaAs have stronger covalent interactions with $\overline{\text{ICOHP}}$ between -3 eV and -4 eV. Interestingly, there are certain examples of materials with both covalent and ionic interactions, for example OsO_4 , SiO_2 , and GeO_2 , for which a significant charge transfer is indicated by ionicities between 35% and 50% while the covalency is relatively large with $\overline{\text{ICOHP}}$ between -6.5 eV and -8.0 eV.

Despite its successful identification of certain bonding properties, the $\overline{\text{ICOHP}}$ does not clearly separate between phase-change materials on the one side and metals on the other side as both classes feature similar bonding properties: weak to moderate covalency and weak to no ionicity. In order to highlight this difference, the effective interaction number as introduced in [section 3.07.2.10.1](#) can also be used to integrate a structural component into the picture of chemical bonding analysis. The corresponding materials map is shown in [Fig. 49](#).

[Fig. 49](#) easily allows to separate the functional materials from both classical semiconductors as well as metals because they have effective interaction numbers between 6.5 and 8.0. An intermetallic NiAl and elemental copper locate in areas with very high EIN, as expected for metals featuring significant long-ranged interactions. On the other side of the scale, we find covalent materials like carbon in the diamond and graphite allotropes. In the same region, classical semiconductors such as silicon (both crystalline and amorphous) are found next to the amorphous phases of phase-change materials GeTe as well as $\text{Ge}_2\text{Sb}_2\text{Te}_5$. The latter is quite

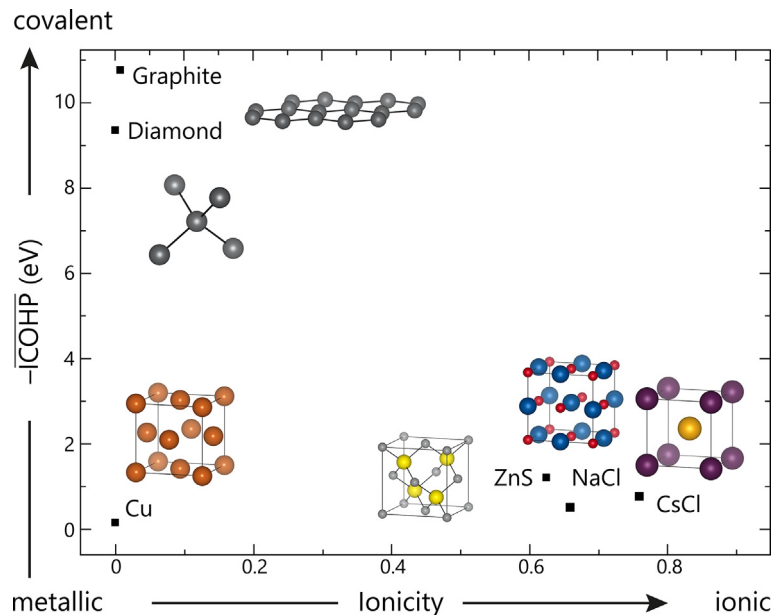


Fig. 47 Prototype of a material map using the weighted average $\overline{\text{ICOHP}}$ and the ionicity from Löwdin charges.

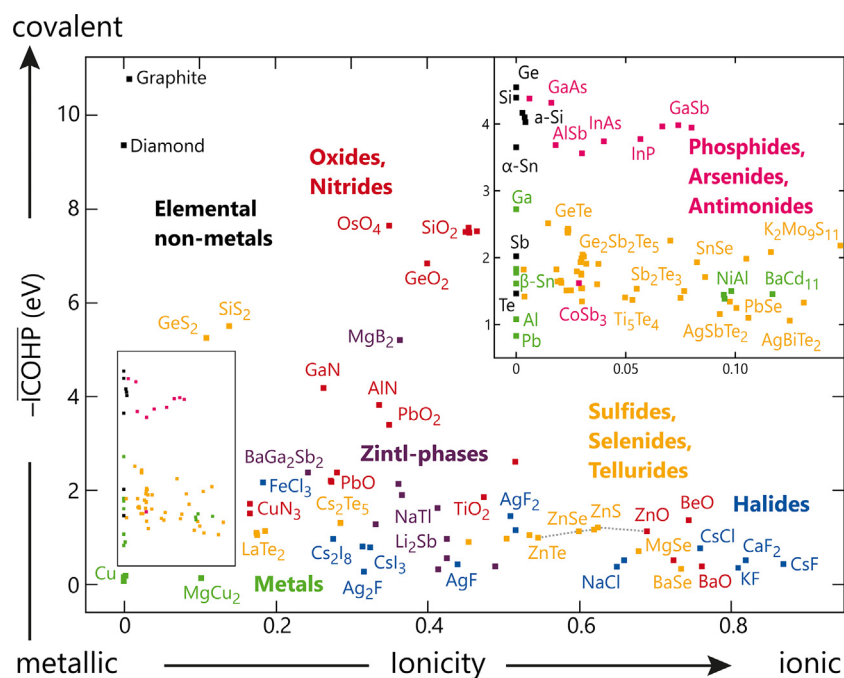


Fig. 48 Material map based on the weighted average ICOHP and the ionicity derived from Löwdin charges. The area between $-0.5 \text{ eV} \leq \text{ICOHP} \leq -5 \text{ eV}$ and $0 \leq \text{ionicity} \leq 0.15$ is shown separately in the inlay.

interesting as these materials differ significantly in their macroscopic properties, compared to the crystalline phases, while Si shows only small differences in both optical properties and EIN between both phases.²⁷⁵ As the effective interaction number simultaneously measures bonding and structure, the origin of the interesting properties of phase change as well as thermoelectric materials are found in only this bonding-structure relationship.

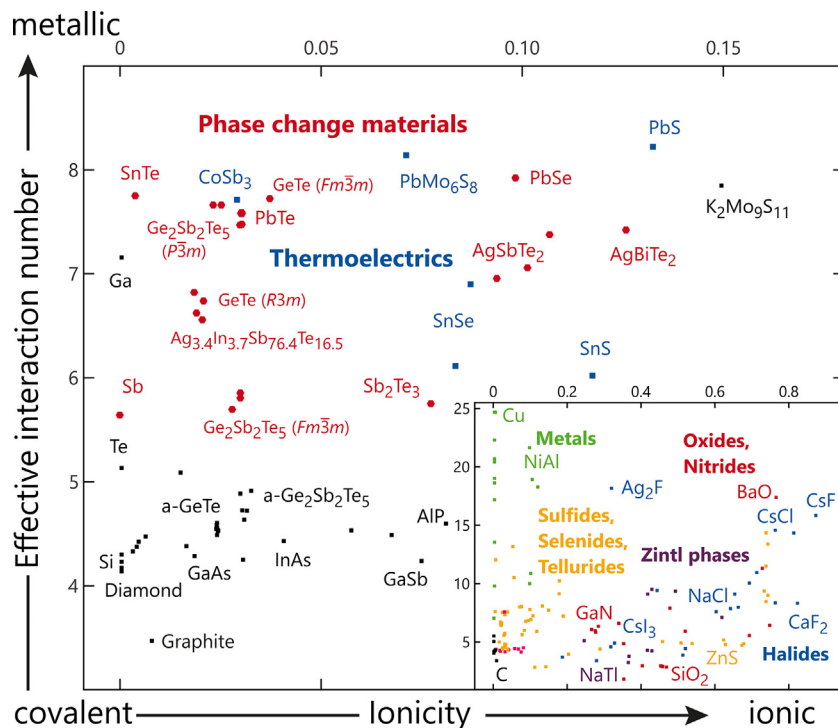


Fig. 49 Material map based on effective interaction number and ionicity from Löwdin charges for the area of functional phase change and thermoelectric materials. Inlay: The same map but for the whole range of examined compounds.

3.07.3.8 Interplay of bonding and structure

The interesting behavior of phase-change materials such as GeTe seemingly originates from both bonding as well as peculiar structure. Their large effective interaction numbers indicate bonding interactions that go beyond the first coordination sphere, and the proposed bonding mechanisms range from “resonant” bonding over a new, albeit vaguely defined, “metavalent” to a multicenter bonding mechanism featuring lone pairs. All of these are supposed to explain the unexpected property portfolio of said functional materials.^{166,167,169,170,275–278} Let us now look into these bonding properties from a local-orbital perspective by the means of pCOHP and COBI. Our example will be cubic GeTe which crystallizes in the rock-salt structure. By combining elements from the fourth and sixth main group, an interesting bonding situation arises as the 8–N rule is violated, as alluded to in [Section 3.07.2.3](#). The electron surplus and its energetic penalty is relieved by either a Peierls distortion into a rhombohedral phase or the formation of Ge vacancies.^{213,217,279,280} A consequence of the increased valence electron count is an unexpectedly strong Te–Te interaction mediated by an in-between germanium atom.^{160,281}

[Fig. 50A](#) shows the projected crystal orbital Hamilton population for the Ge–Te bond in the rock-salt β -phase of GeTe as well as the closest and second closest Te–Te contacts. Unsurprisingly, the Ge–Te bond is the strongest interaction present in the unit cell. For the Te–Te contacts, the expectation is not met, though. The closest Te–Te with $d = 4.17 \text{ \AA}$ exhibits an IpCOHP of +0.01 eV, in harmony with this distance being well beyond the sum of their covalent and ionic radii.^{282,283} The second closest Te–Te contact, however, does not fit the expected course. Despite $d = 5.90 \text{ \AA}$, the interaction is slightly *bonding* with –0.13 eV. In order to find the origin of this unexpected long-ranged bonding, a *gedankenexperiment* may be appropriate. By removing the Ge atom directly located *between* the bonding Te atoms, the bond can be completely eliminated. Not only is the IpCOHP = –0.002 eV extremely small, the course of the pCOHP in [Fig. 50B](#) resembles noise rather than a distinct curve. At the same time, the Te–Te contact that is mediated by a Ge atom is magnitudes larger in both pCOHP and IpCOHP. We can thus conclude that the presence of a Ge atom between two Te atoms is somehow responsible for the existence of a Te–Te contact.

Is the bond-mediating influence confined to a Ge atom or will other atoms do as well? To answer this question, [Fig. 51](#) shows the effect of substituting the Ge site by a Ca atom and doing the reverse experiment by inserting a Ge atom in a structure of CaTe. Since both phases possess the same structure type, a comparison can easily be done. Electronically, germanium and calcium only differ in their valence electron count by two, so CaTe follows the 8–N rule while GeTe does not. Consequently, the existence of a hyperbonding interaction is not likely in CaTe. Indeed, the pCOHP as well as the IpCOHP are negligibly small for the Te–Te_{Ca} interaction; note that the Ca subscript refers to the Ca atom mediating the Te–Ca–Te contact. Qualitatively, this observation is independent of the surrounding environment: In a GeTe structure in which one Ge position is replaced by a Ca atom (see [Fig. 51A](#)), the Ge-mediated Te–Te interaction has the same IpCOHP value of –0.13 eV whereas the ICOHP of the Ca-mediated Te–Te contact is weak (IpCOHP = –0.02 eV). In the opposite case, as depicted in [Fig. 51B](#), the Te–Te_{Ge} bond is still stronger than the Te–Te_{Ca} bond with IpCOHP equal to –0.09 eV and –0.01 eV, respectively. The difference between the examples in [Fig. 51A](#) and B is mainly quantitative between the pCOHP which is more discrete in the CaTe case, and a smaller IpCOHP for both examined Te–Te interactions. Both observations can be explained by CaTe’s stronger ionicity. The strong localization of electrons on the atoms leads to flat bands

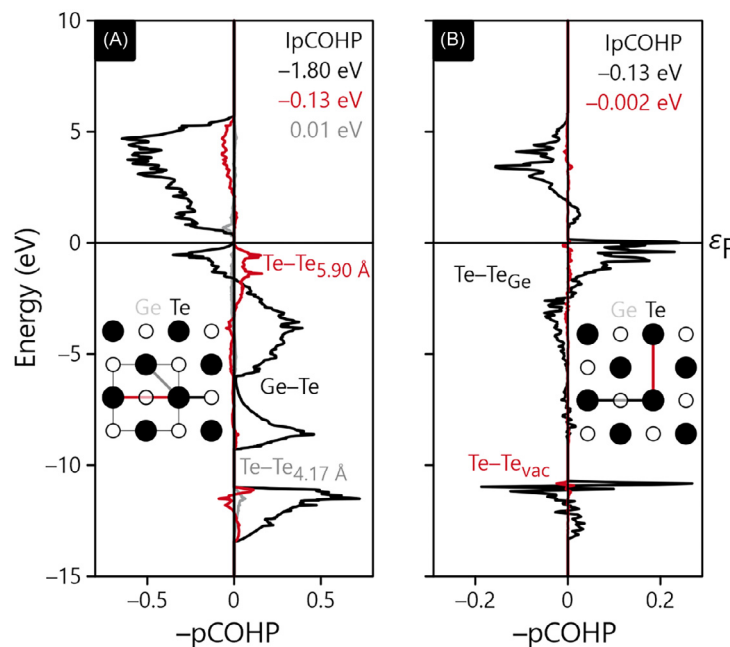


Fig. 50 Projected crystal orbital Hamilton population of (A) pure GeTe in rock-salt structure for the shortest Ge–Te bond, the shortest Te–Te contact, and the Te–Te bond over one Ge atom. (B) GeTe with a Ge-vacancy for the Te–Te contact over the Ge-vacancy and one Ge atom.

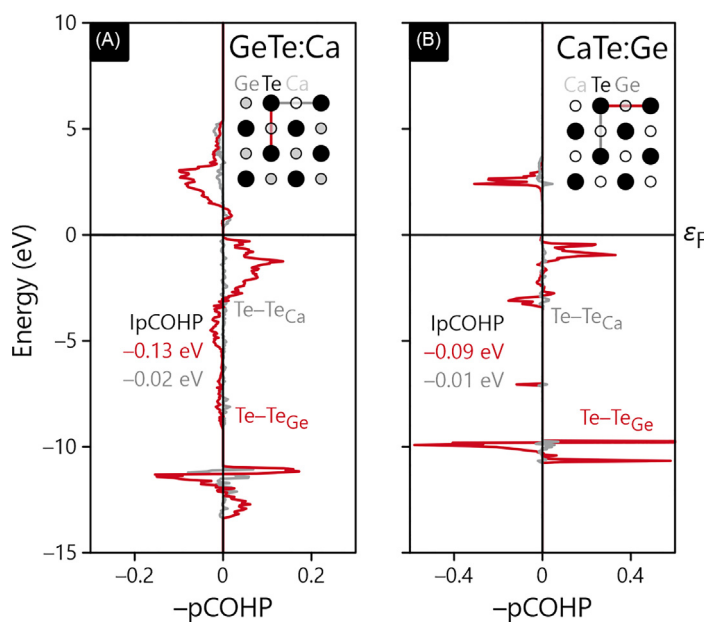


Fig. 51 Crystal orbital Hamilton population for the Te–Te bond over a Ge atom as well as a Ca atom in (A) Ca-substituted GeTe and (B) Ge-substituted CaTe.

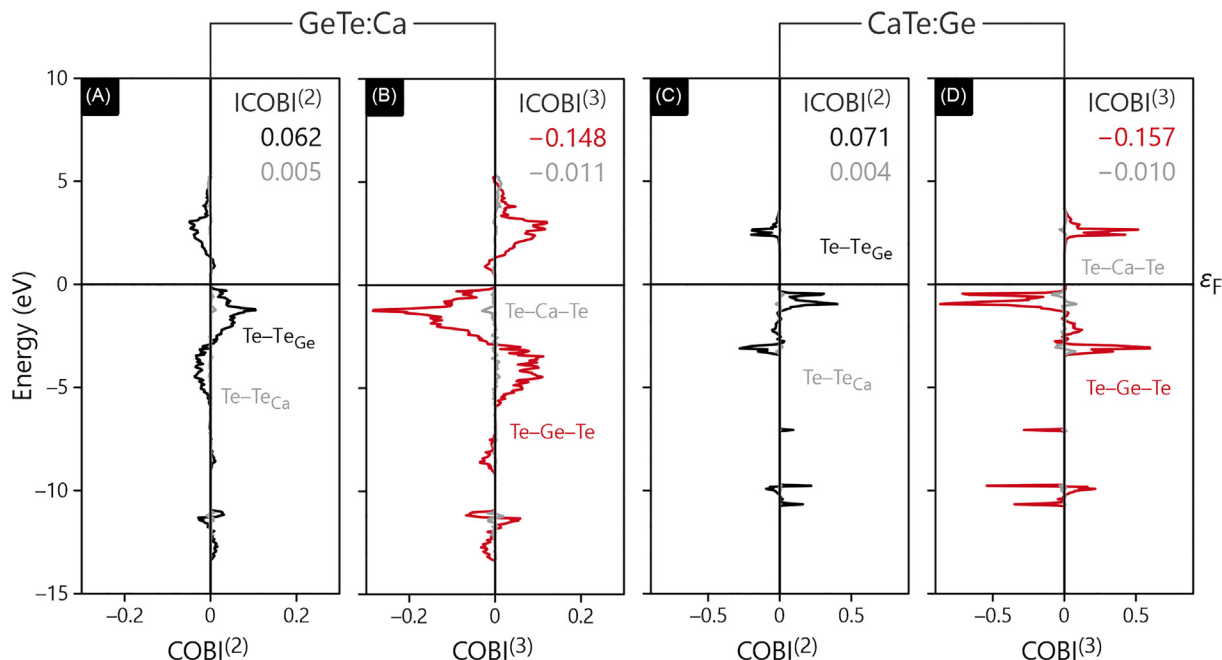


Fig. 52 (A) Two-center COBI for the Te–Te contacts mediated by germanium and calcium in Ca-substituted GeTe. (B) Three-center COBI for the Te–Ge–Te and the Te–Ca–Te interaction in Ca-substituted GeTe. (C) Two-center COBI for the Te–Te contacts mediated by germanium and calcium in Ge-substituted CaTe. (D) Three-center COBI for the Te–Ge–Te and the Te–Ca–Te interaction in Ge-substituted CaTe.

and discrete energy levels. At the same time, the covalent interactions decrease which then leads to a weakened Te–Ge–Te multicenter bond.

While pCOHP is useful for chemical bonding, its application to multicenter bonding is limited as it only resolves two-center interactions. An improved analysis of the bonding situation is possible via the crystal orbital bond index (COBI) that can be formed over (theoretically) any number of atoms. The two-center COBI⁽²⁾ as well as the three-center COBI⁽³⁾ are shown in Fig. 52 for the exact same setup that was used for the pCOHP in Fig. 51.

The two-center COBI in Fig. 52A and C are very similar to the pCOHP in Fig. 51 as, the Ge-mediated Te–Te interaction is significantly stronger than the Ca-mediated Te–Te contact. This result comes to no surprise since both bonding indicators are similarly defined and quantify the same kind of interaction: covalent bonding. The COBI⁽³⁾ in Fig. 52B and D, on the other side, allow for a deeper insight. Analogous to the two-center COBI⁽²⁾, the Te–Ge–Te interaction is significantly stronger than the Te–Ca–Te interaction. The latter kind of interaction would be very surprising in a primarily ionic compound like CaTe that—again—follows the 8–N rule. In GeTe, the total number of valence electrons exceeds the octet such as to enable a hyperbonding mechanism well-known in the molecular realm, say in XeF₂ or SF₆. We note, however, that such behavior was also proposed for solid-state materials in which the range of these interactions can be much larger due to translational invariance.^{169,170,284}

3.07.4 Computational details

Figs. 7, 9, 10, 14, 15B and C, 16, 17, 18, 19, 20, 21, 23, 24, 27, 28C, 29B, 30, 31, 32, 35, 36, 37, 40, 41; Figs. 42, 43, 44, 45, 46, 47, 48, 49, 50, 51, 52 were produced based on data calculated using the Vienna Ab initio Simulation Package (VASP). Fig. 13 is based on calculations using ABINIT. The program Local Orbital Basis Suite Towards Electronic-Structure Reconstruction (LOBSTER) was also utilized to produce Figs. 7, 9, 10, 13, 14, 15B and C, 16, 17, 18, 19, 20, 21, 23, 24, 27, 28C, 29B, 30, 32, 35, 36, 37, 40, 41, 42, 43, 44, 46, 47, 48, 49, 50, 51, 52. Orbital shapes in Fig. 3 are qualitatively based on a Hartree-Fock GAMESS²⁸⁵ calculation. Fig. 8 is based on a YAeHMOP²⁸⁶ calculation. The detailed setups of individual calculations and references of all computer programs are given in the main text and in the referenced literature.

Acknowledgments

We thank the decent taxpayers of the state NRW for having provided basic funding over many years. In addition, we thank DFG, the Alexander von Humboldt foundation, the Hoffmann Institute, and VolkswagenStiftung for third-party money.

References

1. Arkel, A. E. V. *Molecules and Crystals in Inorganic Chemistry*, 2nd edn; Butterworth: London, 1956.
2. Ketelaar, J. A. A. *Chemical Constitution: An Introduction to the Theory of the Chemical Bond*, 2nd rev. edn; Elsevier: Amsterdam, 1958.
3. Pauling, L. *The Nature of the Chemical Bond*, Cornell University Press: Ithaca, New York, 1960.
4. Parr, R. G.; Pearson, R. G. Absolute hardness: companion parameter to absolute electronegativity. *J. Am. Chem. Soc.* **1983**, *105* (26), 7512–7516.
5. London, F. Zur Theorie und Systematik der Molekularkräfte. *Z. Physik* **1930**, *63*, 245–279.
6. Waals, J. D. V. D. *Over de Continuiteit van den Gas- en Vloeistofstaand*. Dissertation, University of Leiden, 1873.
7. Parsegian Van der, A. *Waals Force: A Handbook for Biologists, Chemists, Engineers, and Physicists*, Cambridge University Press: New York, 2006.
8. Pimentel, G. C.; McClellan, A. L. *The Hydrogen Bond*, W. H. Freeman: San Francisco, 1960.
9. Jeffrey, G. A. *An Introduction to Hydrogen Bonding*, Oxford University Press: Oxford, 1997.
10. Schrödinger, E. Quantisierung als Eigenwertproblem. *Ann. Phys.* **1926**, *384* (4), 361–376.
11. Pauling, L.; Wilson, E. B. *Introduction to Quantum Mechanics With Applications to Chemistry*, Courier Corporation, 2012.
12. Szabo, A.; Ostlund, N. S. *Modern Quantum Chemistry—Introduction to Advanced Electronic Structure Theory*, Dover Publications, Inc.: Mineola, NY, 1996.
13. Bishop, D. M. *Group Theory and Chemistry*, Courier Corporation, 1993.
14. Burdett, J. K. From bonds to bands and molecules to solids. *Prog. Solid State Chem.* **1984**, *15* (3), 173–255.
15. Heitler, W.; London, F. Wechselwirkung neutraler Atome und homöopolare Bindung nach der Quantenmechanik. *Z. Phys.* **1927**, *44*, 455–472.
16. Pauling, L. The nature of the chemical bond. Application of results obtained from the quantum mechanics and from a theory of paramagnetic susceptibility to the structure of molecules. *J. Am. Chem. Soc.* **1931**, *53* (4), 1367–1400.
17. Schrödinger, E. Quantisierung als Eigenwertproblem. *Ann. Phys.* **1926**, *79*.
18. Heisenberg, W. Über quantentheoretische Umdeutung kinematischer und mechanischer Beziehungen. *Zeitschrift für Physik* **1925**, *33*, 15.
19. Stark, J. Beobachtungen über den Effekt des elektrischen Feldes auf Spektrallinien. V. Feinzerlegung der Wasserstoffserie. *Ann. Phys.* **1915**, *48*.
20. Born, M. J.; Oppenheimer, R. Zur Quantentheorie der Moleküle. *Ann. Phys.* **1927**, *389*.
21. Pauli, W. Über den Zusammenhang des Abschlusses der Elektronengruppen im Atom mit der Komplexstruktur der Spektren. *Zeitschrift für Physik* **1925**, *31*, 765–783.
22. Hartree, D. R. The Wave Mechanics of an Atom with a Non-Coulomb Central Field. *Proc. R. Soc. Lond.* **1928**, *A113*.
23. Slater, J. The Theory of Complex Spectra. *Phys. Rev.* **1929**, *34*.
24. Fock, V. Näherungsmethode zur Lösung des quantenmechanischen Mehrkörperproblems. *Zeitschrift für Physik* **1930**, *61*, 126–148.
25. Roothaan, C. C. J. New Developments in Molecular Orbital Theory. *Rev. Mod. Phys.* **1951**, *23*.
26. Dronkowski, R. *Computational Chemistry of Solid State Materials: A Guide for Materials Scientists, Chemists, Physicists and Others*, Wiley-VCH: Weinheim, 2005.
27. Hehre, W. J.; Radom, L.; Schleyer, P. V., et al. *Ab Initio Molecular Orbital Theory*, John Wiley: New York, 1986.
28. Möller, C.; Plesset, M. S. Note on an Approximation Treatment for Many-Electron Systems. *Phys. Ther. Rev.* **1934**, *46*.
29. Jensen, F. *Introduction to Computational Chemistry*, Wiley: New York, 1999.
30. Hohenberg, P.; Kohn, W. Inhomogeneous Electron Gas. *Phys. Ther. Rev.* **1964**, *136*.
31. Martin, R. M. *Electronic Structure: Basic Theory and Practical Methods*, Cambridge University Press: Cambridge, 2004.
32. Kohn, W.; Sham, L. J. Self-Consistent Equations Including Exchange and Correlation Effects. *Phys. Rev.* **1965**, *140* (4A), A1133–A1138.
33. Dirac, P. A. M. Note on Exchange Phenomena in the Thomas Atom. *Math. Proc. Camb. Philos. Soc.* **1930**, *26* (3), 376–385.
34. Ceperley, D. M.; Alder, B. J. Ground State of the Electron Gas by a Stochastic Method. *Phys. Rev. Lett.* **1980**, *45* (7), 566–569.
35. Gunnarsson, O.; Jonson, M.; Lundqvist, B. I. Exchange and Correlation in Inhomogeneous Electron Systems. *Solid State Commun.* **1977**, *24* (11), 765–768.

36. Gunnarsson, O.; Lundqvist, B. I. Exchange and Correlation in Atoms, Molecules, and Solids by the Spin-Density-Functional Formalism. *Physical Review B* **1976**, *13* (10), 4274–4298.
37. Ziegler, T.; Rauk, A.; Baerends, E. J. On the calculation of multiplet energies by the Hartree-Fock-Slater method. *Theor. Chim. Acta* **1977**, *43* (3), 261–271.
38. Burke, K.; Perdew, J. P.; Ernzerhof, M. Why semilocal functionals work: Accuracy of the on-top pair density and importance of system averaging. *J. Chem. Phys.* **1998**, *109* (10), 3760–3771.
39. Emerich, D. W.; Burris, R. H. Complementary functioning of the component proteins of nitrogenase from several bacteria. *J. Bacteriol.* **1978**, *134* (3), 936–943.
40. Noodleman, L.; Lovell, T.; Liu, T.; Himo, F.; Torres, R. A. Insights into properties and energetics of iron–sulfur proteins from simple clusters to nitrogenase. *Curr. Opin. Chem. Biol.* **2002**, *6* (2), 259–273.
41. Pühler, A. Die Molekularbiologie der Stickstofffixierung bei Klebsiella pneumoniae. *Biologie in unserer Zeit* **1979**, *9* (1), 14–23.
42. Haghghi Mood, K.; Lüchow, A. Full Wave Function Optimization With Quantum Monte Carlo and Its Effect on the Dissociation Energy of FeS. *Chem. A Eur. J.* **2017**, *121* (32), 6165–6171.
43. Zitzlau, C. *Quantum Monte Carlo-based Full Wave Function Optimization for Transition Metal Compounds*. Master Thesis, RWTH Aachen, 2017.
44. Zhai, H.-J.; Kiran, B.; Wang, L.-S. Electronic and Structural Evolution of Monoiron Sulfur Clusters, FeS_n^- and FeS ($n = 1 – 6$), From Anion Photoelectron Spectroscopy. *Chem. A Eur. J.* **2003**, *107* (16), 2821–2828.
45. Roothaan, C. C. J. New Developments in Molecular Orbital Theory. *Rev. Mod. Phys.* **1951**, *23*, 69–89.
46. Bloch, F. Über die Quantenmechanik der Elektronen in Kristallgittern. *Z. Phys.* **1929**, *50*, 555–600.
47. Slater, J. C.; Koster, G. F. Simplified LCAO Method for the Periodic Potential Problem. *Phys. Rev.* **1954**, *94* (6), 1498.
48. Kohanoff, J. *Electronic Structure Calculations for Solids and Molecules: Theory and Computational Methods*, Cambridge University Press, 2006.
49. Kittel, C.; McEuen, P.; McEuen, P. *Introduction to Solid State Physics*; vol. 8; Wiley: New York, 1996.
50. Bullett, D. W. The Renaissance and Quantitative Development of the Tight-Binding Method. In *Solid State Physics*; Ehrenreich, H., Seitz, F., Turnbull, D., Eds.; vol. 35; Academic Press, 1980; pp 129–214.
51. Hoffmann, R. *Solids and Surfaces: A Chemist's View of Bonding in Extended Structures*, Wiley-VCH: Weinheim, NY, 1988.
52. Peierls, R. E. *Quantum Theory of Solids*, Oxford University Press: Oxford, 1955.
53. Jahn, H. A.; Teller, E. Stability of Polyatomic Molecules in Degenerate Electronic States. I. Orbital Degeneracy. *Proc. Roy. Soc. Lond. A* **1937**, *161*.
54. Burdett, J. K. *Chemical Bonding in Solids*, Oxford University Press: Oxford, 1995.
55. Burdett, J. K. *Chemical Bonds—A Dialog*, Wiley: New York, 1997.
56. Decker, A.; Landrum, G. A.; Dronskowski, R. Structural and Electronic Peierls Distortions in the Elements (A): The Crystal Structure of Tellurium. *Z. Anorg. Allg. Chemie* **2002**, *628* (1), 295–302.
57. Roller, D. E.; Roller, D. H. D. B. *The Development of the Concept of Electric Charge: Electricity From the Greeks to Coulomb*, Harvard University Press, 1954.
58. Mulliken, R. S. Electronic Population Analysis on LCAO-MO Molecular Wave Functions. I. *J. Chem. Phys.* **1955**, *23*, 1833–1840.
59. Löwdin, P. O. On the Non-Orthogonality Problem Connected With the Use of Atomic Wave Functions in the Theory of Molecules and Crystals. *J. Chem. Phys.* **1950**, *18*, 365–375.
60. Piela, L. *Ideas of Quantum Chemistry (Appendix J)*, 1st edn; Elsevier B.V.: Amsterdam, 2007.
61. Ertural, C.; Steinberg, S.; Dronskowski, R. Development of a Robust Tool to Extract Mulliken and Löwdin Charges From Plane Waves and Its Application to Solid-State Materials. *RSC Adv.* **2019**, *9* (51), 29821–29830.
62. Ertural, C.; Stoffel, R. P.; Müller, P. C.; Vogt, C. A.; Dronskowski, R. First-Principles Plane-Wave-Based Exploration of Cathode and Anode Materials for Li- and Na-Ion Batteries Involving Complex Nitrogen-Based Anions. *Chem. Mater.* **2022**, *34*, 652–668.
63. Nelson, R.; Ertural, C.; George, J.; Deringer, V. L.; Hautier, G.; Dronskowski, R. LOBSTER: Local Orbital Projections, Atomic Charges, and Chemical-Bonding Analysis From Projector-Augmented-Wave-Based Density-Functional Theory. *J. Comput. Chem.* **2020**, *41* (21), 1931–1940.
64. Steinberg, S.; Dronskowski, R. The Crystal Orbital Hamilton Population (COHP) Method as a Tool to Visualize and Analyze Chemical Bonding in Intermetallic Compounds. *Crystals* **2018**, *8*, 225.
65. Bader, R. F. W. *Atoms in Molecules: A Quantum Theory*, Oxford University Press: Oxford, 1994.
66. Bader, R. F. W. A Quantum Theory of Molecular Structure and Its Applications. *Chem. Rev.* **1991**, *91*, 893–928.
67. Ladd, M. F. C.; Lee, W. H. Lattice Energies and Related Topics. *Prog. Solid State Chem.* **1964**, *1*, 37–82.
68. Ladd, M. F. C.; Lee, W. H. Lattice Energies and Related Topics. *Prog. Solid State Chem.* **1965**, *2*, 378–413.
69. Jenkins, H.; Pratt, K. Convergence of the Bertaut Series and the Calculation of the Electrostatic Energy of an Extended Crystalline Lattice. *Chem. Phys. Lett.* **1979**, *62* (3), 416–420.
70. Jenkins, H. D. B. Calculation of Lattice Energy, Some Problems and Some Solutions. *Rev. Chim. Minér.* **1979**, *16*, 134–150.
71. Ewald, P. P. Die Berechnung optischer und elektrostatischer Gitterpotentiale. *Ann. Phys.* **1921**, *369* (3), 253–287.
72. Luo, D.; Qiao, X.; Dronskowski, R. Predicting Nitrogen-Based Families of Compounds: Transition-Metal Guanidinates TCN_3 ($T = \text{V}, \text{Nb}, \text{Ta}$) and Ortho-Nitrido Carbonates T_2CN_4 ($T = \text{Ti}, \text{Zr}, \text{Hf}$). *Angew. Chem. Int. Ed.* **2021**, *60* (1), 486–492.
73. Lewis, G. N. The Atom and the Molecule. *J. Am. Chem. Soc.* **1916**, *38* (4), 762–785.
74. Hughbanks, T.; Hoffmann, R. Chains of Trans-Edge-Sharing Molybdenum Octahedra: Metal-Metal Bonding in Extended Systems. *J. Am. Chem. Soc.* **1983**, *105* (11), 3528–3537.
75. Dronskowski, R.; Blöchl, P. E. Crystal Orbital Hamilton populations (COHP): Energy-Resolved Visualization of Chemical Bonding in Solids Based on Density-Functional Calculations. *J. Phys. Chem.* **1993**, *97* (33), 8617–8624.
76. Börnsen, N.; Meyer, B.; Grotheer, O.; Fähnle, M. Ecov—a New Tool for the Analysis of Electronic Structure Data in a Chemical Language. *J. Phys. Condens. Matter* **1999**, *11* (25), L287.
77. Slater, J. C. Atomic Shielding Constants. *Phys. Rev.* **1930**, *36* (1), 57–64.
78. Boys, S. F.; Egerton, A. C. Electronic Wave Functions—I. A General Method of Calculation for the Stationary States of Any Molecular System. *Proc. R. Soc. Lond. Ser. A Math. Phys. Sci.* **1950**, *200* (1063), 542–554.
79. Hellmann, H.; Kassatotschkin, W. Metallic Binding According to the Combined Approximation Procedure. *J. Chem. Phys.* **1936**, *4* (5), 324–325.
80. Hellmann, H. A New Approximation Method in the Problem of Many Electrons. *J. Chem. Phys.* **1935**, *3* (1), 61.
81. Kerker, G. Non-Singular Atomic Pseudopotentials for Solid State Applications. *J. Phys. C* **1980**, *13* (9), L189.
82. Phillips, J. C.; Kleinman, L. New Method for Calculating Wave Functions in Crystals and Molecules. *Phys. Rev.* **1959**, *116* (2), 287.
83. Phillips, J. C. Energy-band Interpolation Scheme Based on a Pseudopotential. *Phys. Rev.* **1958**, *112* (3), 685.
84. Cohen, M. L.; Heine, V. The Fitting of Pseudopotentials to Experimental Data and Their Subsequent Application. In *Solid State Physics*; vol. 24; Elsevier, 1970; ; pp 37–248.
85. Hamann, D.; Schlüter, M.; Chiang, C. Norm-Conserving Pseudopotentials. *Phys. Rev. Lett.* **1979**, *43* (20), 1494.
86. Foulkes, W.; Mitas, L.; Needs, R.; Rajagopal, G. Quantum Monte Carlo Simulations of Solids. *Rev. Mod. Phys.* **2001**, *73* (1), 33.
87. Christiansen, P. A.; Lee, Y. S.; Pitzer, K. S. Improved Ab initio Effective Core Potentials for Molecular Calculations. *J. Chem. Phys.* **1979**, *71* (11), 4445–4450.
88. Burkatzki, M.; Filippi, C.; Dolg, M. Energy-Consistent Pseudopotentials for Quantum Monte Carlo Calculations. *J. Chem. Phys.* **2007**, *126* (23), 234105.
89. Vanderbilt, D. Soft self-consistent pseudopotentials in a generalized eigenvalue formalism. *Phys. Rev. B* **1990**, *41* (11), 7892–7895.
90. Blöchl, P. E. Projector Augmented-Wave Method. *Phys. Rev. B* **1994**, *50* (24), 17953–17979.

91. Andersen, O. K. Linear Methods in Band Theory. *Phys. Rev. B* **1975**, *12* (8), 3060–3083.
92. Holzwarth, N. A. W.; Matthews, G. E.; Dunning, R. B.; Tackett, A. R.; Zeng, Y. Comparison of the Projector Augmented-Wave, Pseudopotential, and Linearized Augmented-Plane-Wave Formalisms for Density-Functional Calculations of Solids. *Phys. Rev. B* **1997**, *55* (4), 2005–2017.
93. Kresse, G.; Joubert, D. From Ultrasoft Pseudopotentials to the Projector Augmented-Wave Method. *Phys. Rev. B* **1999**, *59* (3), 1758–1775.
94. Kresse, G.; Furthmüller, J. Efficiency of Ab-Initio Total Energy Calculations for Metals and Semiconductors Using a Plane-Wave Basis Set. *Comput. Mater. Sci.* **1996**, *6* (1), 15–50.
95. Kresse, G.; Furthmüller, J. Efficient Iterative Schemes for Ab Initio Total-Energy Calculations Using a Plane-Wave Basis Set. *Phys. Rev. B* **1996**, *54* (16), 11169–11186.
96. Kresse, G.; Hafner, J. Ab Initio Molecular Dynamics for Liquid Metals. *Phys. Rev. B* **1993**, *47* (1), 558–561.
97. Wende, F.; Marsman, M.; Kim, J.; Vasilev, F.; Zhao, Z.; Steinke, T. OpenMP in VASP: Threading and SIMD. *Int. J. Quant. Chem.* **2019**, *119* (12), e25851.
98. Maintz, S.; Eck, B.; Drönskowski, R. Speeding Up Plane-Wave Electronic-Structure Calculations Using Graphics-Processing Units. *Comput. Phys. Commun.* **2011**, *182* (7), 1421–1427.
99. Hutchinson, M.; Widom, M. VASP on a GPU: Application to Exact-Exchange Calculations of the Stability of Elemental Boron. *Comput. Phys. Commun.* **2012**, *183* (7), 1422–1426.
100. Hacene, M.; Anciaux-Sedrakian, A.; Rozanska, X.; Klahr, D.; Guignon, T.; Fleurat-Lessard, P. Accelerating VASP Electronic Structure Calculations Using Graphic Processing Units. *J. Comput. Chem.* **2012**, *33* (32), 2581–2589.
101. Gonze, X.; Amadon, B.; Antonius, G.; Arnaldi, F.; Baguet, L.; Beuken, J.-M.; Bieder, J.; Bottin, F.; Bouchet, J.; Bousquet, E.; Brouwer, N.; Bruneval, F.; Brunin, G.; Cavignac, T.; Charraud, J.-B.; Chen, W.; Côté, M.; Cottener, S.; Denier, J.; Geneste, G.; Ghosez, P.; Giantomassi, M.; Gillet, Y.; Gingras, O.; Hamann, D. R.; Hautier, G.; He, X.; Helbig, N.; Holzwarth, N.; Jia, Y.; Jollet, F.; Lafargue-Dit-Hauret, W.; Lejaeghere, K.; Marques, M. A. L.; Martin, A.; Martins, C.; Miranda, H. P. C.; Naccarato, F.; Persson, K.; Petretto, G.; Planes, V.; Pouillon, Y.; Prokhortchenko, S.; Ricci, F.; Rignanese, G.-M.; Romero, A. H.; Schmitt, M. M.; Torrent, M.; van Setten, M. J.; Van Troeye, B.; Verstraete, M. J.; Zerah, G.; Zwanziger, J. W. The Ab Initproject: Impact, Environment and Recent Developments. *Comput. Phys. Commun.* **2020**, *248*, 107042.
102. Romero, A. H.; Allan, D. C.; Amadon, B.; Antonius, G.; Appelcourt, T.; Baguet, L.; Bieder, J.; Bottin, F.; Bouchet, J.; Bousquet, E.; Bruneval, F.; Brunin, G.; Caliste, D.; Côté, M.; Denier, J.; Dreyer, C.; Ghosez, P.; Giantomassi, M.; Gillet, Y.; Gingras, O.; Hamann, D. R.; Hautier, G.; Jollet, F.; Jomard, G.; Martin, A.; Miranda, H. P. C.; Naccarato, F.; Petretto, G.; Pike, N. A.; Planes, V.; Prokhortchenko, S.; Rangel, T.; Ricci, F.; Rignanese, G.-M.; Royo, M.; Stengel, M.; Torrent, M.; van Setten, M. J.; Van Troeye, B.; Verstraete, M. J.; Wiktor, J.; Zwanziger, J. W.; Gonze, X. ABINIT: Overview and Focus on Selected Capabilities. *J. Chem. Phys.* **2020**, *152* (12), 124102.
103. Torrent, M.; Jollet, F.; Bottin, F.; Zerah, G.; Gonze, X. Implementation of the Projector Augmented-Wave Method in the ABINIT Code: Application to the Study of Iron Under Pressure. *Comput. Mater. Sci.* **2008**, *42* (2), 337–351.
104. Gonze, X.; Beuken, J. M.; Caracas, R.; Detraux, F.; Fuchs, M.; Rignanese, G. M.; Sindic, L.; Verstraete, M.; Zerah, G.; Jollet, F.; Torrent, M.; Roy, A.; Mikami, M.; Ghosez, P.; Raty, J. Y.; Allan, D. C. First-Principles Computation of Material Properties: The ABINIT Software Project. *Comput. Mater. Sci.* **2002**, *25* (3), 478–492.
105. Levitt, A.; Torrent, M. Parallel Eigensolvers in Plane-Wave Density Functional Theory. *Comput. Phys. Commun.* **2015**, *187*, 98–105.
106. Bottin, F.; Leroux, S.; Knyazev, A.; Zerah, G. Large-Scale Ab Initio Calculations Based on Three Levels of Parallelization. *Comput. Mater. Sci.* **2008**, *42* (2), 329–336.
107. Jollet, F.; Torrent, M.; Holzwarth, N. Generation of Projector Augmented-Wave Atomic data: A 71 Element Validated Table in the XML Format. *Comput. Phys. Commun.* **2014**, *185* (4), 1246–1254.
108. Giannozzi, P.; Baroni, S.; Bonini, N.; Calandra, M.; Car, R.; Cavazzoni, C.; Ceresoli, D.; Chiarotti, G. L.; Cococcioni, M.; Dabo, I.; Dal Corso, A.; de Gironcoli, S.; Fabris, S.; Fratesi, G.; Gebauer, R.; Gerstmann, U.; Gougoussis, C.; Kokalj, A.; Lazzeri, M.; Martin-Samos, L.; Marzari, N.; Mauri, F.; Mazzarello, R.; Paolini, S.; Pasquarello, A.; Paulatto, L.; Sbraccia, C.; Scandolo, S.; Sclauzero, G.; Seitsonen, A. P.; Smogunov, A.; Umari, P.; Wentzcovitch, R. M. QUANTUM ESPRESSO: A Modular and Open-Source Software Project for Quantum Simulations of Materials. *J. Phys. Condens. Matter* **2009**, *21* (39), 395502.
109. Giannozzi, P.; Andreussi, O.; Brumme, T.; Bunau, O.; Buongiorno Nardelli, M.; Calandra, M.; Car, R.; Cavazzoni, C.; Ceresoli, D.; Cococcioni, M.; Colonna, N.; Carnimeo, I.; Dal Corso, A.; de Gironcoli, S.; Delugas, P.; DiStasio, R. A.; Ferretti, A.; Floris, A.; Fratesi, G.; Fugallo, G.; Gebauer, R.; Gerstmann, U.; Giustino, F.; Gorni, T.; Jia, J.; Kawamura, M.; Ko, H. Y.; Kokalj, A.; Küçükbenli, E.; Lazzeri, M.; Marsili, M.; Marzari, N.; Mauri, F.; Nguyen, N. L.; Nguyen, H. V.; Otero-de-la-Roza, A.; Paulatto, L.; Poncé, S.; Rocca, D.; Sabatini, R.; Santra, B.; Schlipf, M.; Seitsonen, A. P.; Smogunov, A.; Timrov, I.; Thonhauser, T.; Umari, P.; Vast, N.; Wu, X.; Baroni, S. Advanced Capabilities for Materials Modelling With Quantum ESPRESSO. *J. Phys. Condens. Matter* **2017**, *29* (46), 465901.
110. Giannozzi, P.; Baseggio, O.; Bonfà, P.; Brunato, D.; Car, R.; Carnimeo, I.; Cavazzoni, C.; de Gironcoli, S.; Delugas, P.; Ferrari Ruffino, F.; Ferretti, A.; Marzari, N.; Timrov, I.; Urri, A.; Baroni, S. Quantum ESPRESSO Toward the Exascale. *J. Chem. Phys.* **2020**, *152* (15), 154105.
111. Lejaeghere, K.; Bihlmayer, G.; Björkman, T.; Blaha, P.; Blügel, S.; Blum, V.; Caliste, D.; Castelli, I. E.; Clark, S. J.; Dal Corso, A.; de Gironcoli, S.; Deutsch, T.; Dewhurst, J. K.; Di Marco, I.; Draxl, C.; Dušák, M.; Eriksson, O.; Flores-Livas, J. A.; Garrity, K. F.; Genovese, L.; Giannozzi, P.; Giantomassi, M.; Goedecker, S.; Gonze, X.; Gránás, O.; Gross, E. K. U.; Gullans, A.; Gygi, F.; Hamann, D. R.; Hasnip, P. J.; Holzwarth, N. A. W.; İlhan, D.; Jochym, D. B.; Jollet, F.; Jones, D.; Kresse, G.; Koepenik, K.; Küçükbenli, E.; Kvashnin, Y. O.; Locht, I. L. M.; Lubeck, S.; Marsman, M.; Marzari, N.; Nitzsche, U.; Nordström, L.; Ozaki, T.; Paulatto, L.; Pickard, C. J.; Poelmans, W.; Probert, M. I. J.; Refson, K.; Richter, M.; Rignanese, G.-M.; Saha, S.; Scheffler, M.; Schlipf, M.; Schwarz, K.; Sharma, S.; Tavazza, F.; Thunström, P.; Tkatchenko, A.; Torrent, M.; Vanderbilt, D.; van Setten, M. J.; Van Speybroeck, V.; Wills, J. M.; Yates, J. R.; Zhang, G.-X.; Cottenier, S. Reproducibility in Density Functional Theory Calculations of Solids. *Science* **2016**, *351* (6280), aad3000.
112. Topsakal, M.; Wentzcovitch, R. M. Accurate Projected Augmented Wave (PAW) Datasets for Rare-Earth Elements (RE=La–Lu). *Comput. Mater. Sci.* **2014**, *95*, 263–270.
113. van Setten, M. J.; Giantomassi, M.; Bousquet, E.; Verstraete, M. J.; Hamann, D. R.; Gonze, X.; Rignanese, G. M. The PseudoDojo: Training and Grading a 85 Element Optimized Norm-Conserving Pseudopotential Table. *Comput. Phys. Commun.* **2018**, *226*, 39–54.
114. Schlipf, M.; Gygi, F. Optimization Algorithm for the Generation of ONCV Pseudopotentials. *Comput. Phys. Commun.* **2015**, *196*, 36–44.
115. Hamann, D. R. Optimized Norm-Conserving Vanderbilt Pseudopotentials. *Phys. Rev. B* **2013**, *88* (8), 085117.
116. Drönskowski, R. *Computational Chemistry of Solid State Materials: A Guide for Materials Scientists, Chemists, Physicists and Others*, Wiley-VCH Verlag GmbH & Co. KGaA: Weinheim, New York, 2005.
117. Heine, V. Electronic Structure from the Point of View of the Local Atomic Environment. In *Solid State Physics*; Ehrenreich, H., Seitz, F., Turnbull, D., Eds.; vol. 35; Academic Press, 1980; pp 1–127.
118. Agapito, L. A.; Ferretti, A.; Calzolari, A.; Curtarolo, S.; Buongiorno Nardelli, M. Effective and Accurate Representation of Extended Bloch States on Finite Hilbert Spaces. *Phys. Rev. B* **2013**, *88* (16), 165127.
119. Sanchez-Portal, D.; Artacho, E.; Soler, J. M. Projection of Plane-Wave Calculations Into Atomic Orbitals. *Solid State Commun.* **1995**, *95* (10), 685–690.
120. Sánchez-Portal, D.; Artacho, E.; Soler, J. M. Analysis of Atomic Orbital Basis Sets From the Projection of Plane-Wave Results. *J. Phys. Condens. Matter* **1996**, *8* (21), 3859–3880.
121. Maintz, S.; Deringer, V. L.; Tchougréeff, A. L.; Drönskowski, R. Analytic Projection From Plane-Wave and PAW Wavefunctions and Application to Chemical-Bonding Analysis in Solids. *J. Comput. Chem.* **2013**, *34* (29), 2557–2567.
122. Maintz, S.; Deringer, V. L.; Tchougréeff, A. L.; Drönskowski, R. LOBSTER: A Tool to Extract Chemical Bonding From Plane-Wave Based DFT. *J. Comput. Chem.* **2016**, *37* (11), 1030–1035.
123. Boost (n.d.) <https://www.boost.org/>.
124. Guennebaud, G.; Jacob, B (n.d.) <https://eigen.tuxfamily.org>.
125. Bunge, C. F.; Barrientos, J. A.; Bunge, A. V. Roothaan-Hartree-Fock Ground-State Atomic Wave Functions: Slater-Type Orbital Expansions and Expectation Values for Z = 2–54. At. Data Nucl. Data Tables **1993**, *53* (1), 113–162.

126. Koga, T.; Kanayama, K.; Watanabe, S.; Thakkar, A. J. Analytical Hartree-Fock Wave Functions Subject to Cusp and Asymptotic Constraints: He to Xe, Li⁺ to Cs⁺, H⁻ to I⁻. *Int. J. Quant. Chem.* **1999**, *71* (6), 491–497.
127. Koga, T.; Kanayama, K.; Watanabe, T.; Imai, T.; Thakkar, A. J. Analytical Hartree-Fock Wave Functions for the Atoms Cs to Lr. *Theor. Chem. Acc.* **2000**, *104* (5), 411–413.
128. Froese Fischer, C. *The Hartree-Fock Method for Atoms: A Numerical Approach/Charlotte Froese Fischer*, Wiley: New York, 1977.
129. Steiner, E. Charge Densities in Atoms. *J. Chem. Phys.* **1963**, *39* (9), 2365–2366.
130. Chong, D. P. Coalescence Conditions as Constraints in Open-Shell SCF Theory. *J. Chem. Phys.* **1967**, *47* (12), 4907–4909.
131. Handy, N. C.; Marron, M. T.; Silverstone, H. J. Long-Range Behavior of Hartree-Fock Orbitals. *Phys. Rev.* **1969**, *180* (1), 45–48.
132. Handler, G. S.; Smith, D. W.; Silverstone, H. J. Asymptotic Behavior of Atomic Hartree-Fock Orbitals. *J. Chem. Phys.* **1980**, *73* (8), 3936–3938.
133. Davis, C. L.; Jensen, H. J. R. A.; Monkhorst, H. J. Accurate Hartree-Fock Wave Functions Without Exponent Optimization. *J. Chem. Phys.* **1984**, *80* (2), 840–855.
134. Ishida, T.; Ohno, K. On the Asymptotic Behavior of Hartree-Fock Orbitals. *Theor. Chim. Acta* **1992**, *81* (6), 355–364.
135. Adhikari, S.; Mukhopadhyay, P. Physical Metallurgy of Beryllium and Its Alloys. *Miner. Process. Extr. Metall. Rev.* **1995**, *14* (1), 253–299.
136. Perdew, J. P.; Burke, K.; Ernzerhof, M. Generalized Gradient Approximation Made Simple. *Phys. Rev. Lett.* **1996**, *77* (18), 3865–3868.
137. Andersen, O. K.; Jepsen, O. Explicit, First-Principles Tight-Binding Theory. *Phys. Rev. Lett.* **1984**, *53* (27), 2571–2574.
138. Dresselhaus, M. S.; Dresselhaus, G.; Jorio, A. *Group Theory: Application to the Physics of Condensed Matter*, Springer: Berlin, 2008.
139. Häussermann, U.; Berastegui, P.; Carlson, S.; Haines, J.; Léger, J.-M. TiF and PbO Under High Pressure: Unexpected Persistence of the Stereochemically Active Electron Pair. *Angew. Chem. Int. Ed.* **2001**, *40* (24), 4624–4629.
140. Sun, X.; Li, X.; Yang, J.; Xi, J.; Nelson, R.; Ertural, C.; Dronskowski, R.; Liu, W.; Snyder, G. J.; Singh, D. J.; Zhang, W. Achieving Band Convergence by Tuning the Bonding Ionicity in n-type Mg₃Sb₂. *J. Comput. Chem.* **2019**, *40* (18), 1693–1700.
141. Chen, W.; George, J.; Varley, J. B.; Rignanese, G.-M.; Hautier, G. High-Throughput Computational Discovery of In₂Mn₂O₇ as a High Curie Temperature Ferromagnetic Semiconductor for Spintronics. *NPJ Comput. Mat.* **2019**, *5* (1), 72.
142. Li, R.; Li, X.; Xi, L.; Yang, J.; Singh, D. J.; Zhang, W. High-Throughput Screening for Advanced Thermoelectric Materials: Diamond-Like ABX₂ Compounds. *ACS Appl. Mater. Interfaces* **2019**, *11* (28), 24859–24866.
143. Nakada, A.; Kato, D.; Nelson, R.; Takahira, H.; Yabuuchi, M.; Higashi, M.; Suzuki, H.; Kirsanova, M.; Kakudou, N.; Tassel, C.; Yamamoto, T.; Brown, C. M.; Dronskowski, R.; Saeki, A.; Abakumov, A.; Kageyama, H.; Abe, R. Conduction Band Control of Oxyhalides With a Triple-Fluorite Layer for Visible Light Photocatalysis. *J. Am. Chem. Soc.* **2021**, *143* (6), 2491–2499.
144. Müller, P. C.; Ertural, C.; Hempelmann, J.; Dronskowski, R. Crystal Orbital Bond Index: Covalent Bond Orders in Solids. *J. Phys. Chem. C* **2021**, *125* (14), 7959–7970.
145. Wiberg, K. B. Application of the Pople-Santry-Segal CNDO Method to the Cyclopropylcarbinyl and Cyclobutyl Cation and to Bicyclobutane. *Tetrahedron* **1968**, *24* (3), 1083–1096.
146. Pople, J. A.; Santry, D. P.; Segal, G. A. Approximate Self-Consistent Molecular Orbital Theory. I. Invariant Procedures. *J. Chem. Phys.* **1965**, *43* (10), S129–S135.
147. Pople, J. A.; Segal, G. A. Approximate Self-Consistent Molecular Orbital Theory. II. Calculations With Complete Neglect of Differential Overlap. *J. Chem. Phys.* **1965**, *43* (10), S136–S151.
148. Pople, J. A.; Segal, G. A. Approximate Self-Consistent Molecular Orbital Theory. III. CNDO Results for AB₂ and AB₃ Systems. *J. Chem. Phys.* **1966**, *44* (9), 3289–3296.
149. Mayer, I. Charge, Bond Order and Valence in the Ab Initio SCF Theory. *Chem. Phys. Lett.* **1983**, *97* (3), 270–274.
150. Mayer, I. Bond Order and Valence Indices: A Personal Account. *J. Comput. Chem.* **2007**, *28* (1), 204–221.
151. Giambiagi, M.; de Giambiagi, M. S.; Mundim, K. C. Definition of a Multicenter Bond Index. *Struct. Chem.* **1990**, *1* (5), 423–427.
152. Kar, T.; Marcos, E. S. Three-Center Four-Electron Bonds and Their Indices. *Chem. Phys. Lett.* **1992**, *192* (1), 14–20.
153. Sannigrahi, A.; Kar, T. Three-Center Bond Index. *Chem. Phys. Lett.* **1990**, *173* (5–6), 569–572.
154. Ponec, R.; Uhlik, F. Multicentre Bond Indices From the Generalized Population Analysis of Higher Order Densities. *Croat. Chem. Acta* **1996**, *69* (3), 941–954.
155. Stock, A. *Hydrides of Boron and Silicon*, Cornell University Press: Ithaca, NY, 1933.
156. Hoppe, R.; Dähne, W.; Mattauch, H.; Rödder, K. Fluorination of Xenon. *Angew. Chem. Int. Ed. Engl.* **1962**, *1*, 599.
157. Longuet-Higgins, H. G. Substances Hydrogénées Avec Défaut d'électrons. *J. Chim. Phys.* **1949**, *46*, 268–275.
158. Lipscomb, W. N. The Boranes and Their Relatives. *Science* **1977**, *196* (4294), 1047–1055.
159. Lipscomb, W. N. Framework Rearrangement in Boranes and Carboranes. *Science* **1966**, *153* (3734), 373–378.
160. Müller, P. C. *Quantum Chemical Descriptors Towards Materials Mapping*, Master Thesis, RWTH Aachen, 2019.
161. Pfeiffer, P. Die Kristalle als Moleküverbündungen. *Z. Anorg. Allg. Chem.* **1915**, *92* (1), 376–380.
162. Pfeiffer, P. Die Kristalle als Moleküverbündungen. II. *Z. Anorg. Allg. Chem.* **1916**, *97* (1), 161–174.
163. Hoppe, R. The Coordination Number—An "Inorganic Chameleon". *Angew. Chem. Int. Ed. Engl.* **1970**, *9* (1), 25–34.
164. Hoppe, R. Effective Coordination Numbers (ECoN) and Mean Fictive Ionic Radii (MEFIR). *Z. Kristallogr. Crystall. Mater.* **1979**, *150* (1–4), 23–52.
165. Schulze, G. E. R. *Metalphysik*, Akademie-Verlag: Berlin, 1967.
166. Raty, J.-Y.; Schumacher, M.; Golub, P.; Deringer, V. L.; Gatti, C.; Wuttig, M. A Quantum-Mechanical Map for Bonding and Properties in Solids. *Adv. Mater.* **2019**, *31* (3), 1806280.
167. Shportko, K.; Kremers, S.; Woda, M.; Lencer, D.; Robertson, J.; Wuttig, M. Resonant Bonding in Crystalline Phase-Change Materials. *Nat. Mater.* **2008**, *7* (8), 653.
168. Wuttig, M.; Deringer, V. L.; Gonze, X.; Bichara, C.; Raty, J.-Y. Incipient Metals: Functional Materials With a Unique Bonding Mechanism. *Adv. Mater.* **2018**, *30* (51), 1803777.
169. Lee, T. H.; Elliott, S. R. Multi-Center Hyperbonding in Phase-Change Materials. *Phys. Status Solidi* **2021**, *2021*, 2000516.
170. Lee, T. H.; Elliott, S. R. Chemical Bonding in Chalcogenides: The Concept of Multicenter Hyperbonding. *Adv. Mater.* **2020**, *32* (28), 2000340.
171. Rao, C. N. R.; Gopalakrishnan, J. *New Directions in Solid State Chemistry*, Cambridge University Press, 1997.
172. Esser, M.; Maintz, S.; Dronskowski, R. Automated First-Principles Mapping for Phase-Change Materials. *J. Comput. Chem.* **2017**, *38* (9), 620–628.
173. Hannay, N. B.; Smyth, C. P. The Dipole Moment of Hydrogen Fluoride and the Ionic Character of Bonds. *J. Am. Chem. Soc.* **1946**, *68* (2), 171–173.
174. Mann, J. B.; Meel, T. L.; Knight, E. T.; Capitani, J. F.; Allen, L. C. Configuration Energies of the d-Block Elements. *J. Am. Chem. Soc.* **2000**, *122* (21), 5132–5137.
175. Madelung, E. Das Elektrische Feld in Systemen von regelmäßig angeordneten Punktladungen. *Phys. Z.* **1918**, *19*, 524–533.
176. Born, M. Die Elektronenaffinität der Halogenatome. *Verh. Deutsch. Phys. Ges.* **1919**, *21*, 679–685.
177. Haber, F. *Verh. Deutsch. Phys. Ges.* **1919**, *21*, 750–768.
178. Williams, D. E. Accelerated Convergence of Crystal-Lattice Potential Sums. *Acta Crystallogr. A* **1971**, *27* (5), 452–455.
179. van Eljck, B. P.; Kroon, J. Coulomb Energy of Polar Crystals. *J. Phys. Chem. B* **1997**, *101* (6), 1096–1100.
180. Bertaut, F. L'énergie Électrostatique de Réseaux Ioniques. *J. Phys. Rad.* **1952**, *13* (11), 499–505.
181. Mooser, E.; Pearson, W. B. On the Crystal Chemistry of Normal Valence Compounds. *Acta Crystallogr.* **1959**, *12* (12), 1015–1022.
182. Eickmeier, K.; Steinberg, S. Revealing the Bonding Nature in an ALnZnTe₃-Type Alkaline-Metal (A) Lanthanide (Ln) Zinc Telluride by Means of Experimental and Quantum-Chemical Techniques. *Crystals* **2020**, *10* (10), 916.
183. Eickmeier, K.; Fries, K. S.; Gladisch, F. C.; Dronskowski, R.; Steinberg, S. Revisiting the Zintl-Klemm Concept for ALn₂Ag₃Te₅-Type Alkaline-Metal (A) Lanthanide (Ln) Silver Tellurides. *Crystals* **2020**, *10* (3), 184.
184. Fincham, D. Optimisation of the Ewald sum for Large Systems. *Mol. Simul.* **1994**, *13* (1), 1–9.
185. Stoffel, R. P.; Dronskowski, R. First-Principles Investigations of the Structural, Vibrational and Thermochemical Properties of Barium Cerate—Another Test Case for Density-Functional Theory. *Z. Anorg. Allg. Chem.* **2013**, *639* (7), 1227–1231.

186. Pimentel, G. C. The Bonding of Trihalide and Bisfluoride Ions by the Molecular Orbital Method. *J. Chem. Phys.* **1951**, *19* (4), 446–448.
187. Rundle, R. Electron Deficient Compounds. II. Relative Energies of "Half-Bonds". *J. Chem. Phys.* **1949**, *17* (8), 671–675.
188. Rundle, R. Electron Deficient Compounds 1. *J. Am. Chem. Soc.* **1947**, *69* (6), 1327–1331.
189. Skriver, H. L. *The LMTO Method: Muffin-Tin Orbitals and Electronic Structure*; vol. 41; Springer Science & Business Media, 2012.
190. Zólyomi, V.; Kúrti, J. First-Principles Calculations for the Electronic Band Structures of Small Diameter Single-Wall Carbon Nanotubes. *Phys. Rev. B* **2004**, *70* (8), 085403.
191. Hoffmann, R. Small But Strong Lessons From Chemistry for Nanoscience. *Angew. Chem. Int. Ed.* **2013**, *52* (1), 93–103.
192. Yamada, T.; Liu, X.; Englert, U.; Yamane, H.; Dronskowski, R. Solid-State Structure of Free Base Guanidine Achieved at Last. *Chem. A Eur. J.* **2009**, *15* (23), 5651–5655.
193. Pitonák, M.; Riley, K. E.; Neogrády, P.; Hobza, P. Highly Accurate CCSD(T) and DFT–SAPT Stabilization Energies of H-Bonded and Stacked Structures of the Uracil Dimer. *ChemPhysChem* **2008**, *9* (11), 1636–1644.
194. Grimme, S.; Ehrlich, S.; Goerigk, L. Effect of the Damping Function in Dispersion Corrected Density Functional Theory. *J. Comput. Chem.* **2011**, *32* (7), 1456–1465.
195. Tkatchenko, A.; Scheffler, M. Accurate Molecular Van Der Waals Interactions From Ground-State Electron Density and Free-Atom Reference Data. *Phys. Rev. Lett.* **2009**, *102* (7), 073005.
196. Lee, K.; Murray, É. D.; Kong, L.; Lundqvist, B. I.; Langreth, D. C. Higher-Accuracy Van Der Waals Density Functional. *Physical Review B* **2010**, *82* (8), 081101.
197. Hoepfner, V.; Deringer, V. L.; Dronskowski, R. Hydrogen-Bonding Networks From First-Principles: Exploring the Guanidine Crystal. *Chem. A Eur. J.* **2012**, *116* (18), 4551–4559.
198. Deringer, V. L.; Englert, U.; Dronskowski, R. Nature, Strength, and Cooperativity of the Hydrogen-Bonding Network in α -Chitin. *Biomacromolecules* **2016**, *17* (3), 996–1003.
199. Grabowski, S. J. What Is the Covalency of Hydrogen Bonding? *Chem. Rev.* **2011**, *111* (4), 2597–2625.
200. Deringer, V. L.; Englert, U.; Dronskowski, R. Covalency of Hydrogen Bonds in Solids Revisited. *Chem. Commun.* **2014**, *50* (78), 11547–11549.
201. Guthrie, F. XXVIII—On the Iodide of Iodammonium. *J. Chem. Soc.* **1863**, *16*, 239–244.
202. George, J.; Deringer, V. L.; Dronskowski, R. Cooperativity of Halogen, Chalcogen, and Pnictogen Bonds in Infinite Molecular Chains by Electronic Structure Theory. *Chem. A Eur. J.* **2014**, *118* (17), 3193–3200.
203. Deringer, V. L.; George, J.; Dronskowski, R.; Englert, U. Plane-Wave Density Functional Theory Meets Molecular Crystals: Thermal Ellipsoids and Intermolecular Interactions. *Acc. Chem. Res.* **2017**, *50* (5), 1231–1239.
204. Politzer, P.; Murray, J. S. Halogen Bonding: An Interim Discussion. *ChemPhysChem* **2013**, *14* (2), 278–294.
205. George, J.; Dronskowski, R. Tetrel Bonds in Infinite Molecular Chains by Electronic Structure Theory and Their Role for Crystal Stabilization. *Chem. A Eur. J.* **2017**, *121* (6), 1381–1387.
206. Deringer, V. L.; Lumeij, M.; Dronskowski, R. Ab Initio Modeling of α -GeTe(111) Surfaces. *J. Phys. Chem. C* **2012**, *116* (29), 15801–15811.
207. Deringer, V. L.; Dronskowski, R. Ab Initio Study of Molecular and Atomic Oxygen on GeTe(111) Surfaces. *J. Appl. Phys.* **2014**, *116* (17), 173703.
208. Yashina, L. V.; Püttner, R.; Neudachina, V. S.; Zyubina, T. S.; Shtanov, V. I.; Poygin, M. V. X-Ray Photoelectron Studies of Clean and Oxidized α -GeTe(111) Surfaces. *J. Appl. Phys.* **2008**, *103* (9), 094909.
209. Deringer, V. L.; Dronskowski, R. Pauling's Third Rule Beyond the Bulk: Chemical Bonding at Quartz-Type GeO₂ Surfaces. *Chem. Sci.* **2014**, *5* (3), 894–903.
210. Ovshinsky, S. R. Reversible Electrical Switching Phenomena in Disordered Structures. *Phys. Rev. Lett.* **1968**, *21* (20), 1450–1453.
211. Deringer, V. L.; Dronskowski, R.; Wuttig, M. Microscopic Complexity in Phase-Change Materials and Its Role for Applications. *Adv. Funct. Mater.* **2015**, *25* (40), 6343–6359.
212. Klemm, W.; Frischmuth, G. Das System Germanium–Tellur. *Z. Anorg. Allg. Chem.* **1934**, *218* (3), 249–251.
213. Chattopadhyay, T.; Boucherle, J. X.; vonSchnering, H. G. Neutron Diffraction Study on the Structural Phase Transition in GeTe. *J. Phys. C: Solid State Phys.* **1987**, *20* (10), 1431–1440.
214. Deringer, V. L.; Zhang, W.; Lumeij, M.; Maintz, S.; Wuttig, M.; Mazzarello, R.; Dronskowski, R. Bonding Nature of Local Structural Motifs in Amorphous GeTe. *Angew. Chem. Int. Ed.* **2014**, *53* (40), 10817–10820.
215. Kühne, T. D.; Krack, M.; Mohamed, F. R.; Parrinello, M. Efficient and Accurate Car-Parrinello-like Approach to Born-Oppenheimer Molecular Dynamics. *Phys. Rev. Lett.* **2007**, *98* (6), 066401.
216. Wuttig, M.; Lüsebrink, D.; Wamwangi, D.; Wehnic, W.; Gilleßen, M.; Dronskowski, R. The Role of Vacancies and Local Distortions in the Design of New Phase-Change Materials. *Nat. Mater.* **2007**, *6* (2), 122–128.
217. Kolobov, A. V.; Tominaga, J.; Fons, P.; Uruga, T. Local Structure of Crystallized GeTe Films. *Appl. Phys. Lett.* **2003**, *82* (3), 382–384.
218. Schröder, T.; Rosenthal, T.; Grott, S.; Stiewe, C.; de Boor, J.; Oeckler, O. Disorder and Transport Properties of In₃SbTe₂—An X-ray, Neutron and Electron Diffraction Study. *Z. Anorg. Allg. Chem.* **2013**, *639* (14), 2536–2541.
219. Deringer, V. L.; Zhang, W.; Rausch, P.; Mazzarello, R.; Dronskowski, R.; Wuttig, M. A Chemical Link Between Ge–Sb–Te and In–Sb–Te Phase-Change Materials. *J. Mat. Chem. C* **2015**, *3* (37), 9519–9523.
220. Muir, J. A.; Cashman, R. J. *Bull. Am. Phys. Soc.* **1966**, *8*, 2.
221. Küpers, M.; Konze, P. M.; Maintz, S.; Steinberg, S.; Mio, A. M.; Cojocaru-Mirédin, O.; Zhu, M.; Müller, M.; Luysberg, M.; Mayer, J.; Wuttig, M.; Dronskowski, R. Unexpected Ge–Ge Contacts in the Two-Dimensional Ge₄Se₃Te Phase and Analysis of Their Chemical Cause with the Density of Energy (DOE) Function. *Angew. Chem. Int. Ed.* **2017**, *56* (34), 10204–10208.
222. Konze, P. M.; Dronskowski, R.; Deringer, V. L. Exploring Chemical Bonding in Phase-Change Materials with Orbital-Based Indicators. *Phys. Status Solidi* **2019**, *13* (4), 1800579.
223. Landrum, G. A.; Dronskowski, R. The Orbital Origins of Magnetism: From Atoms to Molecules to Ferromagnetic Alloys. *Angew. Chem. Int. Ed.* **2000**, *39* (9), 1560–1585.
224. Decker, A.; Landrum, G. A.; Dronskowski, R. Structural and Electronic Peierls Distortions in the Elements (B): The Antiferromagnetism of Chromium. *Z. Anorg. Allg. Chem.* **2002**, *628* (1), 303–309.
225. Fokwa, B. P. T.; Lueken, H.; Dronskowski, R. Rational Synthetic Tuning between Itinerant Antiferromagnetism and Ferromagnetism in the Complex Boride Series Sc₂FeR₅_–_nRh_nB₂ (0 ≤ n ≤ 5). *Chem. A Eur. J.* **2007**, *13* (21), 6040–6046.
226. Nelson, R.; Konze, P. M.; Dronskowski, R. First-Principles Chemical Bonding Study of Manganese Carbodiimide, MnNCN, As Compared to Manganese Oxide, MnO. *Chem. A Eur. J.* **2017**, *121* (40), 7778–7786.
227. Islam, M. S.; Fisher, C. A. J. Lithium and Sodium Battery Cathode Materials: Computational Insights Into Voltage, Diffusion and Nanostructural Properties. *Chem. Soc. Rev.* **2014**, *43*, 185–204.
228. Whittingham, M. S. Materials Challenges Facing Electrical Energy Storage. *MRS Bull.* **2008**, *33* (4), 411–419.
229. Liu, J.; Zhang, J.-G.; Yang, Z.; Lemmon, J. P.; Imhoff, C.; Graff, G. L.; Li, L.; Hu, J.; Wang, C.; Xiao, J.; Xia, G.; Viswanathan, V. V.; Baskaran, S.; Sprenkle, V.; Li, X.; Shao, Y.; Schwenzer, B. Materials Science and Materials Chemistry for Large Scale Electrochemical Energy Storage: From Transportation to Electrical Grid. *Adv. Funct. Mater.* **2013**, *23* (8), 929–946.
230. Palacin, M. R. Recent Advances in Rechargeable Battery Materials: A Chemist's Perspective. *Chem. Soc. Rev.* **2009**, *38* (9), 2565–2575.
231. Thackeray, M. M.; Wolverton, C.; Isaacs, E. D. Electrical Energy Storage for Transportation—Approaching the Limits of, and Going Beyond, Lithium-Ion Batteries. *Energ. Environ. Sci.* **2012**, *5* (7), 7854–7863.
232. Dunn, B.; Kamath, H.; Tarascon, J. M. Electrical Energy Storage for the Grid: A Battery of Choices. *Science* **2011**, *334* (6058), 928–935.
233. Myung, S.-T.; Amine, K.; Sun, Y.-K. Nanostructured Cathode Materials for Rechargeable Lithium Batteries. *J. Power Sources* **2015**, *283*, 219–236.
234. The Royal Swedish Academy of Sciences (2019), *The Nobel Prize in Chemistry 2019*, Retrieved from: <https://www.nobelprize.org/prizes/chemistry/2019/press-release>.
235. Deringer, V. L. Modelling and Understanding Battery Materials With Machine-Learning-Driven Atomistic Simulations. *J. Phys.* **2020**, *2* (4), 041003.

236. Wu, Y. P.; Rahm, E.; Holze, R. Carbon Anode Materials for Lithium Ion Batteries. *J. Power Sources* **2003**, *114* (2), 228–236.
237. Kaskhedikar, N. A.; Maier, J. Lithium Storage in Carbon Nanostructures. *Adv. Mater.* **2009**, *21* (25–26), 2664–2680.
238. Kim, S.-W.; Seo, D.-H.; Ma, X.; Ceder, G.; Kang, K. Electrode Materials for Rechargeable Sodium-Ion Batteries: Potential Alternatives to Current Lithium-Ion Batteries. *Adv. Energy Mater.* **2012**, *2* (7), 710–721.
239. Nitta, N.; Wu, F.; Lee, J. T.; Yushin, G. Li-ion Battery Materials: Present and Future. *Mater. Today* **2015**, *18* (5), 252–264.
240. Irisarri, E.; Ponrouch, A.; Palacin, M. R. Review—Hard Carbon Negative Electrode Materials for Sodium-Ion Batteries. *J. Electrochem. Soc.* **2015**, *162* (14), A2476–A2482.
241. Huang, J.-X.; Csányi, G.; Zhao, J.-B.; Cheng, J.; Deringer, V. L. First-Principles Study of Alkali-Metal Intercalation in Disordered Carbon Anode Materials. *J. Mater. Chem. A* **2019**, *7* (32), 19070–19080.
242. Liang, M.; Zhi, L. Graphene-Based Electrode Materials for Rechargeable Lithium Batteries. *J. Mater. Chem.* **2009**, *19* (33), 5871–5878.
243. Liu, Y.; Merinov, B. V.; Goddard, W. A., 3rd Origin of Low Sodium Capacity in Graphite and Generally Weak Substrate Binding of Na and Mg Among Alkali and Alkaline Earth Metals. *Proc. Natl. Acad. Sci. U. S. A.* **2016**, *113* (14), 3735–3739.
244. Deringer, V. L.; Merlet, C.; Hu, Y.; Lee, T. H.; Kattirzi, J. A.; Pecher, O.; Csányi, G.; Elliott, S. R.; Grey, C. P. Towards an Atomistic Understanding of Disordered Carbon Electrode Materials. *Chem. Commun.* **2018**, *54* (47), 5988–5991.
245. Bonaccorso, F.; Colombo, L.; Yu, G.; Stoller, M.; Tozzini, V.; Ferrari, A. C.; Ruoff, R. S.; Pellegrini, V. 2D Materials. Graphene, Related Two-Dimensional Crystals, and Hybrid Systems for Energy Conversion and Storage. *Science* **2015**, *347* (6217), 1246501.
246. Egúia-Barrio, A.; Castillo-Martínez, E.; Liu, X.; Dronskowski, R.; Armand, M.; Rojo, T. Carbodiimides: New Materials Applied as Anode Electrodes for Sodium and Lithium Ion Batteries. *J. Mater. Chem. A* **2016**, *4* (5), 1608–1611.
247. Dolotko, O.; Senyshyn, A.; Mühlbauer, M. J.; Nikolicowski, K.; Ehrenberg, H. Understanding Structural Changes in NMC Li-ion Cells by In Situ Neutron Diffraction. *J. Power Sources* **2014**, *255*, 197–203.
248. Sun, J.; Ruzsinszky, A.; Perdew, J. P. Strongly Constrained and Appropriately Normed Semilocal Density Functional. *Phys. Rev. Lett.* **2015**, *115* (3), 036402.
249. Tang, W.; Sanville, E.; Henkelman, G. A Grid-Based Bader Analysis Algorithm Without Lattice Bias. *J. Phys. Condens. Matter* **2009**, *21*, 084204.
250. Sanville, E.; Kenny, S. D.; Smith, R.; Henkelman, G. An Improved Grid-Based Algorithm for Bader Charge Allocation. *J. Comput. Chem.* **2007**, *28*, 899–908.
251. Henkelman, G.; Arnaldsson, A.; Jónsson, H. A Fast and Robust Algorithm for Bader Decomposition of Charge Density. *Comput. Mater. Sci.* **2006**, *36*, 354–360.
252. Yu, M.; Trinkle, D. R. Accurate and Efficient Algorithm for Bader Charge Integration. *J. Chem. Phys.* **2011**, *134*, 064111.
253. Stevens, D. A.; Dahn, J. R. An In Situ Small-Angle X-Ray Scattering Study of Sodium Insertion into a Nanoporous Carbon Anode Material within an Operating Electrochemical Cell. *J. Electrochem. Soc.* **2000**, *147* (12), 4428–4431.
254. Stevens, D. A.; Dahn, J. R. High Capacity Anode Materials for Rechargeable Sodium-Ion Batteries. *J. Electrochem. Soc.* **2000**, *147* (4), 1271–1273.
255. Letellier, M.; Chevallier, F.; Cléard, C.; Frackowiak, E.; Rouzaud, J.-N.; Béguin, F.; Morcrette, M.; Tarascon, J.-M. The First In Situ ^{7}Li Nuclear Magnetic Resonance Study of Lithium Insertion in Hard-Carbon Anode Materials for Li-ion Batteries. *J. Chem. Phys.* **2003**, *118* (13), 6038–6045.
256. Stratford, J. M.; Allan, P. K.; Pecher, O.; Chater, P. A.; Grey, C. P. Mechanistic Insights Into Sodium Storage in Hard Carbon Anodes Using Local Structure Probes. *Chem. Commun.* **2016**, *52* (84), 12430–12433.
257. Rao, F.; Wang, Z.; Xu, B.; Chen, L.; Ouyang, C. First-Principles Study of Lithium and Sodium Atoms Intercalation in Fluorinated Graphite. *Engineering* **2015**, *1* (2), 243–246.
258. Toberer, E. S.; May, A. F.; Snyder, G. J. Zintl Chemistry for Designing High Efficiency Thermoelectric Materials. *Chem. Mater.* **2010**, *22*, 624–634.
259. Sootsman, J. R.; Chung, D. Y.; Kanatzidis, M. G. New and Old Concepts in Thermoelectric Materials. *Angew. Chem. Int. Ed.* **2009**, *48*, 8616–8639.
260. Snyder, G. J.; Toberer, E. S. Complex Thermoelectric Materials. *Nat. Mater.* **2008**, *7*, 105–114.
261. Kauzlarich, S. M.; Brown, S. R.; Snyder, G. J. Zintl Phases for Thermoelectric Devices. *Dalton Trans.* **2007**, 2099–2107.
262. Zintl, E. Intermetallics Verbindungen. *Angew. Chem.* **1939**, *52*, 1–6.
263. Schäfer, H.; Eisenmann, B.; Müller, W. Zintl Phases: Transitions Between Metallic and Ionic Bonding. *Angew. Chem. Int. Ed. Engl.* **1973**, *12*, 694–712.
264. Miller, G. J.; Schmidt, M. W.; Wang, F.; You, T.-S. Quantitative Advances in the Zintl-Klemm Formalism. *Struct. Bond.* **2011**, *139*, 1–55.
265. Göbgen, K. C.; Gladisch, F. C.; Steinberg, S. The Mineral Stützite: A Zintl-Phase or Polar Intermetallic? A Case Study Using Experimental and Quantum-Chemical Techniques. *Inorg. Chem.* **2018**, *57*, 412–421.
266. Kälin, W.; Günter, J. R. Preparation of $\text{Ag}_{5-x}\text{Te}_3$ Thin Films and Confirmation of Their Crystal Structure by High Resolution Electron Microscopy. *J. Solid State Chem.* **1996**, *123*, 391–397.
267. Peters, J.; Conrad, O.; Bremer, B.; Krebs, B. Die Kristallstruktur des synthetischen Stützits, $\text{Ag}_{5-x}\text{Te}_3$. *Z. Anorg. Allg. Chem.* **1996**, *622*, 1823–1832.
268. Imamov, R. M.; Pinsker, Z. G. Determination of the Crystal Structure of the Hexagonal Phase in the Silver-Tellurium System. *Kristallografiya* **1966**, *11*, 182–190.
269. Pearson, R. G. Absolute Electronegativity and Hardness: Application to Inorganic Chemistry. *Inorg. Chem.* **1988**, *27*, 734–740.
270. Allen, L. C.; Capitani, J. F.; Kolks, G. A.; Sproul, G. D. Van Arkel—Ketelaar Triangles. *J. Mol. Struct.* **1993**, *300*, 647–655.
271. Woodward, R. B.; Hoffmann, R. Stereochemistry of Electrocyclic Reactions. *J. Am. Chem. Soc.* **1965**, *87* (2), 395–397.
272. Esser, M.; Deringer, V. L.; Wuttig, M.; Dronskowski, R. Orbital Mixing in Solids as a Descriptor for Materials Mapping. *Solid State Commun.* **2015**, *203*, 31–34.
273. Anderson, W. P.; Burdett, J. K.; Czech, P. T. What Is the Metallic Bond? *J. Am. Chem. Soc.* **1994**, *116* (19), 8808–8809.
274. Allen, L. C.; Burdett, J. K. The Metallic Bond—Dead or Alive? A Comment and a Reply. *Angew. Chem. Int. Ed.* **1995**, *34* (18), 2003.
275. Wuttig, M.; Raoux, S. The Science and Technology of Phase Change Materials. *Z. Anorg. Allg. Chem.* **2012**, *638* (15), 2455–2465.
276. Zhu, M.; Cojocaru-Mirédin, O.; Mio, A. M.; Keutgen, J.; Küpers, M.; Yu, Y.; Cho, J.-Y.; Dronskowski, R.; Wuttig, M. Unique Bond Breaking in Crystalline Phase Change Materials and the Quest for Metavalent Bonding. *Adv. Mater.* **2018**, *30* (18), 1706735.
277. Pries, J.; Cojocaru-Mirédin, O.; Wuttig, M. Phase-Change Materials: Empowered by an Unconventional Bonding Mechanism. *MRS Bull.* **2019**, *44* (9), 699–704.
278. J. Hempelmann, P. C. Müller, C. Ertural, R. Dronskowski The Orbital Origins of Chemical Bonding in Ge–Sb–Te Phase-Change Materials, *Angew. Chem. Int. Ed.*, **2022**, *61*, e202115778
279. Nonaka, T.; Ohbayashi, G.; Toriumi, Y.; Mori, Y.; Hashimoto, H. Crystal Structure of GeTe and $\text{Ge}_2\text{Sb}_2\text{Te}_5$ Meta-Stable Phase. *Thin Solid Films* **2000**, *370* (1), 258–261.
280. Waghamore, U. V.; Spaldin, N. A.; Kandpal, H. C.; Seshadri, R. First-Principles Indicators of Metallicity and Cation Off-Centricity in the IV-VI Rocksalt Chalcogenides of Divalent Ge, Sn, and Pb. *Phys. Rev. B* **2003**, *67* (12), 125111.
281. Konze, P. M. *On Chemical Bonding in Layered Chalcogenides*. Dissertation, RWTH Aachen, 2019.
282. Shannon, R. D. Revised Effective Ionic Radii and Systematic Studies of Interatomic Distances in Halides and Chalcogenides. *Acta Cryst. A* **1976**, *32* (5), 751–767.
283. Adenis, C.; Langer, V.; Lindqvist, O. Reinvestigation of the Structure of Tellurium. *Acta Cryst. C* **1989**, *45* (6), 941–942.
284. Carpenter, G. B. The Use of n-Center Bonds. *J. Chem. Educ.* **1963**, *40* (7), 385–387.
285. Schmidt, M. W.; Baldridge, K. K.; Boatz, J. A.; Elbert, S. T.; Gordon, M. S.; Jensen, J. H.; Koseki, S.; Matsunaga, N.; Nguyen, K. A.; Su, S. General Atomic and Molecular Electronic Structure System. *J. Comput. Chem.* **1993**, *14* (11), 1347–1363.
286. Landrum, G.; Glassey, W. *YAEHMOP, version 3.0*. Cornell University: Ithaca, NY, 1995.
287. Deringer, V. L.; Dronskowski, R. Computational Methods for Solids. In *Comprehensive Inorganic Chemistry II: From Elements to Applications*; Reedijk, J., Poeppelmeier, K., Eds.; vol. 9; Elsevier: Amsterdam, 2013; pp 59–87.
288. Esser, M. *Materialkarten ab initio: Quantenchemische Wegweiser zur Entdeckung und Charakterisierung neuer Funktionsmaterialien*. Dissertation, RWTH Aachen, 2017.